Chapter 8

Metal Oxide Nanomaterials, Conducting Polymers and Their Nanocomposites for Solar Energy

Sadia Ameen, M. Shaheer Akhtar, Minwu Song and Hyung Shik Shin

Additional information is available at the end of the chapter

http://dx.doi.org/10.5772/51432

1. Introduction

The increasing concern on energy and the global warming due to the depletion of fossil fuel demands to search the alternative renewable energy resources for covering the energy crisis in the coming decade. A very popular renewable source called photovoltaic device is anticipated to solve energy problem, which converts directly the solar energy from sun to the electricity energy. Recently, dye sensitized solar cells (DSSCs) are widely used as promising photovoltaic device owing to its important properties like high solar to electricity energy conversion efficiency, low production cost, ease of fabrication and vast varieties of various semiconducting materials. DSSC is composed of few micrometer-thick nanocrystalline semiconducting oxides thin film combined with monolayer of charge-transfer dye as a photoanode, a redox electrolyte and a platinum metal electrode as counter electrode. In principle, upon illumination, the electron injection to conduction band of semiconductor takes place by the absorption of photons from dye molecules and the redox electrolyte regenerates the oxidized dye by the transportation of charges or ions. These days, the photovoltaic devices are facing inherent drawbacks such as leakage and evaporation problem that limits its practical application. In this regards, efforts are being done to overcome the leakage and evaporation of liquid electrolyte with solid or gel electrolytes such as room temperature molten salts (RTMSs), p-type semiconductor, conducting organic polymers and polymer gel electrolytes. Furthermore, the choice of catalytic in counter component of DSSCs is crucial to improve the reduction rate of I_3^- to I^- in the redox electrolyte. In general, the conducting glass electrode without any catalytic materials such as metals, conducting polymers etc shows very low electrocatalytic activity towards the iodide couple electrolyte due to overvoltage and high energy loss. It has been realized that the low resistance and high electrocatalytic materials

might deliver the better catalyst to avoid the overvoltage and energy loss for the high reduction of I_3^- in redox electrolyte.

The semiconducting nanomaterials based thin film electrodes with high surface area are of great significance for acquiring the high amount dye adsorption which leads to the higher light harvesting efficiency and photocurrent density. Various metal oxides semiconductors such as TiO_2, ZnO and SnO_2 have shown good optical and electronic properties and are accepted as the effective photoanode materials for DSSCs. Additionally, the morphology and sizes of metal oxides semiconducting materials, particularly one dimensional (1D) nanostructures like nanorods (NRs), nanowires (NWs) and nanotubes (NTs) based electrodes have shown increased electron transfer during the operation of DSSCs owing to their high surface to volume ratio and arrangements. Until now, the photoanodes with TiO_2, SnO_2/ZnO, Nb_2O_5 and ZnO nanomaterials have presented the maximum solar to electricity energy conversion efficiencies of ~11.2%, ~8%, ~2% and ~5% respectively.

On the other hand, the conducting polymers are regarded as promising semiconducting materials due to distinguishable electrical properties, mechanical flexibility, and the relative ease of processing. The conductive polymers such as polypyrrole, poly (3, 4-ethylenedioxy-thiophene) and polyaniline (PANI) are frequently used in DSSC as hole transport materials, electron acceptor and electrocatalytic materials for tri-iodide reduction in redox electrolyte. Among them, PANI is an excellent host for the trapping of semiconducting nanomaterials and conducts the electric charges through the polymeric chain due to extended π-electron conjugation. The conducting polymers and dye sensitized metal oxides are good electron donors upon the photo-excitation during the operation of DSSCs.

In this chapter, we have briefly discussed the different conducting polymers, metal oxides and their application for the performance of DSSCs. The chapter includes the brief literature surveys, properties and photovoltaic properties of various metal oxides nanomaterials, nanofillers in polymer electrolytes and the conducting polymers. Additionally, the latest research advancements are surveyed for the development of efficient conducting polymers as p-type semiconducting nanomaterials for counter electrode materials and efficient nanofillers in the solid polymers of DSSCs. Moreover, the doping and the utilization of TiO_2 and ZnO nanomaterials for the performance of DSSCs have been discussed in details. It has been seen that the preparation methods, doping, morphologies, and the sizes of conducting polymers and metal oxides have shown the considerable impact on the electrical properties of the nanomaterials and performances of DSSCs. The study also demonstrates the enhanced properties of inorganic metal oxides like ZnO and TiO_2 with different sizes and morphologies for achieving the efficient photovoltaic properties of DSSCs such as J_{SC}, V_{OC}, FF and conversion efficiency.

2. Types of conducting polymers

The conducting polymers are composed of π-conjugated polymeric chain and are known as "synthetic metals" [1-2]. These extended π-conjugated systems of conducting polymers have

http://dx.doi.org/10.5772/51432

alternating single and double bonds along the polymeric chain [3]. The conducting polymers display the overlapping of molecular orbital to allow the formation of delocalized molecular wave functions and secondly these molecular orbital must be partially filled so that there is a free movement of electrons in the polymeric structure. The presence of unusual electronic properties such as electrical conductivity, low ionization potential and high electron affinity are associated with the π-electron backbone of the conjugated polymers. These are promising candidates for electronics applications, and offer possible replacements of the conventional metals and inorganic semiconductors [4-5]. The electrical conductivity of the conducting polymers could be altered upon partial oxidation or reduction by a commonly referred process called 'doping'. The electrical conductivity of these polymers could be changed from insulating to metallic by chemical or electrochemical doping and they could be used to produce electronic devices. These polymers have the electrical properties like that of metals, and have attractive characteristics of organic polymers such as light weight, resistance to corrosion, flexibility and lower cost. Additionally, these polymers could be tailor-made to the requirements of the application through modifications in the polymer structure by varying the functional groups in the organic moiety. The commercial applications of conducting polymers are in thin film transistor, batteries, antistatic coatings, electromagnetic shielding, artificial muscles, light-emitting diodes, gas and bio-sensors [6], fuel and solar cells, fillers [7] and corrosion protective coatings [8]. The conducting polymers are easy to synthesize through chemical or electrochemical processes, and their molecular chain structure could be modified conveniently by the copolymerization or structural derivations. Typically, the conducting polymers are of several types as listed below:

2.1. Polypyrrole (PPy)

Polypyrrole (PPy) is a versatile polymer of significant properties like redox activity [9] ion-exchange, ion discrimination capacities [10], electrochromic effects, charge/discharge processes [11] and exhibits strong absorptive properties towards gases [12], catalytic activity [13] and corrosion protection properties [14]. It is one of the important conducting polymers due to its good electrochemical reversibility between its conducting and insulating states and the ease of preparation through chemical or electrochemical routes [15].

2.2. Poly phenylenes) (PP)

Poly phenylene (PP) is one of the most unusual electro conducting polymers due to the extended planar conjugated π-system, along with high strength and high heat resistance [16]. The most widely used method of PP production is benzene oxidation with a Friedel-Crafts catalyst (the Kovacic method) [17], which yield a polycrystalline powder. Besides, electrochemical polymerization is also a method for PP synthesis, but the molecular weight of the polymer is limited due to its insolubility and chemical defect [18].

2.3. Polyacetylene (PA)

Polyacetylene (PA) is the polymer of highest conductivity as compared to those of conventional metals. PA has the simplest structure of the linear chains of C-H units with alternating single

and double bonds [19]. Moreover, the existence of the two hydrogen atoms in its repeat unit offers ample opportunity to decorate the backbone with pendants which perturbs the electronic conjugation and influences the molecular alignment of the polymeric chain. Significantly, the proper structural design might tune the backbone-pendant interplay into harmony and synergy, generating new substituted PAs with novel functionalities [20].

2.4. Polyazule (PAz)

The electron-donor and electron-acceptor character of polyazulene (PAz) has been explained by the electron-donor effect of the seven-membered ring toward the five-membered ring. The five-membered ring carries a partial negative charge and the seven-membered ring of azulene carries a partial positive charge. The polymers and its derivatives show high electrical conductivity almost similar as polythiophene, polypyrrole and polyaniline [21].

2.5. Polyindole (PIN)

Polyindol (PIN) is an electroactive polymer which could be obtained by the anodic oxidation of indole in various electrolytes. It is reported that the conductivity of PIN is lower than that of PPy and PANI but its thermal stability is better with respect to PANI and PPy. PIN, a macromolecular compound, is a good candidate for applications in various areas, such as electronics, electrocatalysis, and active materials for anodes of batteries, anticorrosion coatings and pharmacology.

2.6. Polycarbazole (PCz)

Polycarbazole (PCz) among conducting polymers, is attributed with good electroactivity, and useful thermal, electrical and photophysical properties [22]. However, π-π electron system along its backbone imparts rigidity to the polymer and therefore, makes it infusible and poorly processable. The increasing interest in PCz is towards its role as a hole-transport material and an efficient photoluminescence unit [23]. Derivatives of carbazole are easily prepared by the substitution at -N atom and thus, the solubility and functionality of the resulting polymers could be improved. More importantly, the substituted groups might influence the effective conjugation length which is promising materials in making the emitting light in devices.

2.7. Polyaniline (PANI)

Polyaniline (PANI) exhibits the high stability, conductivity and low cost [24-25]. PANI basically undergoes oxidative polymerization in the presence of a protonic acid. Protonation induces an insulator-to-conductor transition, while the number of π-electrons in the chain remains constant. The oxidation and reduction takes place on this –NH– group, and various forms are obtained due to the number of imine and amine segments on the PANI chain. Other substituted aniline like *N*-benzenesulfaniline [26], o-, p- and m-toluidine, o-chloroaniline [27], o-, m- and p-halogenated anilines [28] and 1-Napthylamine are also the subject of current studies and could be used for the semiconducting polymers based electronic applications.

http://dx.doi.org/10.5772/51432

Out of several conducting polymers, the interest of researchers in PANI could possibly be linked to the numerous applications that exist for the electronic conducting polymers and also aniline is cheap product and also a very stable material. On the other hand, the nanocomposites of conducting polymers with inorganic semiconducting nanomaterials show the improved mechanical, electrical and thermal properties due to the combined effects of both the semiconducting nanomaterials and conducting polymers. In particular, PANI nanocomposites display applications on a large scale for various electrochemical, electrorheological and in the electronic fields such as batteries, sensors, controlling systems and organic displays [29]. The nanocomposites of PANI with cadmium sulphide has been discussed in the next section of the chapter

3. Nanocomposites of conducting polymers

3.1. Nanocomposites of PANI and cadmium sulphide

Cadmium Sulphide (CdS) is a semiconductor with a direct band gap of ~2.42 eV which displays superior optical, photophysical and photochemical properties [30]. The nanocomposites of CdS and PANI have presented the effective electrode materials for many electrochemical, photoelectrochemical, sensing and electrochromic devices [31]. The nanocomposites are anticipated as effective and promising electrode materials in many electrochemical devices. Xi et al studied the influence of optical and absorption properties of CdS by the incorporation of CdS into PANI matrix [32]. R. Seoudi et al studied the dependence of structural, vibrational spectroscopy and optical properties on the particle sizes of PANI/CdS nanocomposites [33]. B.T. Raut et al reported the novel method of fabrication of PANI/CdS nanocomposites and studied the structural, morphological and optoelectronic properties [34]. In this regards, Ameen et al has reported a simple solution method to synthesize the CdS decorated PANI nanorods (NRs) and studied the electrochemical impedance properties of the nanocomposites [35].

The synthesized PANI NRs exhibit the entangled network with diameter of ~40-50 nm and length of several hundred nanometers, as shown in Fig. 1 (a). The uniform decoration and the thicknesses of CdS-PANI NRs increase gradually with the increase of $CdCl_2$ concentration. After sensitization with the highest concentration of $CdCl_2$ (0.1 M), the surface of PANI NRs (Fig. 1(b)) is completely decorated by CdS nanoparticles which results in the enhanced diameter of ~60-70 nm. The TEM characterization (Fig. 1 (c and d)) clearly justifies the decoration of CdS nanomaterials on the surface of PANI NRs and shows the increased thickness of PANI NRs with the average diameter of ~60-70 nm due to the decoration of CdS nanoparticles with highest concentration of $CdCl_2$ (0.1 M). From the EDS studies, the overall CdS contents have been estimated as 0.34, 0.53 and 1.08 wt% in the synthesized CdS-PANI NRs with $CdCl_2$ concentrations of 0.01 M, 0.05 M and 0.1 M respectively.

The Raman bands at ~1175 cm^{-1}, ~1507 cm^{-1}, ~1595 cm^{-1} are observed in all the samples of CdS-PANI NRs (Fig. 2), corresponding to the C-H bending vibration of the semi quinonoid rings (cation-radical segments), N-H deformation vibration associated with the semiquinonoid structures and C=C stretching vibration in the quinonoid ring respectively [36]. PANI NRs show a relatively high band at ~1368 cm^{-1} in the spectrum which provides the information of

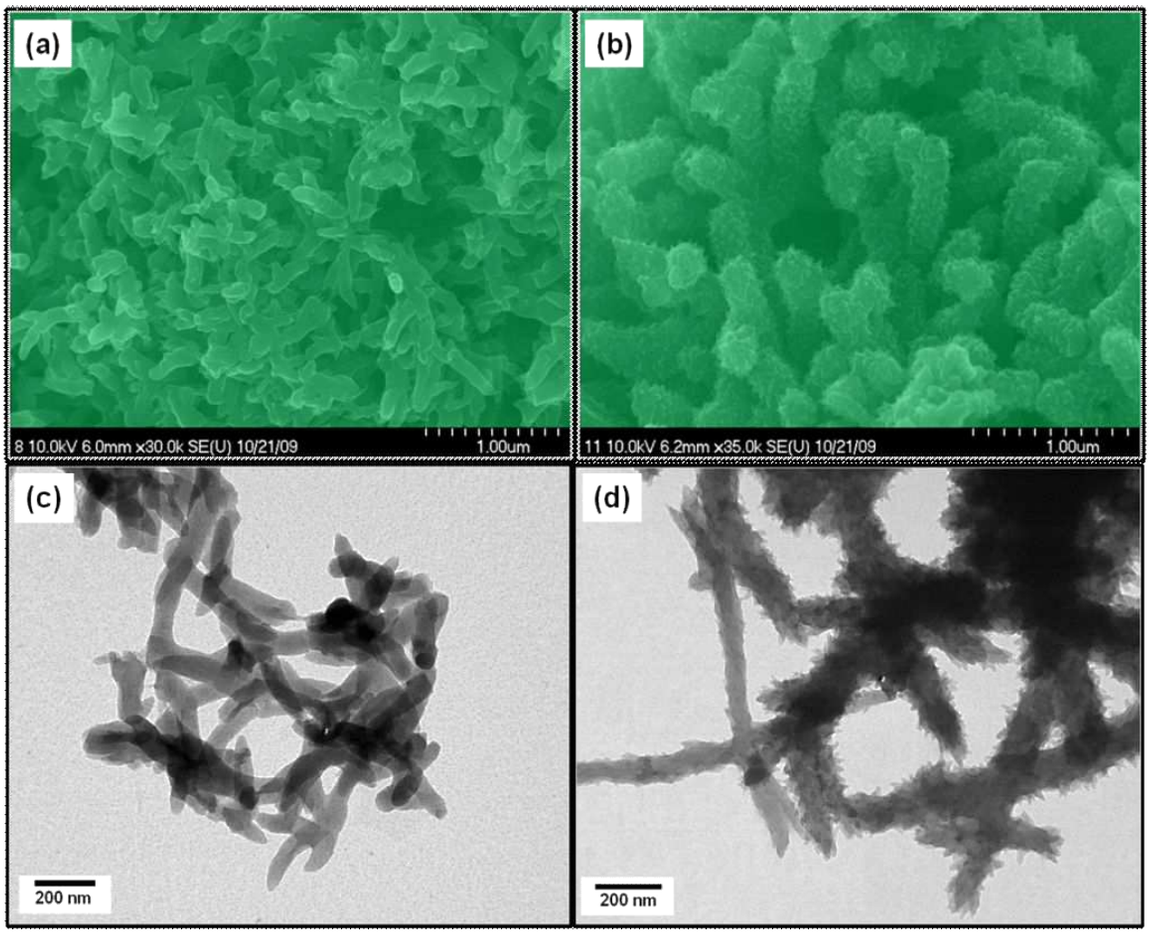

Figure 1. FESEM (a, b) and TEM (c, d) images of synthesized PANI NRs and CdS-PANI NRs. Reprinted with permission from [Ameen S., 2012], Chem. Eng. J. 181 (2012) 806 ©2012, Elsevier Ltd.

the C-$N^{+\bullet}$ vibration of delocalized polaronic structures [37]. The absence of this band in CdS-PANI NRs might due to the efficient interaction of imine (-NH) group of PANI with CdS nanomaterials.

The UV-Vis absorption spectra of the PANI NRs and CdS-PANI NRs are depicted in Fig. 3(a). In PANI NRs, the broad absorption bands at ~617 nm is related to n-π* transition, and the absorption peak at ~268 nm and ~327 nm arises due to π-π* transition within the benzenoid segment which is associated to the extent of conjugation between adjacent phenyl rings in the PANI [38]. On comparison to PANI NRs, the red shifting are seen and absorption bands move to higher wavelength of ~279 nm, ~338 nm and ~630 nm respectively in CdS-PANI NRs due to the sensitization of CdS nanomaterials with PANI NRs. The red shift of absorption bands with high intensities reveals that PANI NRs might form a partial bond with CdS nanoparticles. The room temperature photoluminescence (PL) spectra (Fig. 3(b)) of PANI NRs and CdS-PANI NRs exhibit a single large amplitude band in the blue green region which originated due to the π–π* transition of the benzenoid unit of PANI [39]. The sensitization of PANI NRs with the highest concentration of $CdCl_2$ (0.1 M) causes a significant red shift from ~421 nm to ~438 nm as compared to the PANI NRs which might occur by the chemical interaction between -

http://dx.doi.org/10.5772/51432

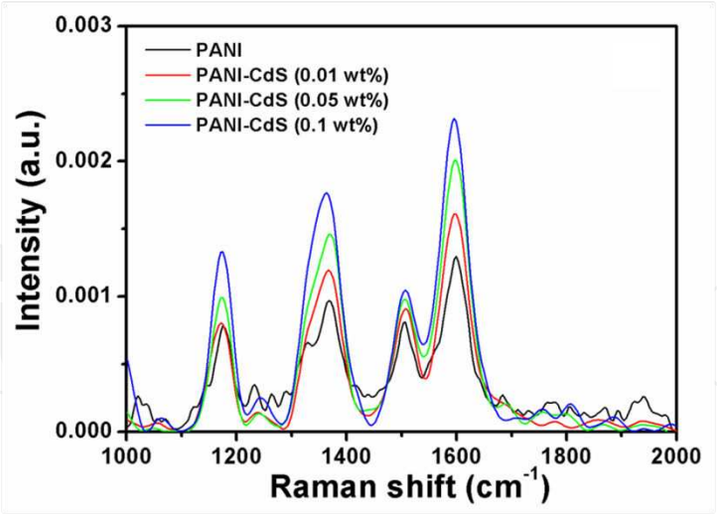

Figure 2. Raman Spectra of PANI NRs and CdS-PANI NRs. Reprinted with permission from [Ameen S., 2012], Chem. Eng. J.181 (2012) 806 ©2012, Elsevier Ltd.

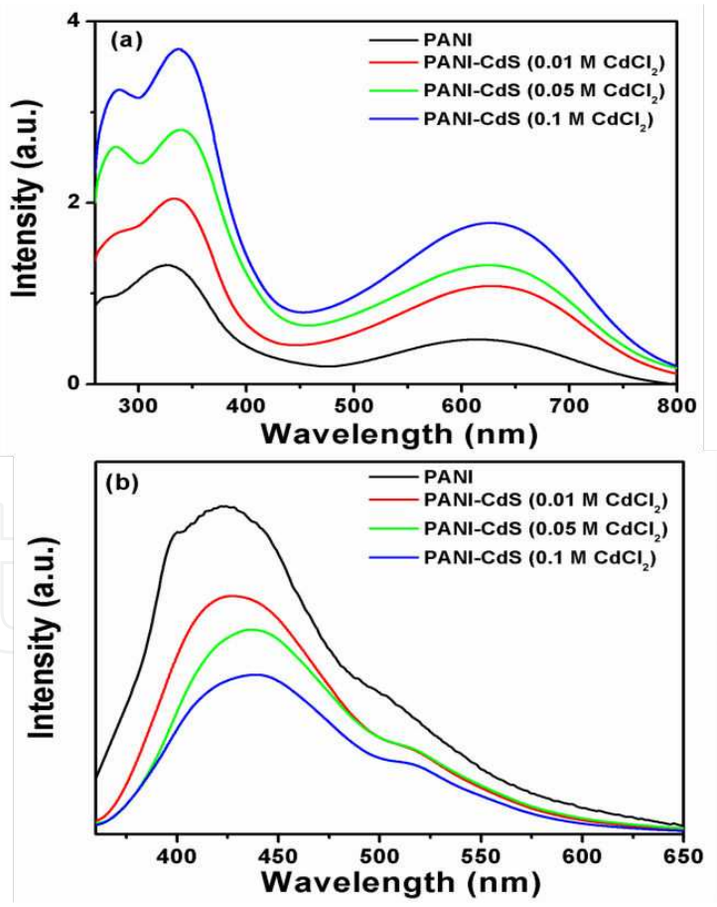

Figure 3. UV-vis absorption spectra (a) and photoluminescence spectra (b) of PANI NRs and CdS-PANI NRs. Reprinted with permission from [Ameen S., 2012], Chem. Eng. J.181 (2012) 806 ©2012, Elsevier Ltd.

NH groups of the PANI chains and surface of CdS. The CdS-PANI NRs sensitized with 0.1 M $CdCl_2$, shows the lowest PL intensity and the highest peak shift, suggesting the large π–π^* transition of the benzenoid unit and the strong chemical interaction between -NH groups of the PANI chains and surface of CdS.

The X-rays Photoelectron Spectroscopy (XPS) has studied to examine the interaction between CdS nanoparticles and the PANI NRs, as shown in Fig. 4. The C 1s XPS spectrum (Fig. 4 (a)) of CdS-PANI NRs shows the center peak at ~284.0 eV with five resolved peaks at the binding energies spanning the range from ~288 to ~283 eV. The strong peak at ~ 283.4 eV represents the carbon (C) of benzonoid ring in which a combination of protonation of imine and amine sites are formed via shake-up processes [40]. The next three resolved peaks at ~284.8 eV, ~285.7 eV and ~286.8 eV confirm the origin of the neutral C-C/C-H bond-PANI backbone, $C\text{-}N^+/C{=}N^+$ bond and C=O/C-O bond (might occur due to the absorption of moisture on the CdS-PANI), respectively [41]. The resolved peaks at ~287.8 eV assigns to the π-π^* bonding in a long-range order with a polymer chain shake-up satellite structure and coincides with the doped states. On comparison with typical PANI peak [42], C 1s peak has shifted backwardly, suggesting that C toms of PANI is interacted with other materials (CdS, TiO_2 etc.) or impurities [43]. The O 1s XPS spectrum (Fig. 4(c)) exhibits the center peak at ~530.1 eV with three resolved peaks

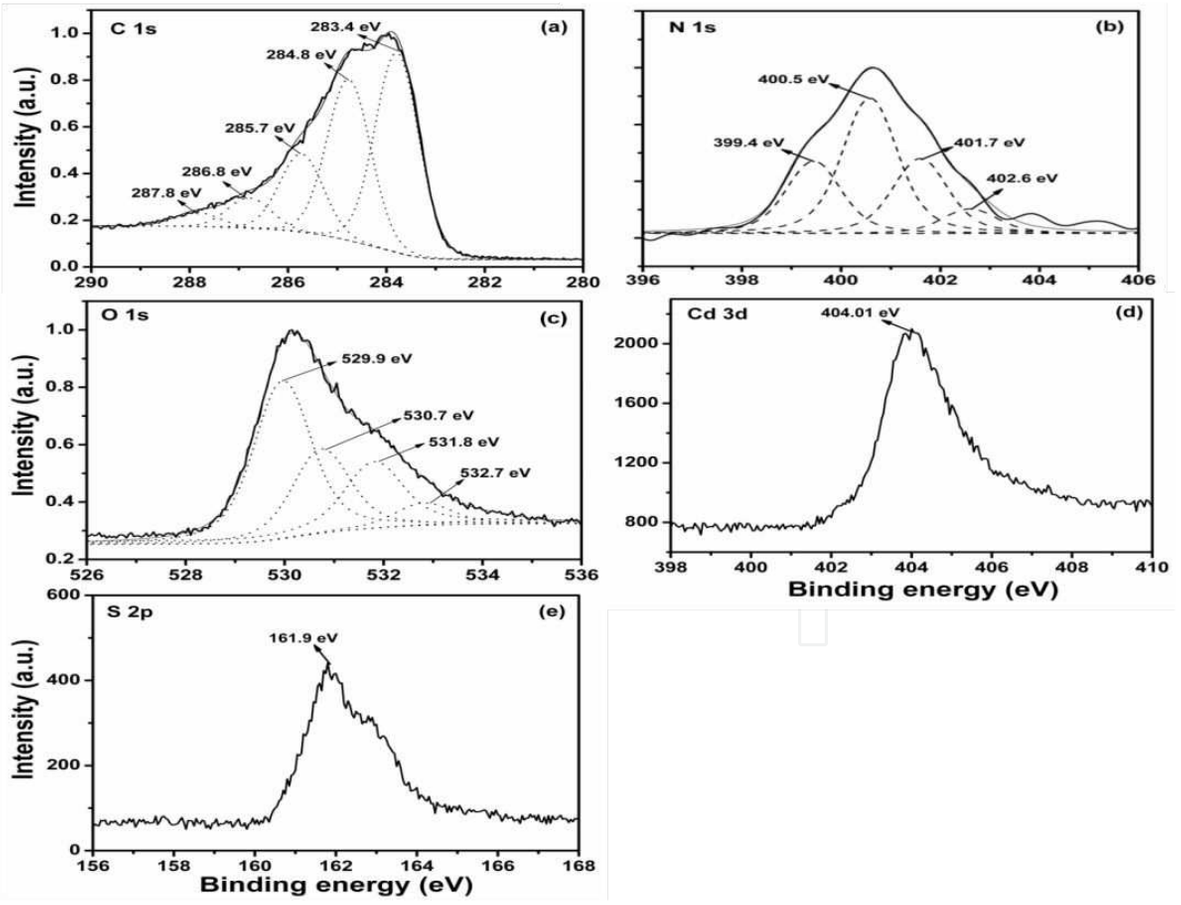

Figure 4. (a) C 1s, (b) N 1s, (c) O 1s, (d) Cd 3d and (e) S 2p XPS spectra of CdS-PANI NRs. Reprinted with permission from [Ameen S., 2012], Chem. Eng. J.181 (2012) 806© 2012, Elsevier Ltd.

at ~530.7, ~531.8 and ~532.7 eV, suggesting the absorption of moisture and some oxygen impurities on the surface of CdS-PANI NRs during the synthesis. In N 1s XPS spectra (Fig. 4(b)), the main center peak with binding energy at ~400.5 eV and a resolved peak with lower binding energy at ~399.4 eV attribute to nitrogen atom originated from benzenoid diamine and quinoid di-imine nitrogen of PANI respectively. The other binding energies of ~401.7 and ~402.6 eV are ascribed to the positively charged nitrogens i.e. oxidized amine (N^+) and protonated imine (N^+) respectively [44]. The positive shifting is seen in the binding energies at ~401.7 eV and ~402.6 eV as compared with N 1s spectrum of pristine PANI indicating the involvement of positively charged nitrogen or protonated nitrogen for the partial bonding between PANI and CdS. Furthermore, the singlet peak at ~404.01 eV observes in Cd 3d XPS (Fig. 4(d)) spectrum, corresponding to Cd $3d_{5/2}$ and the typical peak of Cd^{+2} atoms in CdS [45]. Fig. 4(e) presents the S 2p XPS spectrum of CdS-PANI NRs and observed one distinct peak of $S2p_{3/2}$ at ~161.9 eV, corresponds to S^{-2} of CdS nanoparticles. This suggests the interaction and bonding between CdS nanomaterials and PANI molecules. Thus, it is concluded that the PANI and CdS nanomaterials are partially interacted and bonded by two charged nitrogen species (N^+ and N^+) of PANI with CdS nanomaterials.

Fig. 5 shows the Nyquist plot of EIS measurement for PANI NRs and CdS-PANI NRs electrodes in the electrolyte (LiI, I_2 and $LiClO_4$ in ethanol) at a frequency range from 100 kHz to 1 Hz. The almost same R_S (electrolyte resistance) with a depressed semi circle in the high frequency region is observed for the all the samples. The presence of depressed semi circle plot is ascribed to the parallel combination of the charge transfer resistance (R_{CT}) of the electrochemical reaction and the double layer capacitance (C_{dl}) of the PANI film/electrolyte interface [46] has been removed. As shown in Fig. 5, the PANI NRs electrode displays large R_{CT} value of ~17 kΩ. The R_{CT} values drastically decreases by the incremental addition of $CdCl_2$ in PANI NRs, and the order of R_{CT} values are measured as 8.4 kΩ ($CdCl_2$ (0.01 M)-PANI NRs) < 5.7 kΩ ($CdCl_2$ (0.05 M)-PANI NRs) < 4.08 kΩ ($CdCl_2$ (0.10 M)-PANI NRs). Usually, the electrode with large R_{CT} leads the slow charge transfer rate of the electrochemical system [46]. It could be seen that the highest R_{CT} value of PANI NRs electrode might result the low charge transfer rate to the electrochemical system. Moreover, the CdS decorated PANI NRs electrode with 0.01 M $CdCl_2$ presents lowest R_{CT} value which delivers the higher charge transfer rate. The variation in charge transfer resistance (R_{CT}) after the CdS sensitization by different concentrations of $CdCl_2$ might attribute to the changes in the NRs structure. Considerably, the direct band gap of CdS nanoparticles might also affect which improve the electronic state like polarons and bipolarons of PANI for the high charge carriers and enhance the charge transfer. Therefore, the CdS-PANI NRs is potential and cost effective electrode materials for the fabrication of efficient electrochemical (sensor, field emission transistor), photoelectrochemical and photovoltaic devices.

4. Basic structure and kinetics of DSSCs

Last few decades, considerable researches on DSSCs have extensively explored in terms of both fundamental and applied viewpoints. The basic components of DSSCs involves the

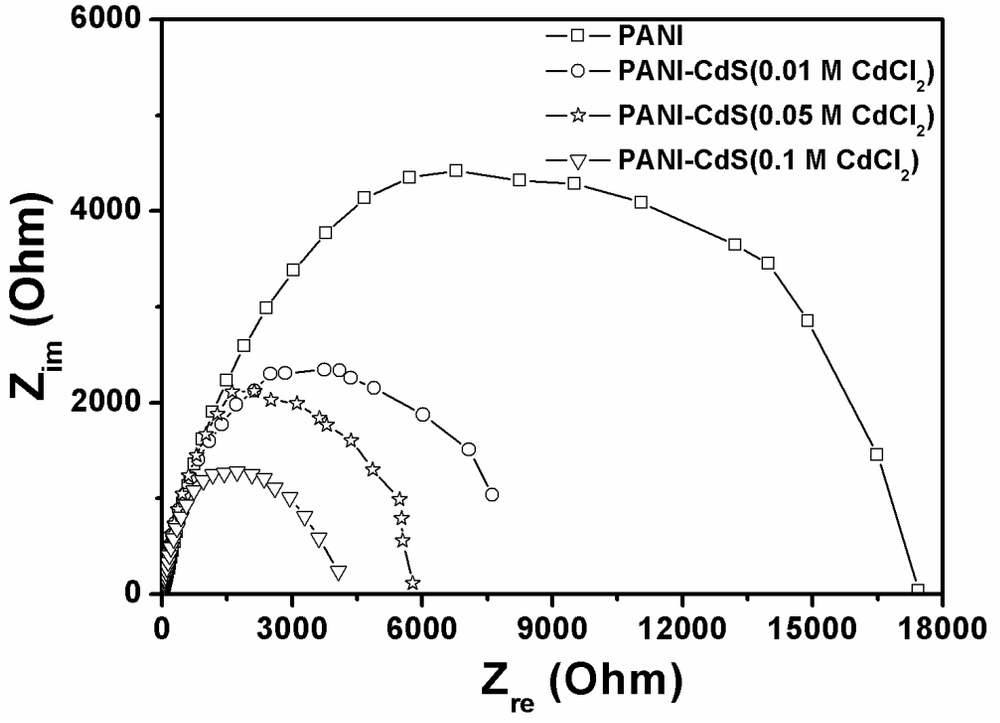

Figure 5. Nyquist plots of PANI NRs and CdS–PANI NRs at a frequency range from 100 kHz to 1 Hz. Reprinted with permission from [Ameen S., 2012], Chem. Eng. J.181 (2012) 806 ©2012, Elsevier Ltd.

conducting fluorine doped tin oxide (FTO) glass, sensitized dye, titania nanoparticles, electrolyte and Pt deposited FTO glass. The working principle of DSSC, involves the adsorption of photons by dye molecules upon light illumination and the injection of electrons from their excited states into the conduction band of the TiO_2 nanoparticles. During the entire process, the oxidized dye molecules are recharged by a redox electrolyte, which transports the positive charges by diffusion to a Pt counter electrode. The low absorption coefficient of a dye monolayer is compensated by the mesoporous structure of the TiO_2 film, which leads to a strong increase in the number of TiO_2/dye/electrolyte interfaces through which photons pass, thus increases the absorption probability. The following steps are in photoelectric chemical mechanism process of DSSC:

i. $TiO_2|D + h\nu \rightarrow TiO_2|D^*$ Excitation

ii. $TiO_2|D^* \rightarrow TiO_2|D^+ + \bar{e}$ (cb) Injection

iii. $TiO_2|2D^+ + 3I^- \rightarrow TiO_2|2S + I_3^-$ Regeneration

iv. $I_3^- + 2\ \bar{e}$ (Pt) $\rightarrow 3I^-$ Reduction

v. $I_3^- + 2\ \bar{e}$ (cb) $\rightarrow 3I^-$ Recaption (dark reaction)

vi. $TiO_2|S^+ + \bar{e}$ (cb) $\rightarrow TiO_2|S$ Recombination (dark reaction)

For the efficient working of DSSCs, the rate of re-reduction of the oxidized dye must be higher than the rate of back reaction of the injected electrons with the dye as well as the rate of reaction of injected electrons with the electron acceptor in the electrolyte. The kinetics of the reaction

http://dx.doi.org/10.5772/51432

at the counter electrode and mesoscopic semiconductor materials with an enormous internal surface area to absorb more incident light via dye as sensitizers determines the fast regeneration of charge mediator performance [47]. Apart from this, the other significant parameters which influence the performance of DSSCs are the mesoporous morphology with high surface area of semiconducting electrode to allow absorption of a larger amount of dye and the efficient charge carriers transport at the interface of photoanode and counter electrode by the semiconducting electrode. Moreover, the oxidized dye should be reduced to its ground state rapidly, after the injection of photoexcited electron from dye into the conduction band of semiconducting electrode. Furthermore, the semiconducting electrode must be able to permit the fast diffusion of charge carriers (higher conductivity) and produces good interfacial contact with the porous nanocrystalline layer and the counter electrode, the long-term stability, including chemical, thermal, optical, electrochemical, and interfacial stability of the electrolyte, which does not cause the desorption and degradation of the dye from the oxide surface and lastly, the optimized concentration of I^-/I_3^- which could reduce the visible light absorption by the dye, and the efficient reaction of I_3^- ions with the injected electrons to increase the dark current.

5. DSSCs based on conducting polymers

5.1. PANI as hole transport materials for DSSCs

The DSSCs and polymer solar cell have been exploring the new approaches in the design of both active materials and device architectures [48]. J. Wagner et al reported the new carbazole-based polymers for DSSCs with hole-conducting polymer [49]. N. Kudo et al fabricated the organic-inorganic hybrid solar cells based on conducting polymer and SnO_2 nanoparticles which were chemically modified with a fullerene derivative [50]. S. Woo et al reported the hybrid solar cells with conducting polymers and vertically aligned silicon nanowire arrays and studied the effects of silicon conductivity [51]. F. Tan et al synthesized PANI films by electrodepostied methods and applied as anode buffer layers in solar cells [52]. M. Y. Chang et al fabricated the polymer solar cells by incorporating one-dimensional polyaniline nanotubes [53]. T. H. Lim et al utilized PANI for a flexible organic solar cells anode [54]. H. Bejbouji et al reported PANI as a hole injection layer on organic photovoltaic cells [55]. S. Zhu et al synthesized the hybrid structure of PANI/ZnO nanograss for the application in dye-sensitized solar cell1 [56]. PANI is also known as large band gap hole transporting material (HMTs) which could easily deposit as thin film on several substrates. In this regards, Ameen et al has reported the application of PANI as photoelectrode using N710 and Z907 as sensitizers for the performance of DSSCs [57].

The morphologies of ZnO nanoparticles, PANI/N719/ZnO and PANI/Z907/ZnO thin films exhibit well crystalline ZnO nanoparticles of size ~30-40 nm. The size of ZnO nanoparticles increases by ~10-15 nm from their original particle sizes after the plasma enhanced chemical vapor deposition (PECVD) polymerization of PANI molecule on dye (N719 and Z907) sensitized ZnO nanoparticulate thin film. PANI/Z907/ZnO thin film displays uniform covering

or coating of PANI, indicating the well penetration of PANI on the surface of Z907/ZnO nanoparticulate thin film. The arrangement of ZnO/PANI nanoparticles are more pronounced for PANI/Z907/ZnO thin films might due to the substantive interaction and the incorporation of Z907 into ZnO nanoparticulate thin film which might allow the uniform deposition and well penetration of PANI through PECVD process. Likewise, the TEM images of ZnO nanoparticles and PANI/Z907/ZnO thin film electrode, again confirm the enhancement in the size of ZnO nanoparticles after PECVD polymerization of PANI. Significantly, after PECVD deposition of PANI, the aggregation of nanoparticles enhances the size of ZnO nanoparticles [57].

UV-Vis spectroscopy is investigated to describe the optical properties of PANI and PANI/ZnO thin film. The PECVD polymerized PANI exhibits the characteristic absorption bands at ~273 nm and ~345 nm which are ascribed to $\pi-\pi^*$ transitions. However, the broad band at ~611 nm is referred to n-π^* transitions which provides the information of the polarons formation into the conducting PANI. The UV-visible spectrum of PANI/ZnO thin film shows the clear red shifts with the absorption bands at ~299 nm and ~628 nm from ~273 and ~611 nm, indicating the interference in the absorption bands of PANI by ZnO nanoparticles. These shifts in the peaks are usually associated to the interactions between ZnO and PANI in PANI-ZnO thin film which might due to the existence of partial hydrogen bonding between NH (PANI)..O–Zn (metal oxide) [58].

The room temperature PL spectra of PECVD polymerized PANI shows two absorption bands in blue-green region at ~438 nm and ~642 nm. The significant higher absorption wavelength shift at ~452 nm with slightly decreased peak intensity is observed in the PANI/ZnO thin film. The considerable changes in the PL emission peak might arise due to the effective interaction between imine (-NH) of PANI and hydroxyl (-OH) group of ZnO nanoparicles in PECVD polymerized PANI-ZnO thin film [57].

The current density-voltage (J-V) characteristics at one sun light illumination (100 mW/cm^2, 1.5AM) have been carried out to evaluate the performances of solar cell fabricated with PANI/N719/ZnO and PANI/Z907/ZnO thin film electrode. The measurements of V_{OC}, J_{SC}, FF and overall solar-to-electrical energy conversion efficiency are obtained from the J-V characteristics of both the DSSCs. The PANI/N719/ZnO electrode based DSSC exhibits low solar-to-electricity conversion efficiency of ~0.6%, with J_{SC} of ~2.80 mA/cm^2, V_{OC} ~0.432 V and FF ~0.51, whereas, PANI/Z907/ZnO electrode based DSSC executes the greater overall solar-to-electricity conversion efficiency of ~1.31% with V_{OC} of J_{SC} ~4.56 mA/cm^2, ~0.521 V, and FF ~0.55. On comparison with PANI/N719/ZnO electrode, DSSC with PANI/Z907/ZnO electrode attains considerably improved the solar-to-electricity conversion efficiency by ~53% along with other parameters of J-V characteristics. The enhanced performances and J_{SC} might attribute to the fast movements of photon generated electrons at the interface of the PANI/ZnO and the nature of Ru dye (Z907) with long chain alkyl group at pyridine rings. Moreover, as seen in FESEM results, the high penetration of the hole conductor (PANI) into the pores of Z907 sensitized ZnO thin film might execute reasonably fast charge injection and electron transfer at the interface of PANI and ZnO layer to Pt layer of electrode. Thus, the choice of dye is crucial to obtain the high performance DSSC with PECVD polymerized PANI/ZnO electrodes. In other

http://dx.doi.org/10.5772/51432

previous report, Ameen et al showed the effects of PANI on TiO_2 as an effective photoelectrode for the performance of DSSCs [59].

A schematic energy level diagram for the device FTO/TiO_2/Dye/PANI/Pt is shown in Fig. 6 (a). The diagram, in accordance with step (1) indicates that the electrons from the dye, upon illumination, jumps from the HOMO level to the LUMO level and thus, as per step (2), these electrons are transferred from the conduction band (C.B) to the valence band (V.B) of TiO_2. The step (3) shows the transfer of electrons from V.B to the HOMO of PANI. As indicated by step (4), further transfer of electrons could be preceded through two different possible ways. Firstly, the electron could move either through the LUMO of PANI, followed by step (5) or then may jump to the LUMO of the dye and finally move onwards by repeating the step (2). Secondly, electrons, from step (3), could also jump to the HOMO of dye and would move ahead by following the same step (1), leading to the transfer of electrons to the entire cell. During the entire cycle, the recovery of the holes is accomplished at the counter electrode. Additionally, Fig. 6(b) depicts that PANI participates in the light absorption through the effective injection of electrons from its LUMO to the C.B of TiO_2. Therefore, the proposed mechanism presents that FTO/TiO_2/Dye/PANI/Pt system might deliver the high transportation of charge carriers during the operation of device under the illumination.

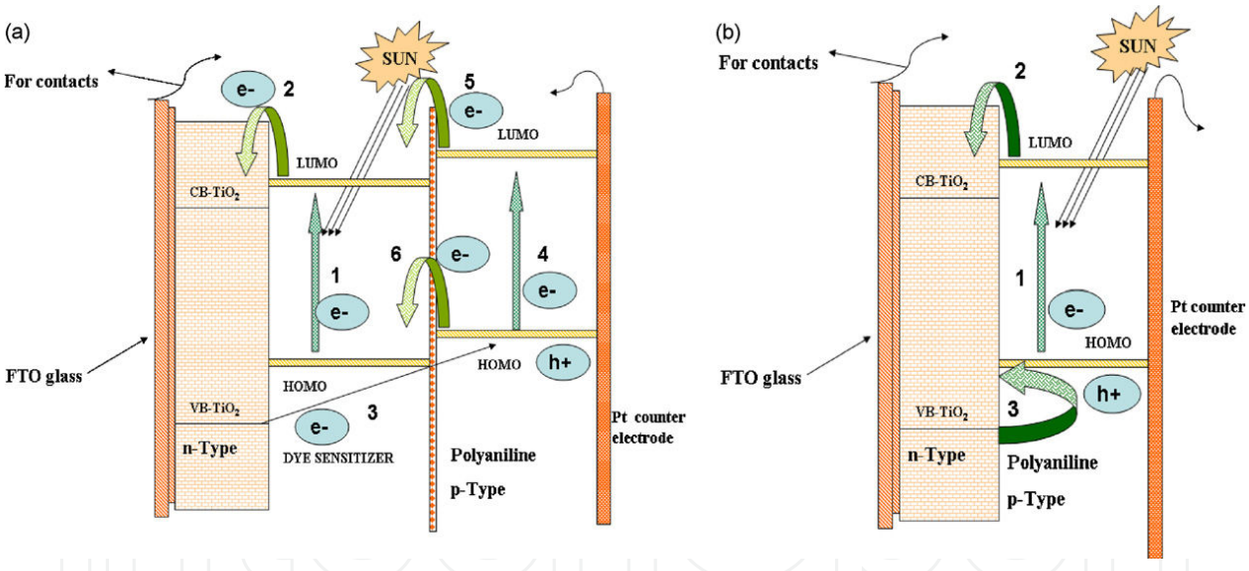

Figure 6. An overview of the energy level diagram of the fabricated devices (a) FTO/TiO_2/Dye/PANI/Pt (b) FTO/TiO_2//PANI/Pt. Reprinted with permission from [Ameen S., 2009], J. Alloys comp. 487 (2009) 382.© 2011, Elsevier Ltd.

To elucidate the charge transfer properties of TiO_2/PANI electrodes, an electrical impedance spectroscopy (EIS) measurement is used. According to the diffusion recombination model proposed by Bisquert [60], an equivalent circuit representing device is illustrated [(Inset of Fig. 7 (a)]. Equivalent circuit is composed of the series resistance (R_S), the charge transfer resistance at the junction of TiO_2 and PANI layer in TiO_2/PANI or TiO_2/Dye/PANI electrodes (R_{CT}), the charge transfer resistance at the interface of TiO_2/PANI or TiO_2/Dye/PANI and TCO ($R_{P/TCO}$), the capacitance of accumulation (of e^-) layer of the TiO_2 (C_{acc}), and space charge

capacitance ($C_{SC)}$ [61]. The values of real impedance (Z_{re}) are used to estimate the values of $R_{P/TCO}$ and R_{CT} at different frequencies. Fig. 7 (a, b) exhibits the Nyquist curve of cell fabricated with TiO_2/PANI and TiO_2/Dye/PANI electrodes. A very high $R_{P/TCO}$ of 52.4Ω and R_{CT} of 3700 Ω observed for TiO_2/PANI electrodes based cells, which are estimated from Fig. 7(a). Comparatively, TiO_2/Dye/PANI based device (Fig.7 (b)) shows the low $R_{P/TCO}$ (35.8 Ω) and R_{CT} (81.9 Ω) due to the influence of dye layer which is placed between the TiO_2 and PANI layer of the electrode. It is reported that a small R_{CT} of the device suggests the fast electron transfer, while a large R_{CT} indicates the slow charge transfer at the junction of inorganic and organic layer [62]. In our case, it is found that the value of R_{CT} in TiO_2/Dye/PANI based device is very low as compared to the R_{CT} of TiO_2/PANI based device. Therefore, it explains the high electron transfer at the junction of TiO_2 and PANI in TiO_2/Dye/PANI based device, resulting in the high photocurrent density and overall conversion efficiency, which are in the excellent agreement with the J-V curve results of the devices. The impedance results clearly indicate that the high photocurrent density, high overall conversion efficiency and low R_{CT} are resulted from the uniform distribution of PANI molecules on the mesoporous surface of TiO_2 electrode. Therefore, the lower R_{CT} and $R_{P/TCO}$ in TiO_2/Dye/PANI based device reveals that the dye and PANI layers on the surface of TiO_2 electrode play an important role in the charge transfer at hole conductor (PANI)-dye absorbed TiO_2 region, which results the high J_{SC}, FF, and conversion efficiency than that of TiO_2/PANI electrode based cells.

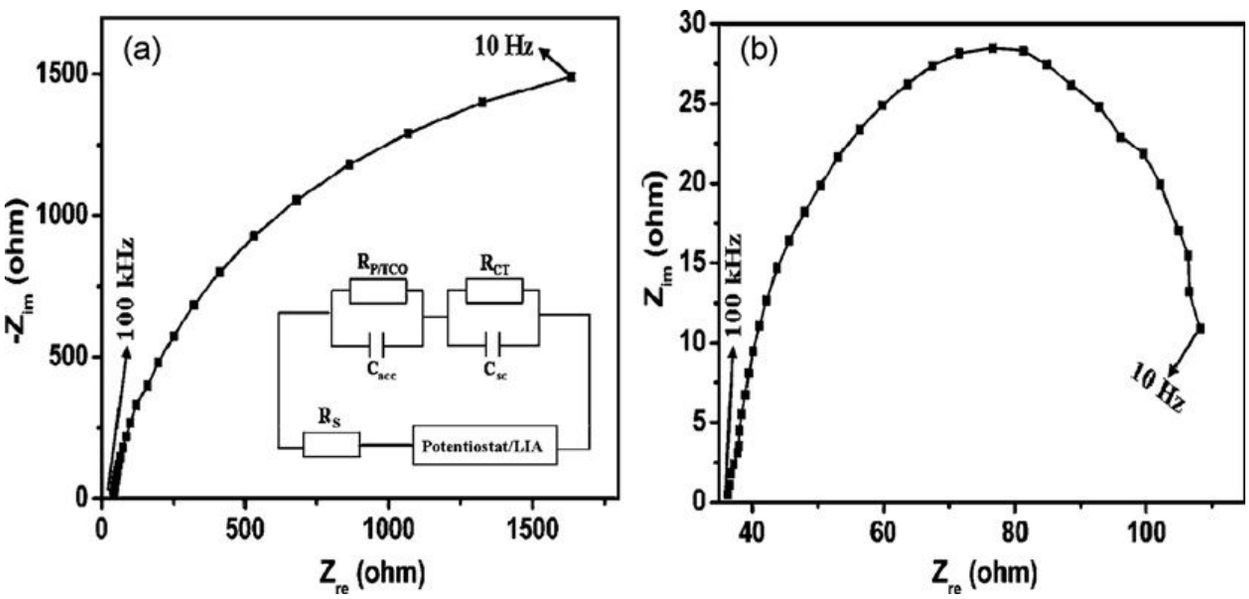

Figure 7. AC impedance of (a) FTO/TiO_2/PANI/Pt and (b) TiO_2/Dye/PANI thin film electrode based DSSCs at the frequency range from 10 Hz to 100 kHz. Inset shows the equivalent circuit model of the device. Reprinted with permission from [Ameen S., 2009], J. Alloys comp. 487 (2009) 382. ©2011, Elsevier Ltd.

The J-V performance of solar cell FTO/TiO_2/Dye/PANI/Pt and FTO/TiO_2/PANI/Pt are shown in Fig. 8 (a, b) under 100 mW/cm^2 light intensity. On comparison with TiO_2/PANI, the solar cell based on TiO_2/Dye/PANI electrode executes great improvement in the overall conversion efficiency with the incorporation of dye layer on TiO_2/PANI electrode. The conversion

http://dx.doi.org/10.5772/51432

efficiency of the solar cell drastically increases from ~0.005% to ~0.68%. It is noteworthy that the photovoltaic properties such as V_{OC}, J_{SC} and FF of the DSSCs enhance dramatically as compared to TiO_2/PANI electrode based DSSC. The high J_{SC} is imputed to the high electrical conductivity of PANI/TiO_2 thin film. The enhancement in JV parameters are resulted from the formation of TiO_2/PANI thin film, where the photon generated electrons could freely travel at the interface of PANI and TiO_2 without decay, and dissociate into free charge carriers effectively. Moreover, the pore filling extent of the hole conductor into the dye-sensitized TiO_2 film, and the electric contact of the hole conductor are the two important factors to determine the photovoltaic behaviors of device. The advanced TiO_2/Dye/PANI electrode executes reasonably fast charge injection and transfer of electron at the interface of hole conductor (PANI) and Pt layer of electrode.

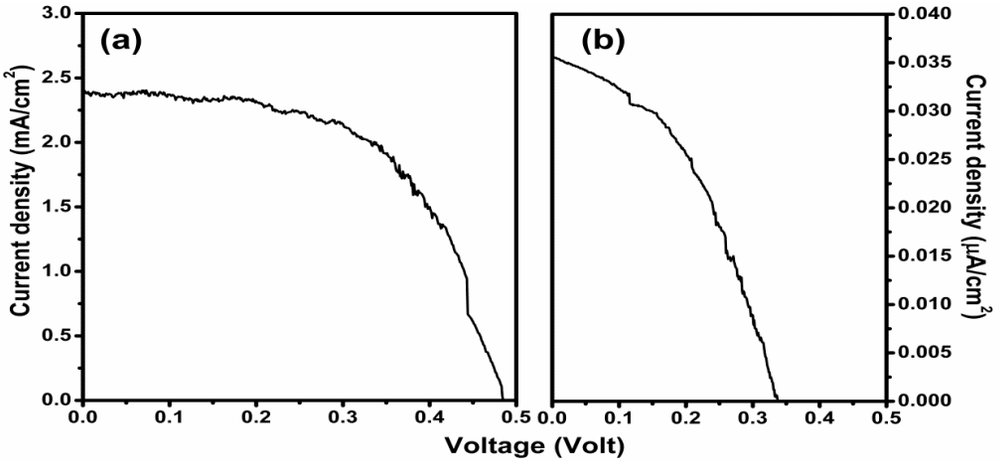

Figure 8. J–V curve of fabricated solar cell (a) FTO/TiO_2/Dye/PANI/Pt (b) FTO/TiO_2//PANI/Pt. Reprinted with permission from [Ameen S., 2009], J. Alloys comp. 487 (2009) 382 ©2011, Elsevier Ltd.

5.2. PANI as counter electrodes for DSSCs

The counter electrode in DSSCs is responsible for the electrocatalytic reduction of I_3^- ions. Until now, Pt counter electrode shows the high electrocatalytic activity for I_3^- ions reduction, high conductivity, and stability. Pt is one of the most expensive components in DSSCs. Therefore, the development of counter electrodes with alternative materials is expected to reduce production costs of DSSCs. Several varieties of materials such as carbon nanotubes, activated carbon, graphite, and conducting polymers are employed as active catalysts for counter electrodes. In this regards, M. H. Yeh et al reported the conducting polymer-based counter electrode for a quantum-dot-sensitized solar cell (QDSSC) with a polysulfide electrolyte [63]. K. M. Lee et al fabricated the DSSC based on poly (3, 4-alkylenedioxythiophene) as counter electrode [64]. In another report, K. M. Lee et al exhibited the effects of mesoscopic poly (3, 4-ethylenedioxythiophene) films as counter electrodes for DSSCs [65]. W. Maiaugree et al optimized the TiO_2 nanoparticle mixed PEDOT-PSS counter electrodes for high efficiency of DSSCs [66]. J. Chen et al reported polyaniline nanofiber-carbon film as flexible counter electrodes in platinum-free dye-sensitized solar cells [67]. Q. Li et al fabricated the microporous

polyaniline thin film as counter electrode for DSSCs [68]. J. Zhang et al applied the nanostructured PANI thin film as counter electrode for DSSCs and investigated the electrochemical formation mechanism [69]. Furthermore, G. Wang et al synthesized PANI-graphene hybrids thin film and utilized as a counter electrode in DSSCs [70]. Tai et al prepared the highly uniform and transparent PANI counter electrodes by a facile in situ polymerization method for the DSSCs [71]. In this regards, Ameen et al performed the doping of PANI with sulfamic acid (SFA) and applied as counter electrode for the efficient performance of DSSCs [72].

Fig. 9(a) shows the J-V curve of the DSSCs fabricated with the counter electrodes made of PANI NFs and SFA-doped PANI NFs under dark and light intensity of 100 mW/cm^2 (1.5AM). DSSCs fabricated with SFA-doped PANI NFs counter electrode achieve high conversion efficiency (η) of ~5.5% with J_{SC} of ~13.6 mA/cm^2, V_{OC} of ~0.74 V, and FF of ~0.53. Significantly, the conversion efficiency increases from ~4.0% to ~5.5% after SFA doping into the PANI NFs. DSSC fabricated with SFA-doped PANI NFs counter electrode has appreciably improved the conversion efficiency and J_{SC} by ~27% and ~20% than that of DSSC fabricated with PANI NFs counter electrode. These improvements are resulted from the higher electrocatalytic activity of SFA-

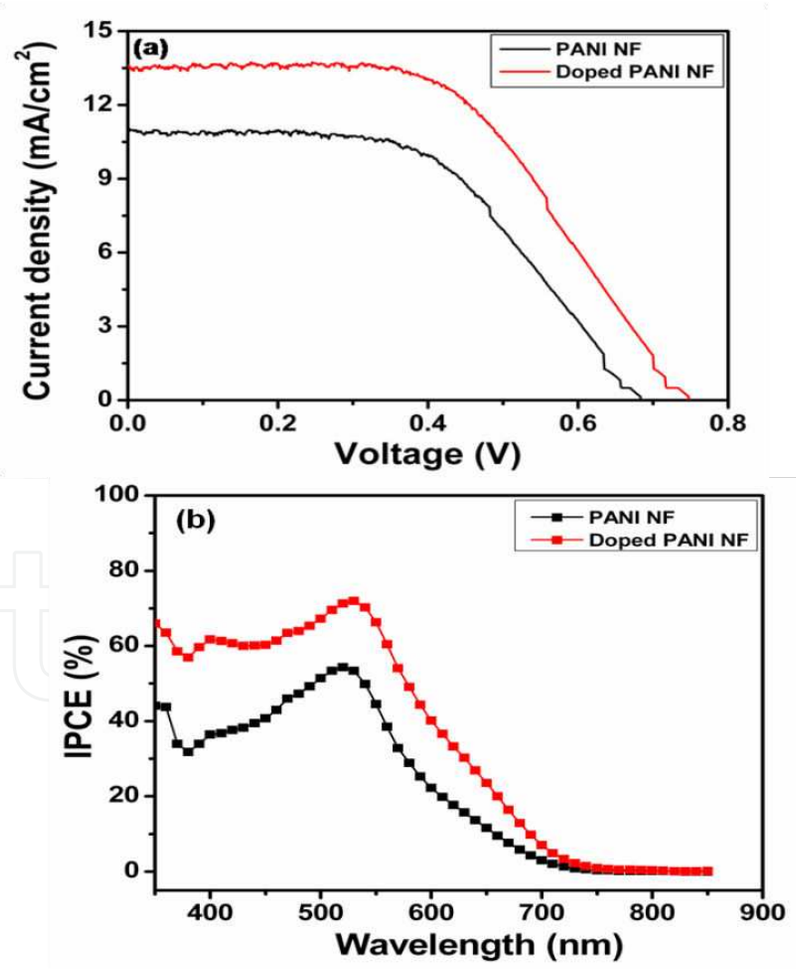

Figure 9. J-V curve (a) and IPCE curves (b) of a fabricated solar cell of PANI NFs and SFA doped PANI NFs as counter electrodes. Reprinted with permission from [Ameen S., 2010], J. Phys. Chem. C 114 (2010) 4760. ©2010, American Chemical Society.

http://dx.doi.org/10.5772/51432

doped PANI NFs, which serves a good path for the charge transport of I^-/I_3^- redox. Therefore, the superior photovoltaic properties such as η, J_{SC}, and V_{OC} of the cell are attributed to the sufficiently high conductivity and electrocatalytic activity of doped PANI NFs, which alleviates the reduction of I_3^- at the thin SFA-doped PANI NFs layers. Fig. 9(b) presents the IPCE curves of DSSCs fabricated with PANI NFs and SFA-doped PANI NFs counter electrodes. DSSCs fabricated with PANI NFs counter electrode exhibits the low IPCE of ~54% in the absorption range of 400-650 nm. The IPCE value is prominently increased by ~70% with the SFA doped PANI NFs counter electrode-based DSSCs. It is noteworthy that the IPCE of the device is considerably enhanced by ~24% upon SFA doping on PANI NFs-based counter electrodes. The enhanced IPCE results are consistent with high electrical conductivity [73] and the electrocatalytic activity of the SFA-doped PANI NFs electrode. Thus, SFA doping significantly enhances the electrical conductivity and increases the higher reduction of I_3^- to I^- in the electrolyte at the interface of PANI NFs layer and electrolyte.

5.3. Other ions doped PANI counter electrode based DSSCs

Z. Li et al recently studied on the in situ electropolymerized-PANI thin film of thickness ~5–20 μm, deposited on FTO glass. The PANI thin films were doped by various counter ions like SO_2^{-4}, ClO^{-4}, BF^{-4}, Cl^-, p-toluenesulfonate (TsO^-), etc. Different doping counter ions showed different impact on the morphology, electrochemical activity of the electropolymerized-PANI thin film. The electropolymerized-PANI doped by SO_2^{-4} anion (PANI-SO_4) film was much porous morphology with pore size diameter of several micrometers and possessed the higher reduction current for the reduction of I_3^- and a low charge transfer resistance of 1.3 Ωcm^2 as compared with Pt as counter electrode (CE). Dye-sensitized solar cell (DSSC) with PANI-SO_4 as CE was assembled, and the device under full sunlight illumination (100mWcm^{-2}, AM 1.5 G) showed ~5.6% photovoltaic conversion efficiency, which was comparable to ~6.0% of that with Pt CE under the same experimental condition. The electropolymerized-PANI doped with SO_2^{-4} ion with a porous and homogeneously structure was a promising candidate which showed the high performance of DSSC. On the other hand, PANI-BF_4 and PANI-Cl was porous and fibrillar thin film which exhibited the modest efficiency of ~3.9% and ~2.6%. On the other hand, PANI-ClO_4 and PANI-TsO showed the very low performance of DSSC ca. <1%, and the R_{CT} was greatly increased accordingly to over 100 Ωcm^2 [74].

6. DSSCs based on metal oxide semiconductors

In DSSCs, the choice of semiconductor is governed by the conduction band energy and density of states, which facilitate the charge separation and minimize the recombination. Secondly, the high surface area and morphology of semiconductors is important to maximize the light absorption by the dye molecules while maintaining the good electrical connectivity with the substrate [75]. The semiconducting metal oxides such as titania (TiO_2), zinc oxide (ZnO), and tin oxide (SnO_2) have shown good optical and electronic properties and are accepted as the effective photoelectrode materials for DSSCs. To improve the light harvesting efficiency, the metal oxide nanostructures must possess a high surface-to-volume ratio for high absorption of dye molecules. Particularly in DSSCs, the porous nature of nanocrystalline TiO_2 films

provides the large surface for dye-molecule adsorption and therefore, the suitable energy levels at the semiconductor-dye interface (the position of the conduction band of TiO_2 being lower than the excited-state energy level of the dye) allow for the effective injection of electrons from the dye molecules to the semiconductor. Compared with other photovoltaic materials, anatase phase TiO_2 is outstanding for its stability and wide band gap and, thus, widely used in the devices [76]. On the other hand, ZnO nanomaterials are chosen as an alternative material to TiO_2 photoanodes due to their wide band gap with higher electronic mobility, which would be favorable for the efficient electron transport, with reduced recombination loss in DSSCs. Studies have already been reported on the use of ZnO material photoanodes for the application in DSSCs. Although the conversion efficiencies of ZnO (0.4-5.8%) is comparably lower than TiO_2 (~11%), ZnO is still a distinguished alternative to TiO_2 due to its ease of crystallization and anisotropic growth. In this part of the chapter, the TiO_2 and ZnO have been briefly summarized for the application for DSSCs.

6.1. DSSCs Based on TiO_2 Photoanode

Due to versatile and the exotic properties, TiO_2 nanomaterials are so far used in many technological applications as a photocatalyst, photovoltaic material, gas sensor, optical coating, structural ceramic, electrical circuit varistor, biocompatible material for bone implants, and spacer material for magnetic spin valve systems etc [77]. The dimensionality of TiO_2 at the nanoscale level is the crucial characteristic for determining the physiological and electrical properties. In recent years, one dimensional (1D) TiO_2 nanomaterials like NRs, NWs and NTs display significantly larger surface areas as compared to bulk materials, which deliver unique chemical and the physical properties [78] and contribute towards the electrical and photoelectrochemical applications [79]. The 1D TiO_2 such as NRs and NTs have shown the reduced recombination rate for the excited electron-hole pair and display unique optical and the electric properties [80]. Particularly, the vertically grown TiO_2 NRs allow shorter and the uninterrupted electrical pathways for the photogenerated carriers and improves the charge separation and charge transport properties in many photoelectrochemical devices like dye sensitized solar cells (DSSCs) [81]. As compared to TiO_2 nanoparticles, it is expected that the highly oriented TiO_2 NRs could be the potential electrode and photocatalyst material for several photoelectrochemical applications. S. Ameen et al reported the TiO_2 nanorods (NRs) based photoanode for the fabrication of DSSCs [82].

The morphology of the TiO_2 NR thin films deposited on FTO substrates by the hydrothermal process with variations of the ethanol/DI water precursor solution is shown in FESEM images (Fig. 10). With an ethanol/DI water ratio of 0:100 v/v as the precursor solution, the distorted hexagonal TiO_2 NRs (Fig. 10 (a, b)) of average diameter ~100-200 nm and length of 3.0 mm are obtained. However, the round headed TiO_2 NRs with ethanol/DI water (50: 50 v/v) as the precursor solution (Fig. 10 (c, d)) is formed. The highly ordered tetragonal TiO_2 NRs have grown on the FTO substrate with the precursor solution of ethanol/DI water (80: 20 v/v) as seen in Fig. 10 (e, f). The grown TiO_2 NRs possess the average lengths of 2-4 mm and diameters of ~50–70 nm respectively. The high amount of ethanol in the precursor solution is crucial to achieve the highly ordered nanorods.

http://dx.doi.org/10.5772/51432

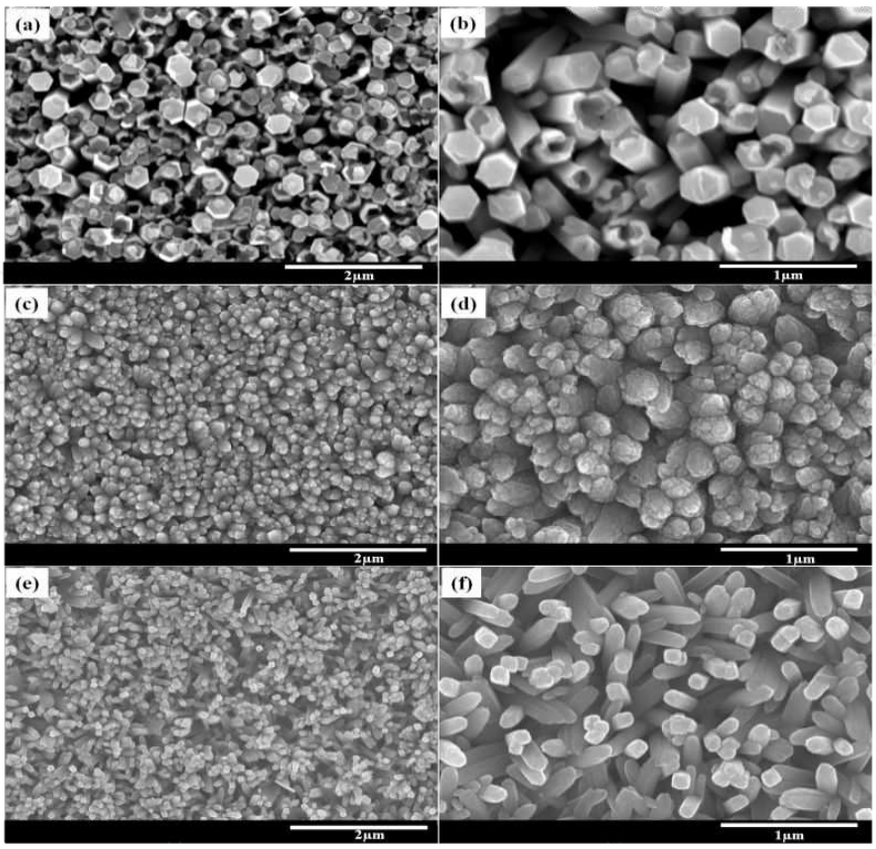

Figure 10. Low and high resolution FESEM images of the TiO_2 NR thin films obtained with the precursor solutions of ethanol/DI water with ratios of (a, b) 0 : 100 v/v, (c, d) 50 : 50 v/v and (e, f) 80 : 20 v/v. Reprinted with permission from [Ameen S., 2012], RSC Adv. 2 (2012) 4807 ©2012, RSC Publications Ltd.

Fig. 11 shows the transmission electron microscopy (TEM), high resolution (HR) TEM and the selected area electron patterns (SAED) of the grown TiO_2 NR coated FTO substrate. Similar to the FESEM results, the highly ordered tetrgonal TiO_2 NRs from the precursor solution of ethanol/DI water (80:20v/v) solvent comprises the average length of 2-4 mm and the diameter of 50-70 nm, as shown in Fig. 11 (a). Each NR is made of a bundle of the densely packed nanofibers (NFs) with an average fibril's diameter of ~5 nm. The corresponding SAED pattern (Fig. 11 (b)) displays the clear phases, suggesting the high crystal quality with the single crystalline fibrils derived from TiO_2 NRs along the [001] direction. However, the HRTEM image (Fig. 11 (c)) shows the well-resolved lattice fringes of the grown TiO_2 NRs and estimates an average interplanar distance of 0.35 nm between the two fringes, which reveals the typical interplanar distance of anatase TiO_2 [83]. On the other side, the width and length of distorted hexagonal TiO_2 NRs are respectively observed as ~200 nm and ~3.2 mm, as seen in Fig. 11(d).

The XRD patterns (Fig. 12) of grown TiO_2 NRs from both precursor solutions exhibit the anatase phase with the peaks at 25.1°, 37.9°, 48.1°, 53.8° and 55.1°, which correspond to typical anatase TiO_2 materials and indexes at JCPDS no. 89-4203. However, the diffraction peaks of the FTO substrate are also observed at 33.8°, 35.7° and 52.8° (JCPDS no. 88-0287). On comparison with the distorted hexagonal TiO_2 NRs, the intensities of XRD diffraction peaks have slightly changed, which might indicate the high crystalline nature of the highly ordered tetragonal TiO_2 NRs.

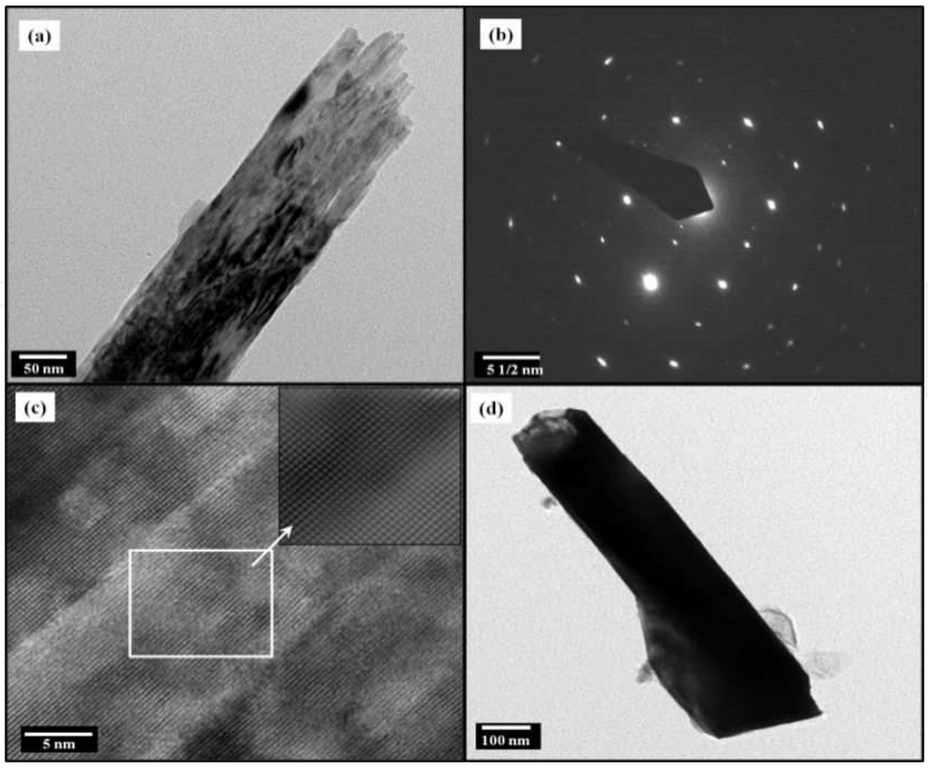

Figure 11. TEM image of (a) highly ordered tetragonal TiO_2 NRs, (b) SAED patterns, (c) HRTEM image and (d) TEM image of grown hexagonal distorted TiO_2 NRs. Reprinted with permission from [Ameen S., 2012],], RSC Adv. 2 (2012) 4807 ©2012, RSC Publications Ltd.

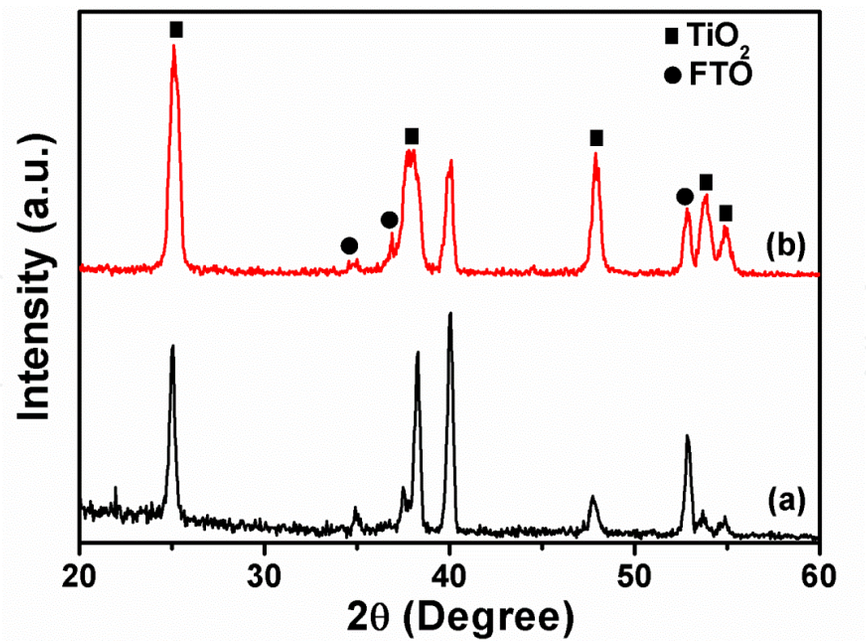

Figure 12. XRD patterns of (a) the distorted hexagonal TiO_2 NRs and (b) the highly ordered tetragonal TiO_2 NR thin film. Reprinted with permission from [Ameen S., 2012], RSC Adv. 2 (2012) 4807 ©2012, RSC Publications Ltd.

http://dx.doi.org/10.5772/51432

The J-V characteristics (Fig. 13 (A)) have been performed to elucidate the performance of the DSSCs fabricated with the photoanodes of grown TiO_2 NRs and are measured under a light intensity of 100 mW cm^{-2} (1.5 AM). DSSC fabricated with the distorted hexagonal TiO_2 NRs photoanode shows a relatively low solar efficiency of ~1.08%, with a low J_{SC} of ~4.48 mA cm^{-2}, V_{OC} ~0.571 V and FF of ~0.42. However, DSSCs fabricated with the highly ordered tetragonal TiO_2 NRs photoanode achieves an appreciably improved overall conversion efficiency of ~3.2% with a high J_{SC} of ~8.7 mA cm^{-2}, V_{OC} of ~0.67 V, and FF of ~0.54. As compared to the distorted hexagonal TiO_2 NRs photoanode based DSSC, the photovoltaic performance, J_{SC}, V_{OC} and FF are significantly enhanced by ~ 67%, ~48%, ~15% and ~22% respectively. It is seen that the size of the NRs also plays an important role for achieving the high photocurrent density and performance of the device. It is known that the high photovoltaic performance and photocurrent density are related to high light harvesting through the highly uniform and high surface to volume ratio of the photoanode materials [84]. In general, the TiO_2 thin film electrodes with larger particles have the smaller surface area and produce moderate contact points between nanoparticles at the interface of the sintered nanoparticles and the conducting substrate, leading to the lower availability of the active surface for dye adsorption, which perhaps decreases the amount of light absorbed and generates the large number of electrons and holes. Whereas, the TiO_2 thin film with smaller particles acquires the larger surface area and higher number of contact points of the sintered colloidal particles present at the interface of the nanoparticles and the conducting substrate, which gives rise to larger dye adsorption and higher light harvesting efficiency [85]. In this case, the distorted hexagonal TiO_2 NRs consist of larger diameters and lengths as compared to the highly ordered TiO_2 NRs, as shown in the FESEM images. It is believed that the smaller diameters of the NRs might generate the high light harvesting efficiency, which might lead to the high photocurrent density and the conversion efficiency. From the UV-Vis spectra (Fig. 13 (B)) of the dye desorption from dye absorbed TiO_2 NRs photoanodes in NaOH solution, the photoanode of highly ordered tetragonal TiO_2 NRs attains the higher dye loading than the photoanode of the distorted hexagonal TiO_2 NRs. Herein, the enhanced photovoltaic performance and J_{SC} are related to the highly ordered NRs morphology, high dye loading and improved light harvesting efficiency through the high surface area of the film. Besides these, the unique ordered morphology of the NRs might retard the recombination rate and contribute to longer electron lifetimes [86], resulting in the increased V_{OC} and FF of device.

The IPCE (Fig. 14) of DSSCs fabricated with highly ordered tetragonal TiO_2 NRs and distorted hexagonal TiO_2 NRs photoanodes have shown the broad the absorption edge of visible spectrum from 400-800 nm. The highly ordered tetragonal TiO_2 NRs photoanode based DSSC exhibits the maximum IPCE of ~31.5% at the highest absorption edge of ~528 nm, whereas ~17.9% IPCE at ~528 nm is achieved by the distorted hexagonal TiO_2 NRs photoanode based DSSC. The highly ordered tetragonal TiO_2 NRs photoanode based DSSC considerably improves IPCE by approximately two times to DSSC with distorted hexagonal TiO_2 NRs photoanode, which is attributed to the high dye loading of the photoanode, resulting in the high light harvesting efficiency and the electron injection from dye to CB of TiO_2. Thus, the highly ordered tetragonal TiO_2 NRs photoanode with enhanced dye loading, light harvesting and IPCE, have resulted to increased J_{SC}, V_{OC} and the photovoltaic performance for DSSC.

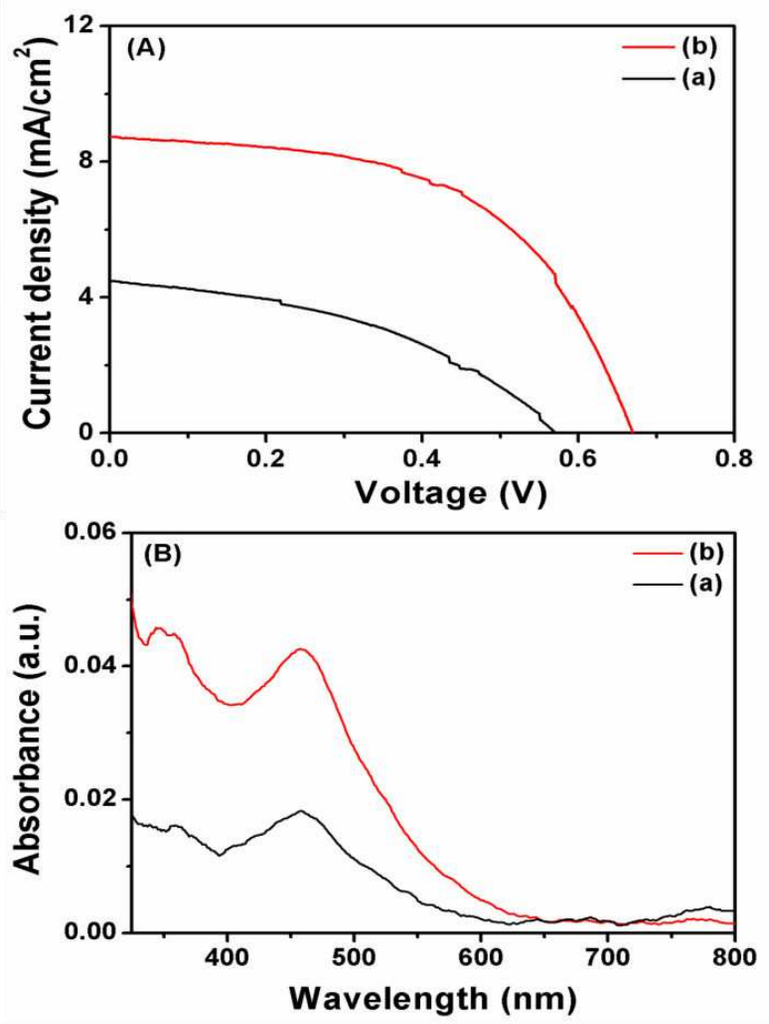

Figure 13. (A) J-V curve of the DSSC fabricated with (a) distorted hexagonal TiO_2 NRs and (b) highly ordered tetragonal TiO_2 NRs. (B) UV-Vis spectroscopy of desorbed dye from (a) distorted hexagonal TiO_2 NRs and (b) highly ordered tetragonal TiO_2 NRs. Reprinted with permission from [Ameen S., 2012]], RSC Adv. 2 (2012) 4807©2012, RSC Publications Ltd.

6.2. DSSCs based ZnO photoanode

Another metal oxide nanomaterials such as ZnO nanomaterials, are recently dealing with the versatile applications in various fields such as field-effect transistors, lasers, photodiodes, sensors and photovoltaics owing to their unique photoelectric properties, optical transparency, electric conductivity and piezoelectricity properties [87]. Importantly, ZnO nanomaterials possess similar wide band gap (~3.37 eV) with large exciton binding energy (~60 meV) and higher electron mobility [88]. Moreover, ZnO nanomaterials with different nanostructures have presented the versatile properties like higher surface-to-volume ratio, chemical stability, high exciton binding energy, and moderate charge transport capability [89] and therefore, it becomes one of the promising alternatives of nanocrystalline TiO_2 photoanode in DSSCs and hybrid solar devices. To control the parameters like morphology, physical and the crystalline properties of ZnO nanomaterials, the performance of DSSCs could be accelerated [90]. So far, the different morphologies of ZnO nanostructures such as nanorods [91], nanotetrapods,

http://dx.doi.org/10.5772/51432

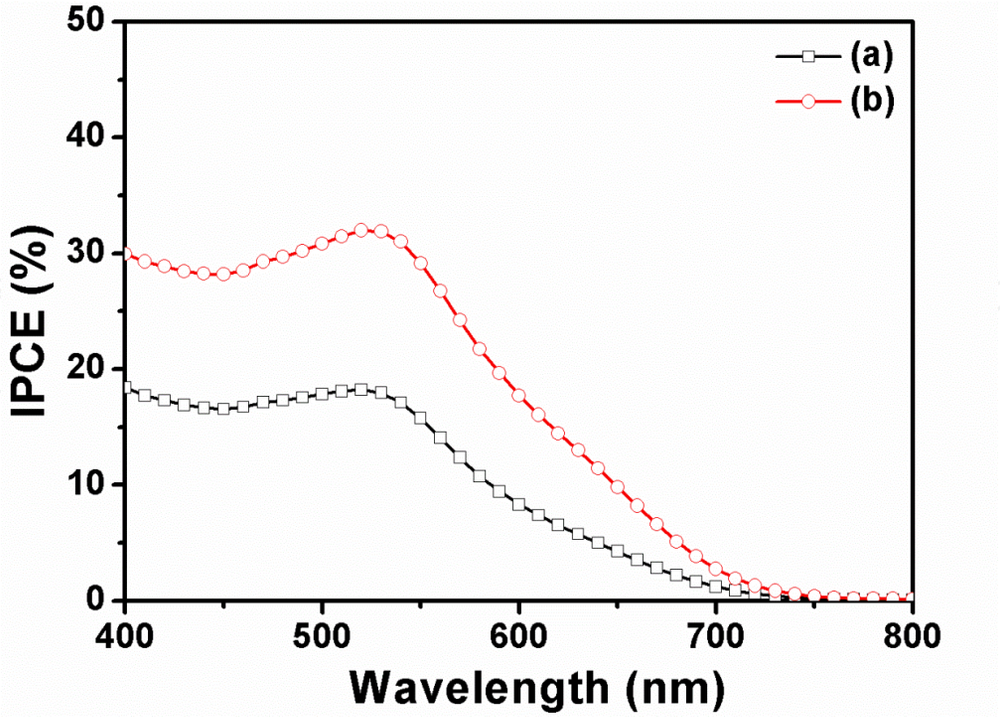

Figure 14. IPCE curve of the DSSC fabricated with (a) the distorted hexagonal TiO_2 NR photoanode and (b) the highly ordered tetragonal TiO_2 NR photoanode. Reprinted with permission from [Ameen S., 2012], RSC Adv. 2 (2012) 4807©2012, RSC Publications Ltd.

nanosheet [92] and nanobelts based photoanodes have been studied for the fabrication of efficient DSSCs [93] and achieved encouraging results. Law et al. firstly designed ZnO NW arrays to increase the electron diffusion length, and applied as photoelectrodes for the fabrication of DSSCs [94]. The grown ZnO NW array films exhibited relatively good resistivity values that ranged from 0.3 to 2.0 Ωcm for individual NWs and a mobility of 1-5 $cm^2\ V^{-1}s^{-1}$. The overall conversion efficiencies of ~1.2-1.5% were obtained by DSSCs fabricated with ZnO NW arrays with J_{SC} of ~5.3-5.85 mA/cm^2, V_{OC} of ~0.610-0.710 V, and FF of ~0.36-0.38. Another

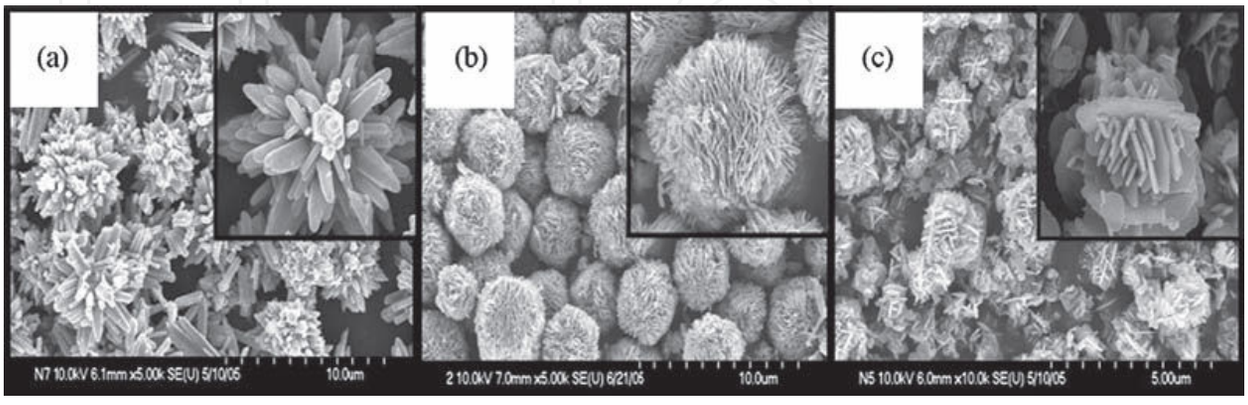

Figure 15. FE-SEM images of (a) ZnO–NH3, (b) ZnO-citric, and (c) ZnO-oxalic materials prepared by hydrothermal method. Inset shows the high magnification FE-SEM images of (a), (b), and (c). Reprinted with permission from [Akhtar., 2008], Electrochim. Acta 53(2008)7869.© 2008, Elsevier Ltd.

group synthesized ZnO NWs by the use of ammonium hydroxide for changing the super saturation degree of Zn precursors in solution process [95]. The length-to-diameter aspect ratio of the individual NWs was easily controlled by changing the concentration of ammonium hydroxide. The fabricated DSSCs exhibited remarkably high conversion efficiency of ~1.7%, which was much higher than DSSC with ZnO NR arrays [96]. Jiang et al. fabricated the flexible DSSCs with a highly bendable ZnO NWs film on PET/ITO substrate which was prepared by a low-temperature hydrothermal growth at 85^{o}C [97]. The fabricated composite films obtained by immersing the ZnO NPs powder in a methanolic solution of 2% titanium isopropoxide and 0.02 M acetic acid was treated with heat, which favored a good attachment of NPs onto the NW surfaces [97]. Here, the achieved conversion efficiency of the fabricated DSSCs was less as compared to DSSCs based on NPs. Recently, Akhtar et al. demonstrated that the performance of DSSCs effectively altered by varying the morphologies of ZnO nanomaterials. They reported the morphology of ZnO nanomaterials through a hydrothermal process using Zinc acetate, NaOH and different capping agents, as shown in Fig 15. The photoanode was prepared by spreading the ZnO paste on an FTO substrate by a doctor blade technique for the fabrication of DSSCs [98], and they obtained non-uniform surface of film. Unfortunately, the DSSCs with ZnO NRs photoanode presented a very low conversion efficiency of ~0.3% with a high FF of ~0.54 (Fig 16), which might attribute to the low dye absorption on the surface of ZnO NRs due to the less uniformity of the thin film with low surface-to-volume ratio (Fig 17). Furthermore, a flower-like structure consisted of NRs/NWs could deliver a larger surface area and a direct pathway for electron transport with the channels arisen from the branched to NR/NW backbone. Recently, hydrothermally grown ZnO nanoflower films accomplished an improved overall conversion efficiency of ~1.9%, with a high J_{SC} of ~5.5 mA/cm^2 and an FF of ~0.53 [99]. These parameters are higher than NR arrays film-based DSSCs of the conversion efficiency ~1.0%, J_{SC} ~4.5 mA/cm^2, and FF ~0.36. Recently, S. Ameen et al reported the nanospikes decorated ZnO sheets thin film as photoanode for the performance of DSSCs [100].

The FESEM image (Fig. 18) shows dense and uniform deposition of the nanospikes decorated ZnO sheets morphology on the FTO substrate. Each nanospikes decorated ZnO sheets is comprised of a sheet with the average thickness of ~50-60 nm and the aligned nanospikes with the average diameter of ~80-100 nm and length of ~150-200 nm. Interestingly, the nanospikes are consisted of the bundles of small nanorods. The nanospikes are aligned either on one side or other side of ZnO sheet, but in some cases, these nanospikes are found on the both sides of ZnO sheets.

Similarly, TEM images (Fig. 19(a)) present the nanospikes with nanosheets in which nanospikes decorated on both the sides of ZnO sheet. The average thickness of the sheet is ~50-60 nm and the decorated nanospikes possess the average diameter of ~30 nm (single rods) and the length of ~150-200 nm. From the HRTEM image (Fig. 19 (b)), the well-resolved lattice reveals that the grown ZnO nanomaterials exhibit the good crystallinity. The inter-planar spacing of ~0.52 nm is observed which is consistent to the lattice constant in the reference (JCPDS No. 36-1451) for ZnO nanomaterials. This inter-planar spacing value of the lattice fringes correspond to the [0001] crystal plane of the wurtzite ZnO confirms that the grown ZnO nanomaterials are almost defect free [100]. Moreover, the corresponding selected area electron diffraction (SAED) also indicates the typical wurtzite single crystalline structure and the ZnO nanomaterials are grown along caxis direction [0001].

http://dx.doi.org/10.5772/51432

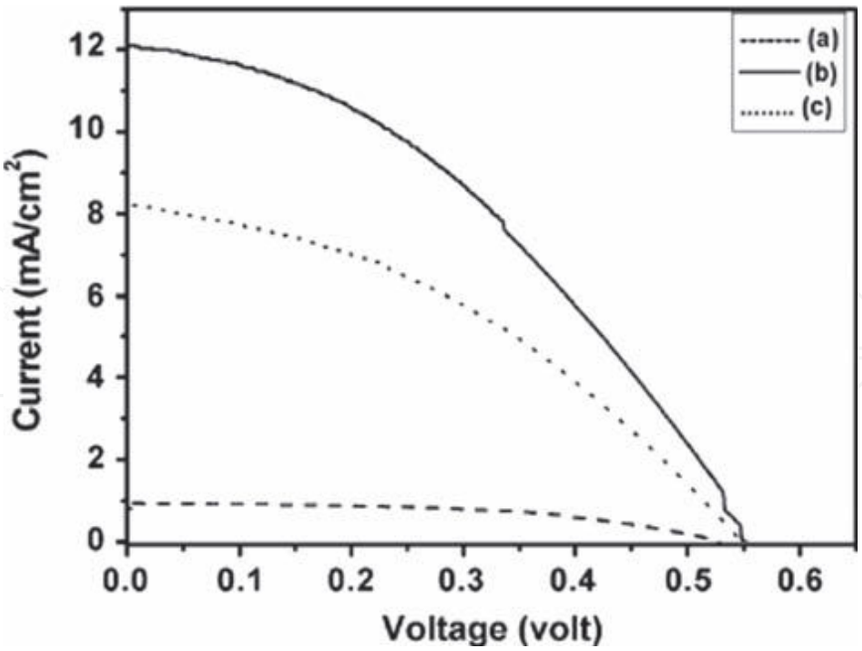

Figure 16. Current–voltage curve of DSSC fabricated with (a) ZnO–NH_3, (b) ZnO-citric, and (c) ZnO-oxalic at 1.5 AM. Reprinted with permission from [Akhtar., 2008], Electrochim. Acta 53, (2008) 7869.© 2008, Elsevier Ltd.

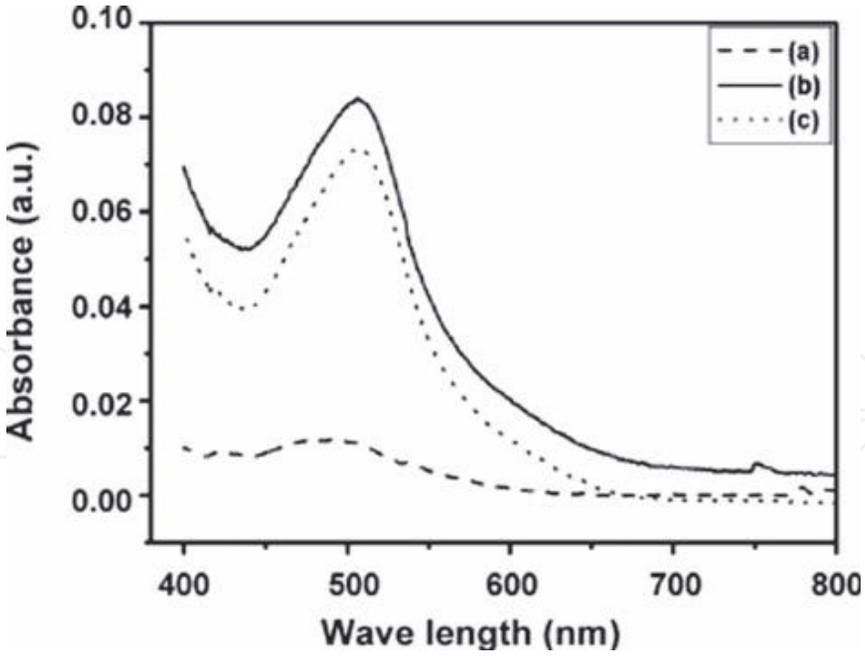

Figure 17. UV-vis absorption of dye (N-719) extracted with 2 M NaOH from the electrodes of (a) ZnO–NH_3, (b) ZnO-citric, and (c) ZnO-oxalic. Reprinted with permission from [Akhtar., 2008], Electrochim. Acta 53 (2008) 7869.© 2008, Elsevier Ltd.

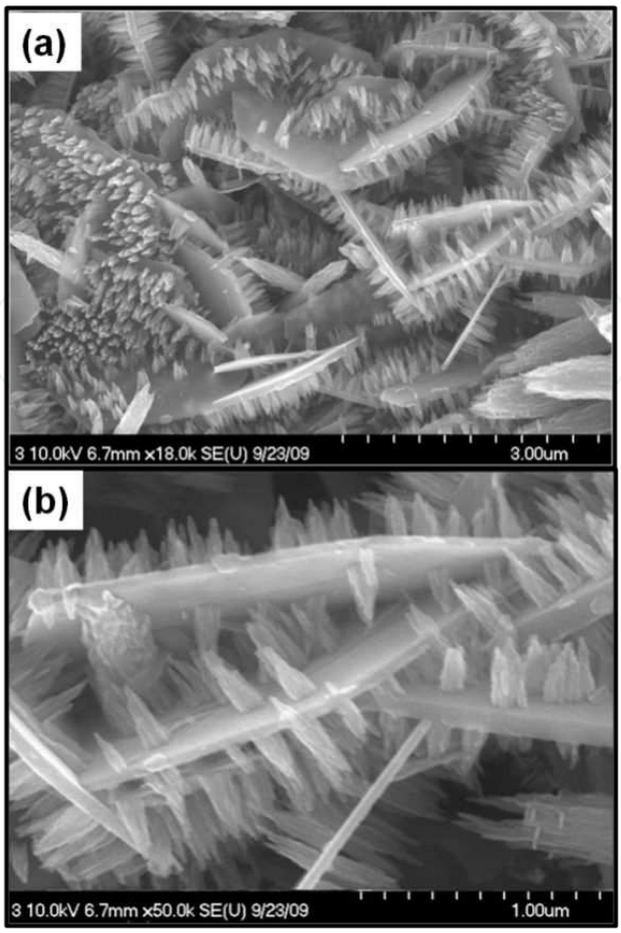

Figure 18. FESEM images of nanospikes decorated ZnO sheets (a) at low magnification and (b) at high magnification. [Ameen S., 2012], Chem. Eng. J. 195 (2012) 307©2012. Elsevier Ltd.

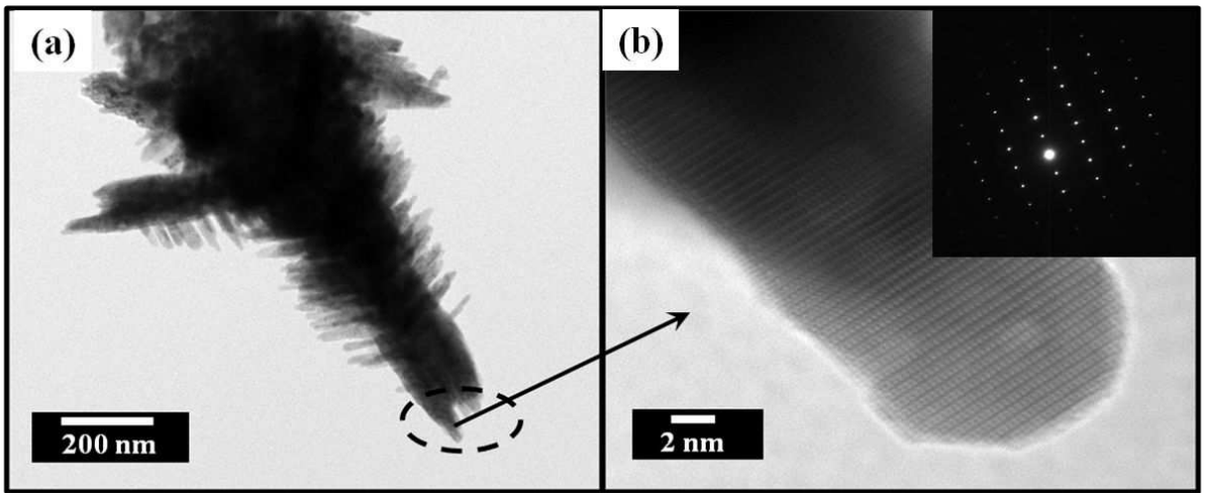

Figure 19. TEM image (a) and HR-TEM image (b) of grown nanospikes decorated ZnO sheets. Inset shows the corresponding SAED patterns of grown nanospikes decorated ZnO sheets. Reprinted with permission from [Ameen S., 2012], Chem. Eng. J. 195 (2012) 307 ©2012, Elsevier Ltd.

http://dx.doi.org/10.5772/51432

XRD patterns (Fig. 20 (a)) of the nanospikes decorated ZnO sheets obtain all the diffraction peaks appeared at 32.3° (100), 35.2° (002), 36.8° (101), 48.2° (102), 57.2° (110), 63.5° (103) and 66.2° (200) which are well matched with the JCPDS card No.36-1451. It confirms that the ZnO nanomaterials possess the hexagonal wurtzite phase with the lattice parameters: a-3.246 and c-5.206 Å. The intensity of (101) diffraction peak is much higher compared to other peaks, indicating the preferential growth direction due to the instability of polar (101) plane [101]. A single narrow absorption peak is observed near the UV region at ~376 nm in the UV-Vis absorbance spectrum of nanospikes decorated ZnO sheets structures (Fig. 20 (b)), corresponds to the characteristic band of the wurtzite hexagonal structure in bulk ZnO [102]. Moreover, the single peak suggests purity of the grown nanospikes decorated sheets morphology.

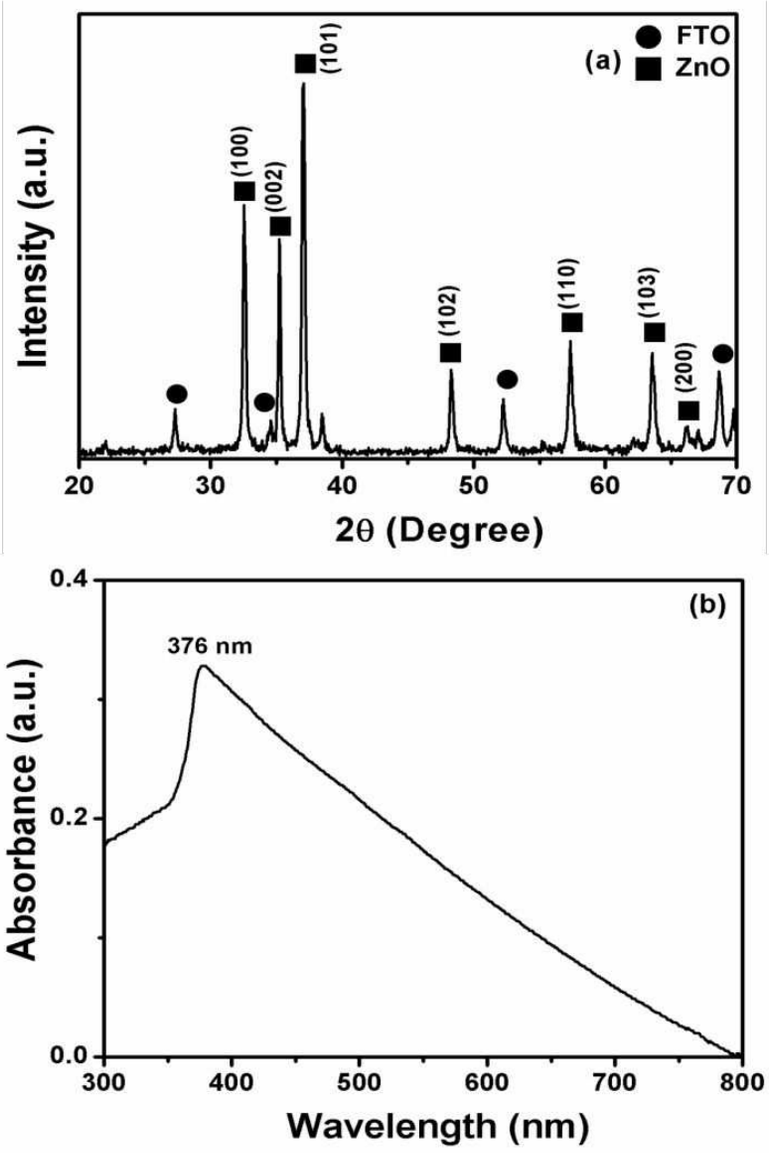

Figure 20. XRD patterns (a) and UV-Vis spectra (b) of nanospikes decorated ZnO sheets. Reprinted with permission from [Ameen S., 2012], Chem. Eng. J. 195 (2012) 307©2012, Elsevier Ltd.

The survey XPS spectrum (Fig. 21 (a)) of grown nanospikes decorated ZnO sheets shows the three strong binding energies of Zn $2p_{3/2}$, Zn $2p_{1/2}$ and O 1s along with small C 1s binding energy. The other binding energies peaks are not detected, indicating the presence of Zn and O without other impurities. However, the C1s binding energy at ~ 284.6 eV is usually used as calibration for other binding energies in the spectrum to avoid the specimen charging [103]. The Zn 2p spectrum of the doublet peaks with the binding energies of ~1021 eV and ~1045 eV are shown Fig 21(b), corresponding to Zn $2p_{3/2}$ and Zn $2p_{1/2}$ in better symmetry, respectively. These binding energies and the difference between two binding energies to ~24 eV are attributed to the typical lattice Zinc in ZnO [104]. The peak at ~1021 eV is associated with the Zn^{2+} in ZnO wurzite structure [105]. Moreover, Zn 2p binding energy and the binding energy difference values confirm that Zn atoms are in +2 oxidation state in ZnO. The deconvolution of O 1s XPS spectrum (Fig. 21(c)) exhibits the main peak at ~528.3 eV along with three resolved peaks at ~529.2 eV, ~530.1 eV and ~531.1 eV. The higher and lower binding energy component at ~528.3 eV and ~529.2 eV are attributed to O_2^- ions on the wurtzite structure of the hexagonal Zn^{2+} ions [106]. Every O_2^- ions are surrounded by Zn atoms with the full appreciation of nearest neighbor O_2^- ions. The other binding energies at ~530.1 eV and ~531.1 eV are ascribed to few oxygen deficiency or oxygen vacancies within the ZnO materials. Therefore, highest binding energy of Zn 2p and O 1s spectra are associated with Zn^{2+} and O_2^- ions which form Zn-O bonds in ZnO crystals.

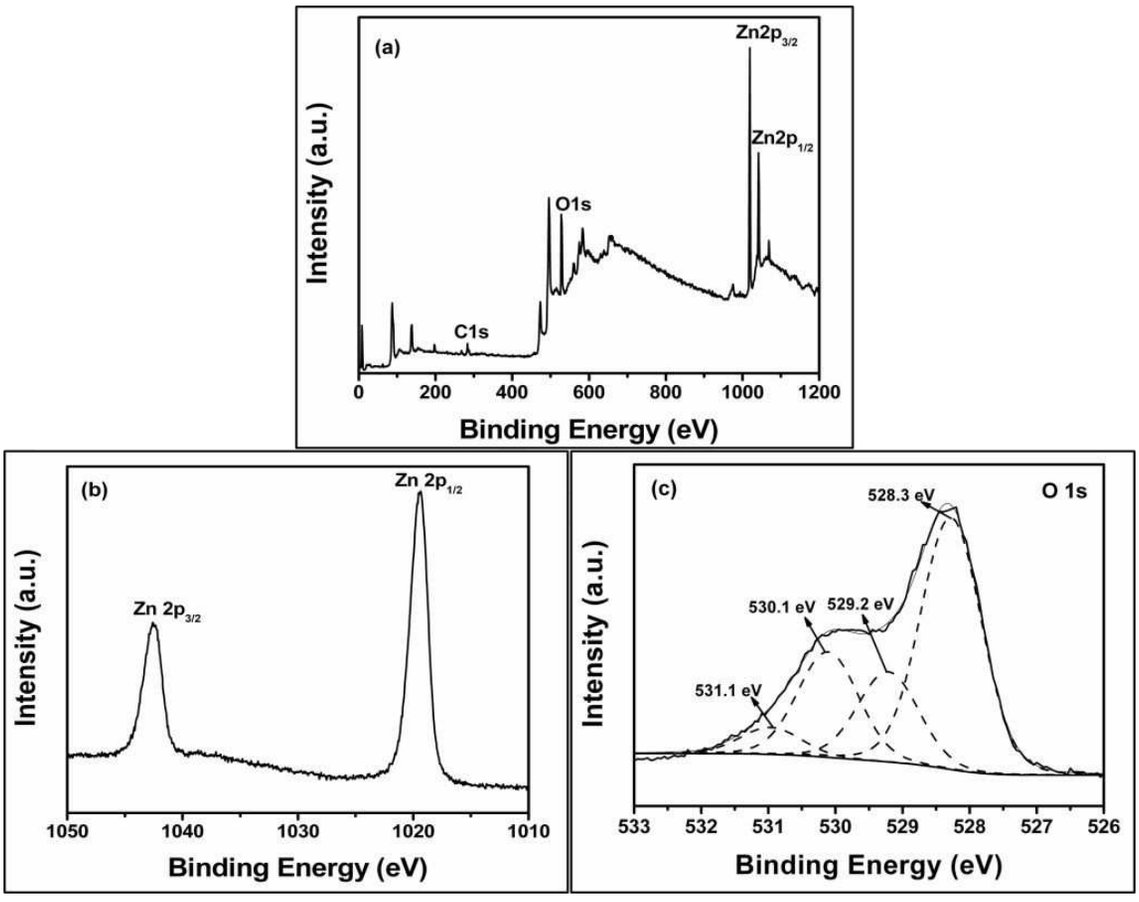

Figure 21. Survey (a), Zn 2p (b) and O 1s (c) XPS spectra of nanospikes decorated ZnO sheets. Reprinted with permission from [Ameen S., 2012], Chem. Eng. J. 195 (2012) 307 ©2012, Elsevier Ltd.

http://dx.doi.org/10.5772/51432

The J-V curve (Fig. 22(a)) of DSSC fabricated with nanospikes decorated ZnO sheets photoanodes is demonstrated under the light intensity of 100 mW/cm^2 (1.5 AM). The fabricated DSSC with the photoanode of nanospikes decorated ZnO sheets has achieved the overall conversion efficiency of ~2.51% with the reasonably high J_{SC} of ~6.07 mA/cm^2, V_{OC} of ~0.68 V and FF of ~0.60. The relatively high J_{SC} is associated to high dye absorption through nanospikes decorated ZnO sheets morphology, resulting from the high amount of dye absorption (2.05 x10^{-7} mol/cm^2) which is calculated by area integration of the maximum absorbance in the UV-Vis spectrum of desorbed dye from the photoanode (as shown in inset of Fig. 22(a)). The unique morphology of the prepared nanospikes decorated ZnO sheets might pronounce the charge collection and transfer properties of electrode due to the presence of standing spikes on the ZnO sheets [107]. The improved V_{OC} and FF of DSSC might attribute to the reduced charge recombination and the series resistance by the photoanode of nanospikes decorated ZnO sheets. As compared to the reported DSSCs based on ZnO nanostructures photoanodes, the nanospikes decorated ZnO sheets photoanode based DSSC shows the significantly higher conversion efficiency and J_{SC} [108]. It has been estimated that the conversion efficiency and J_{SC} are enhanced by ~40% and ~25% as compared to reported values. In this case, the sheets morphology of ZnO display highly uniform and the standing nanospikes might considerably

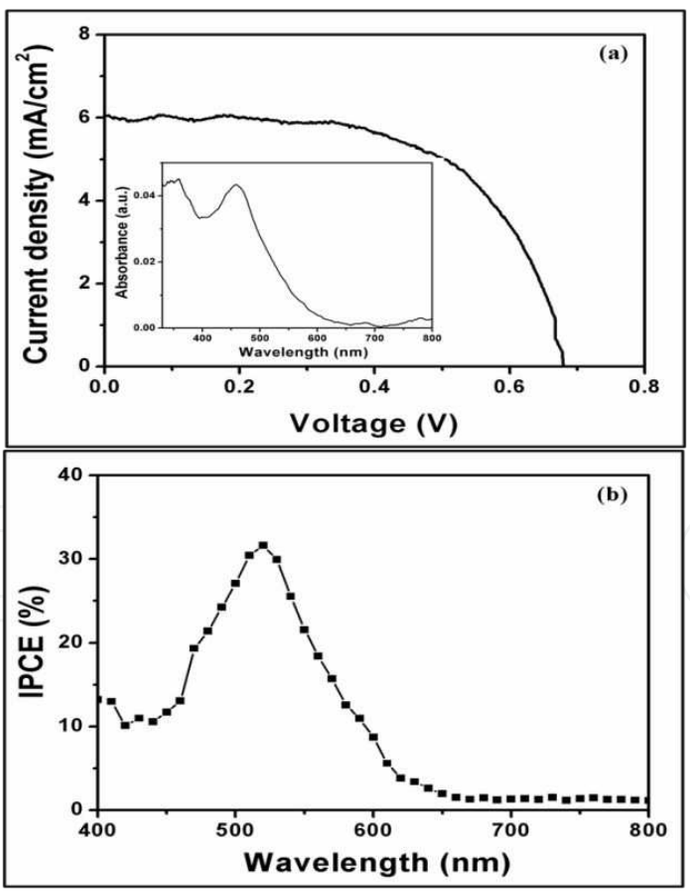

Figure 22. J-V curve (a) and IPCE (b) curve of the DSSC fabricated with nanospikes decorated ZnO sheets photoanode. Inset (a) shows the UV-Vis spectrum of desorbed dye from the nanospikes decorated ZnO sheets photoanode. Reprinted with permission from [Ameen S., 2012], Chem. Eng. J. 195 (2012) 307 ©2012, Elsevier Ltd.

facilitates the electrons transfer at the interface of the conduction and the electrolyte layer. The fabricated DSSC with photoanode of nanospikes decorated ZnO sheets attains the moderate IPCE of ~31.8%, as shown in Fig. 22 (b), which is probably originated from the larger amount of dye-loading through large surface area of sheet and the standing spikes of photoanode. Moreover, the presence of nanospikes on ZnO sheets might efficiently enhance the electron transport and reduces the recombination rate to high IPCE and J_{SC} value 109].

7. Doping of ZnO for improved electrical and photovoltaic properties

One of the modifications is still in the developing stage called doping of ZnO nanomaterials by metals like F, Cu, Ag, Ga, Al, In, Sn and Sb which usually tailors the chemical, conductive and the electrical properties of ZnO nanomaterials [110]. The metal doping is an effective procedure to modify the grain size, orientation and the conductivity and could greatly influence the crystalline, optical and the electrical properties of the ZnO nanostructures. Among various metal doping, Sn-ion is recently known as promising dopant to ZnO nanomaterials for enhancing the electrical and optical properties [111]. Tsay et al. [112] prepared the Sn doped ZnO thin films coated glass substrates and investigated the effects of Sn doping on the crystallinity, microstructures and the optical properties of ZnO thin film. Several reports are available on the preparation of the Sn doped ZnO thin films and the effects of Sn doping on grain size, vibrational structure, optical and the structural properties of ZnO thin film substrates [113]. Ameen et al recently reported the doping of ZnO nanostructures with Sn ion by simple hydrothermal process for the fabrication of DSSC [114].

7.1. Sn doped ZnO nanostructures for solar cell performance

The synthesized ZnO and Sn-ZnO nanostructures are morphologically characterized by the FESEM images, as shown in Fig. 23. The ZnO nanostructure shows the irregular, non-uniform and highly aggregated nanoparticles with the average size of range ~150–200 nm. After Sn-ion doping, the ZnO nanostructures have dramatically arranged into the spindle shaped morphology and each Sn-ZnO spindle comprises of small aggregated nanoparticles with average size of 350 ±50 nm.

Fig. 24 (a, b) shows the high resolution TEM images of Sn-ZnO nanostructures which are completely consistent with FESEM observations. The aggregated ZnO nanoparticles arranged spindle shaped morphology is observed with some black spots or particles, clearly indicating the presence of the Sn-ions. The HR-TEM image of Sn-ZnO displays dark spots on the fringes which are expressed by the circles in Fig. 24(c). The morphological changes in Sn-ZnO nanostructures might due to the substantive influence of Sn-ion into ZnO nanostructures. The EDS spectrum (Fig. 24 (d)) obtains two high intense peaks (Zn & O) and single small peak (C) along with Sn peaks, again confirming the Sn-ion doping into the ZnO nanostructures.

From the UV-DRS spectra of ZnO and Sn-ZnO nanostructures (Fig. 25), the broad intense absorption edge from ~400 nm to lower wavelengths region is assigned to the charge-transfer process from the valence band to conduction band of ZnO [115]. After Sn-ion doping, the

http://dx.doi.org/10.5772/51432

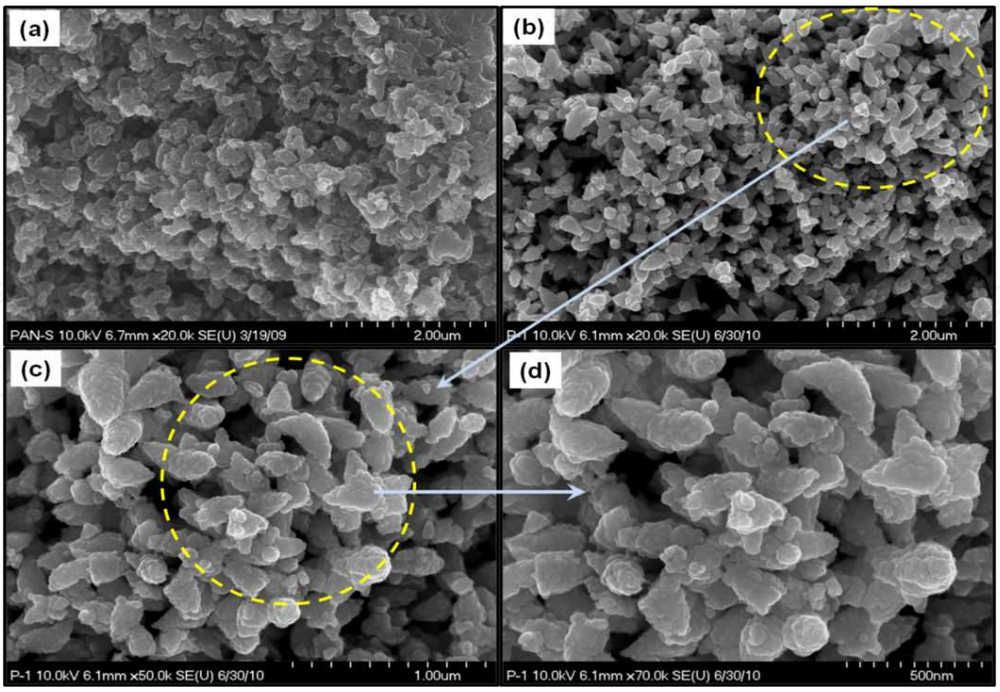

Figure 23. FESEM images of ZnO (a) and Sn-ZnO (b) nanostructures at low resolution, and FESEM images of Sn-ZnO nanostructures at high resolution (c and d). Reprinted with permission from [Ameen S., 2012], Chem. Eng. J. 187 (2012) 351 ©2012, Elsevier Ltd.

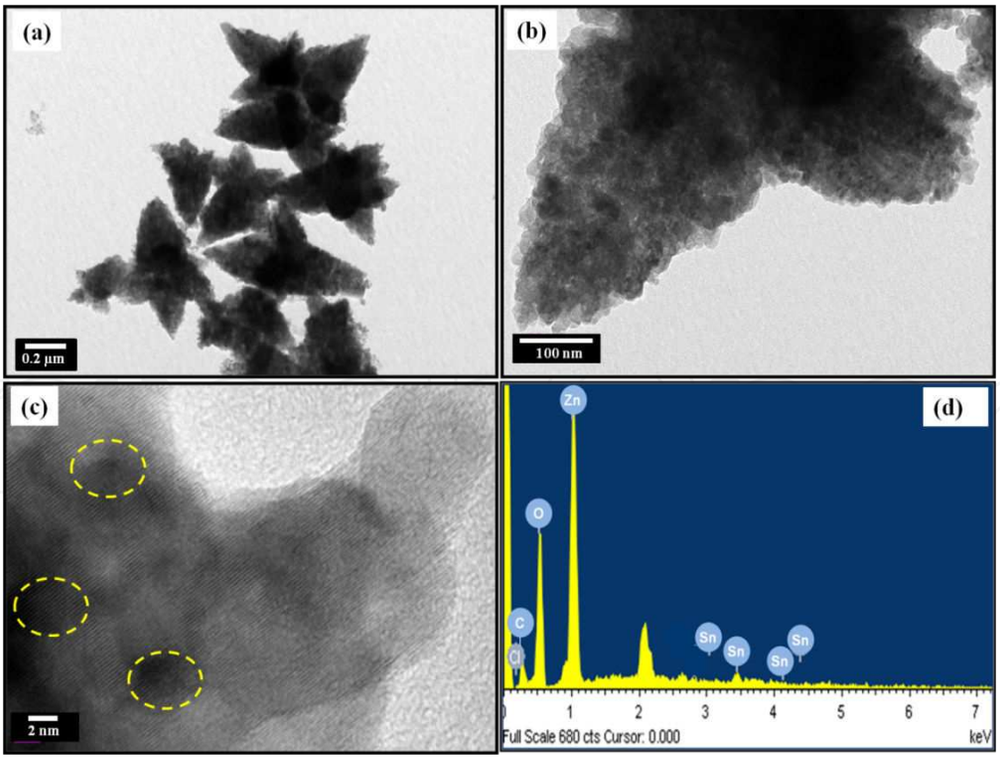

Figure 24. TEM images of Sn-ZnO nanostructures at low resolution (a and b), HRTEM image (c), and EDS spectrum of Sn-ZnO nanostructures (d). Reprinted with permission from [Ameen S., 2012], Chem. Eng. J. 187 (2012) 351 ©2012, Elsevier Ltd.

absorption wavelength of ZnO has significantly shifted from ~389 nm to ~406 nm and its band gap has changed from ~3.18 eV to ~3.05 eV. It has arisen due to the presence of interstitially embedded Sn-ion into ZnO nanomaterials. This small variation in band gaps again confirms the Sn-ion doping into ZnO nanomaterials.

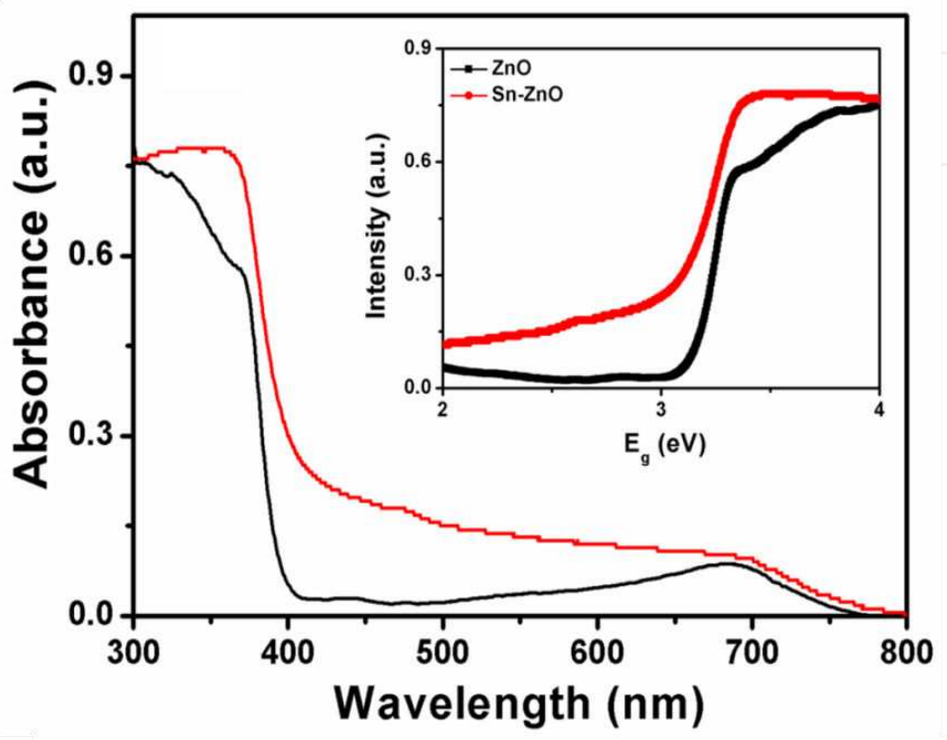

Figure 25. UV-DRS spectra of ZnO and Sn-ZnO nanostructures. Reprinted with permission from [Ameen S., 2012], Chem. Eng. J. 187 (2012) 351 ©2012, Elsevier Ltd.

The XPS survey (Fig. 26 (a)) spectrum displays all Zn 2p, O 1s and Sn 3d binding energy peaks with very small C 1s binding energy. Sn-ZnO nanomaterials show the doublet binding energies at ~1022.1 eV and ~1046.1 eV in Zn 2p XPS spectra (Fig. 26 (b)) which correspond to Zn $2p_{3/2}$ and Zn $2p_{1/2}$ respectively. The energy difference between doublet binding energies is calculated to ~24 eV, which is in excellent agreement with the standard value of ~22.97 eV. The deconvoluted O 1s XPS presents the four binding energies peaks at ~533.6 eV, ~532.4 eV, ~530.8 eV and ~529.1 eV, as shown in Fig. 26 (c). The highest binding energy at ~533.6 eV is originated from the oxygen atoms chemisorbed at the surface of synthesized materials [116]. The binding energy at ~532.4 e V is ascribed to O_2^- ions (surface hydroxyl (OH) group) on the synthesized Sn-ZnO (in the oxygen deficient region) and the lowest binding energy at ~529.1 eV is attributed to O_2^- ions in the Zn-O structures The binding energy at ~530.8 eV is attributed to oxidized metal ions in the synthesized Sn-ZnO such as, O-Sn and O-Zn in the ZnO lattice. Sn 3d spectra (Fig. 26 (d)) presents the doublet binding energies at ~487.2 eV and ~496.7 eV, correspond to Sn $3d_{5/2}$ and Sn $3d_{3/2}$ respectively. The appearance of these peaks indicates the incorporation of Sn dopant in the form of O-Sn in the ZnO lattice [117], as deduced by O 1s XPS results. Moreover, the energy gap of ~9.5 eV is

http://dx.doi.org/10.5772/51432

observed between these two peaks which resembles to the reported value [118]. It is observed that since no diffraction peaks corresponding to the SnO and SnO_2 are observed in the XRD spectra therefore, the O-Sn bonding could be considered as the substitutional doping of Sn-ions into the ZnO lattice.

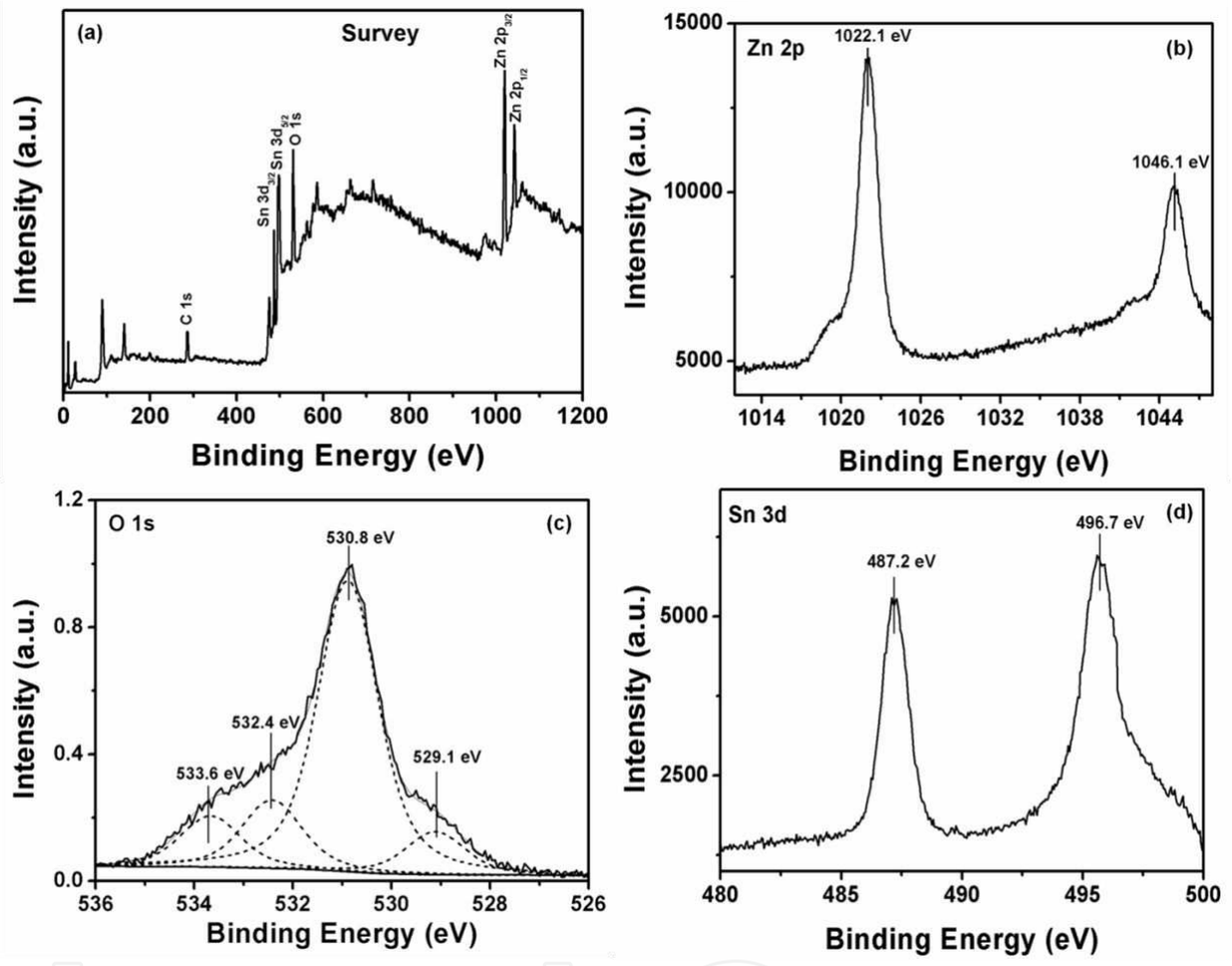

Figure 26. Survey (a), Zn 2p (b), O 1s (c), and Sn 3d (d) XPS spectra of Sn-ZnO nanostructures. Reprinted with permission from [Ameen S., 2012], Chem. Eng. J. 187 (2012) 351. ©2012, Elsevier Ltd.

DSSC fabricated (Fig. 27) with Sn-ZnO photoanode depicts reasonably high solar-to -electricity conversion efficiency of ~1.82% with J_{SC} of 5.1 mA/cm^2, V_{OC} of 0.786 V and FF of 0.45. While, DSSC with ZnO photoanode shows relatively low conversion efficiency of ~1.49% with J_{SC} of ~4.05 mA/cm^2, V_{OC} (~0.761 V) and FF of ~0.48. Noticeably, the conversion efficiency and J_{SC} are considerably enhanced by ~20% and ~21% respectively after Sn-ion doping into ZnO nanostructures. Moreover, it could be explained that Sn-ZnO nanostructures might due to the increase of high charge collection and the transfer of electrons at the interface of Sn-ZnO and the electrolyte layer. The dopants like Sn, is known to enhance the electrons transport capacity and electron mobility of ZnO nanomaterials [119]. Moreover, the Sn-ion doping into ZnO nanostructures might increase the specific surface area by lowering the particle size and

arranging into spindle shaped morphology, which might contribute to high dye absorption. The increased photocurrent density and the improved photovoltaic performance might also result from high dye absorption and the improved electron transport by Sn-ZnO nanostructures, leading the enhancement in light harvesting efficiency and photo-excited electron transportation under sun light. Therefore, the arrangement of ZnO nanoparticles into Sn-ZnO spindle shaped, and good optical properties of Sn-ZnO are crucial to improve the conversion efficiency and the photocurrent density of the fabricated DSSCs.

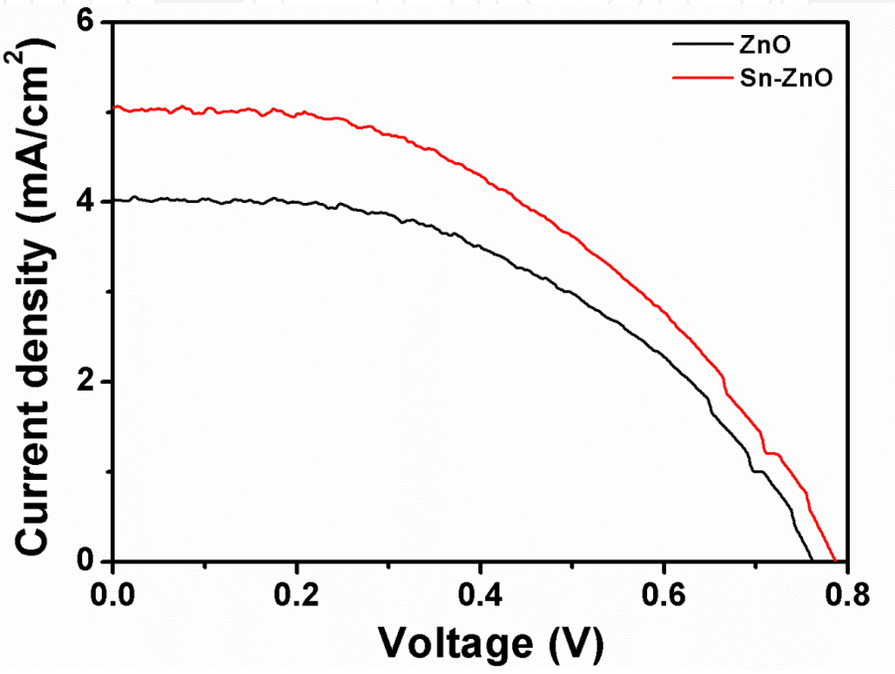

Figure 27. J-V curve of the DSSC fabricated with ZnO and Sn-ZnO nanostructures based photoanodes. Reprinted with permission from [Ameen S., 2012], Chem. Eng. J. 187 (2012) 351. ©2012, Elsevier Ltd.

7.2. Ga doped ZnO nanostructures with improved electrical properties

ZnO nanomaterials along with conjugated polymers like PANI, PPy and poly (3-alkylthiophene) comports the high quality organic/inorganic Schottky diodes [120]. Recently, ZnO-PANI films sandwiched between indium tin oxide (ITO) and a Pt electrode have displayed the linear I-V behavior [121]. The effects of Ga ion doping on ZnO NPs have been studied by Ameen et al on the basis of optical and electrical properties of the fabricated heterostructure devices [122]. The morphology of the synthesized ZnO and Ga-ZnO NPs were studied by FESEM and TEM analysis, as shown in Fig. 28 (a-d). The synthesized ZnO NPs obtain an average diameter of ~20–25 nm. After Ga ion doping, the average diameter increases to ~30–35 nm by the agglomeration of NPs due to entrapping and the substantive influence of Ga ion with ZnO NPs.

The optical properties of ZnO and Ga-doped ZnO NPs were studied by the UV-Vis spectra, as shown in Fig. 29 (a, b). ZnO and Ga-doped ZnO NPs present the absorption in the UV region with strong absorption peak at ~370 nm and ~378 nm respectively, corresponding to the

http://dx.doi.org/10.5772/51432

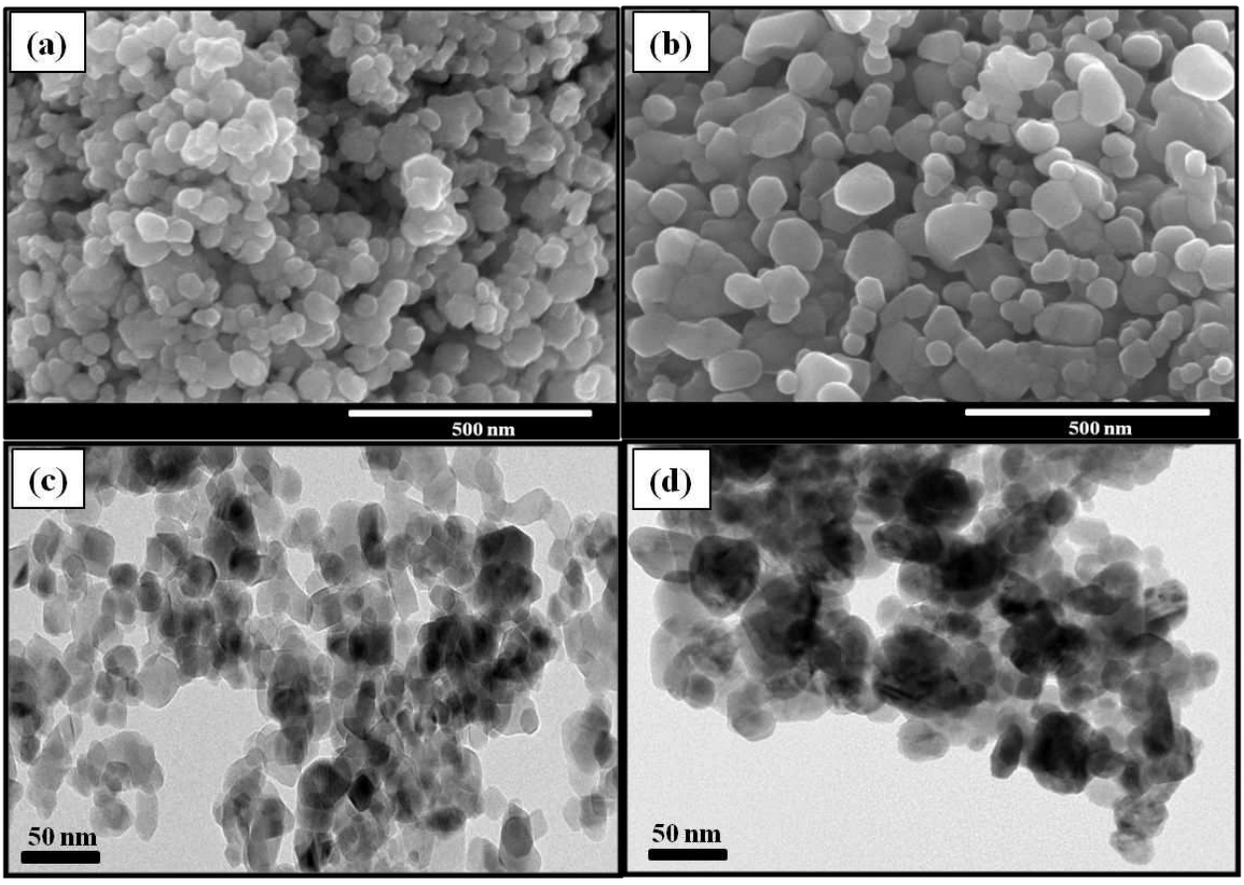

Figure 28. FESEM (a, b) and TEM (c, d) images of ZnO NPs and Ga-ZnO NPs. Reprinted with permission from [Ameen S., 2011], Microchim. Acta 172 (2011) 471. © 2012, Springerlink Ltd.

characteristic band of wurtzite hexagonal ZnO nanomaterials [123]. A considerable red shift from ~370 nm to ~378 nm after Ga ion doping is seen in the absorption peak of Ga-ZnO NPs and results that the band gap of ZnO NPs has changed from ~3.4 eV to ~3.26 eV due to the presence of interstitially embedded Ga ion on the surface of ZnO NPs. Thus, the small variation in band gaps again confirms the Ga doping on the surface of ZnO NPs.

Fig. 30 shows the XPS of PANI/Ga-ZnO thin film electrodes. The Carbon (C 1s), oxygen (O 1s), nitrogen (N 1s) and Zinc (Zn 2p) peaks at ~284.4 eV, ~529.8 eV, ~400.9 eV and ~1019.4/1042.5 eV are taken to investigate the interaction between PANI and Ga-ZnO NPs. The deconvoluted C 1s peak at ~284.4 eV presents four resolved peaks at ~289.1, ~286.8, ~285.7 eV and ~284.9 eV (Fig. 30 (a)) and are ascribed to C = O/C–O bond, C–N^+/C = N^+ bond, neutral C–C/C–H bond of PANI backbone and C of the benzonoid ring showing a combination of protonation of imine and amine sites via shake-up processes [124]. Figure 30(b) shows the four O 1s XPS resolved peaks of PANI/Ga-ZnO thin film. The main peak at ~529.8 eV confirms the nature of oxygen atom originated from metal oxide [125] i.e. the oxide of ZnO NPs. Zn 2p XPS of PANI/Ga-ZnO thin film typically exhibits the doublet peaks at ~1019.4 eV/1042.5 eV (Fig. 30 d), suggests that Zn atoms are linked with oxide bond in Ga doped ZnO NPs. Moreover, Fig. 30(e) shows the Ga 2p peak at ~1116.2 eV which confirms the doping of ZnO with the Ga^{+2} oxidation state [126].

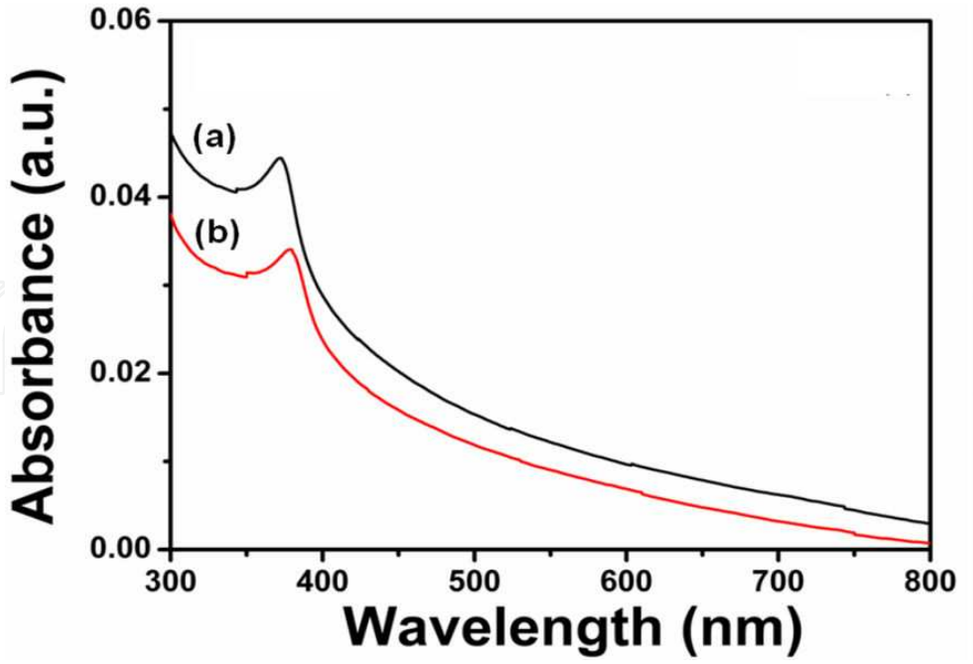

Figure 29. UV-Vis spectra of ZnO (a) and Ga-ZnO NPs (b). Reprinted with permission from [Ameen S., 2011], Microchim Acta 172 (2011) 471© 2012, Springerlink Ltd

N 1s XPS spectrum of PANI/Ga-ZnO thin film (Fig. 30(c)) exhibits the bonding between imine group of PANI and Ga-ZnO. The centered peak at ~400.9 eV ascribes quinoid di-imine nitrogen of PANI [127]. The main peak at ~400.9 eV is resolved into four hide peaks at ~400.5, ~401.3, ~401.9 and ~402.8 eV which correspond to benzenoid di-amine nitrogen, quinoid di-imine nitrogen, positively charged nitrogen ($-N^+$) and the protonated imine ($=N^+$) respectively. It is known that the protonation of PANI produces electronic defects such as polarons or bipolarons which might form by the addition of protons to the neutral polymer chain. In this case, positively shifted binding energy at ~401.9 and ~402.8 eV might exhibit the participation of protonated N atom for the bond formation between PANI and Ga-ZnO. These two charged nitrogen species ($-N^+$ and $=N^+$) are originated from these defect states [128] and are observed in N 1s results of PANI/Ga-ZnO thin film. In conclusion, the PANI and Ga-ZnO are interacted to each other by the formation of partial hydrogen bonding between two charged nitrogen species ($-N^+$ and $=N^+$) of PANI and surface hydroxyl of Ga-ZnO.

The I-V characteristics of Pt/PANI/ZnO and Pt/PANI/Ga-ZnO heterostructure devices are obtained at 298 K with applied voltage from −1 V to +1 V, shown in Fig. 31. Both the devices display non-linear and rectifying behavior of I–V curves due to the existence of Schottky barrier via a Schottky contact at the interfaces of Pt layer and PANI-ZnO thin film layer. Pt/PANI/ZnO device shows almost Ohmic or very weak rectifying behavior (Fig. 31(a)) that attains very low turn-on voltage (~0.0005 V) with least current (~0.002 mA). Similarly, in forward bias, a breakdown voltage (~0.05 V) and high leakage current (~0.015 mA) indicate poor I-V characteristics of Pt/PANI/ZnO device. Whereas, Pt/PANI/Ga-ZnO device (Fig. 31 (b)) presents

http://dx.doi.org/10.5772/51432

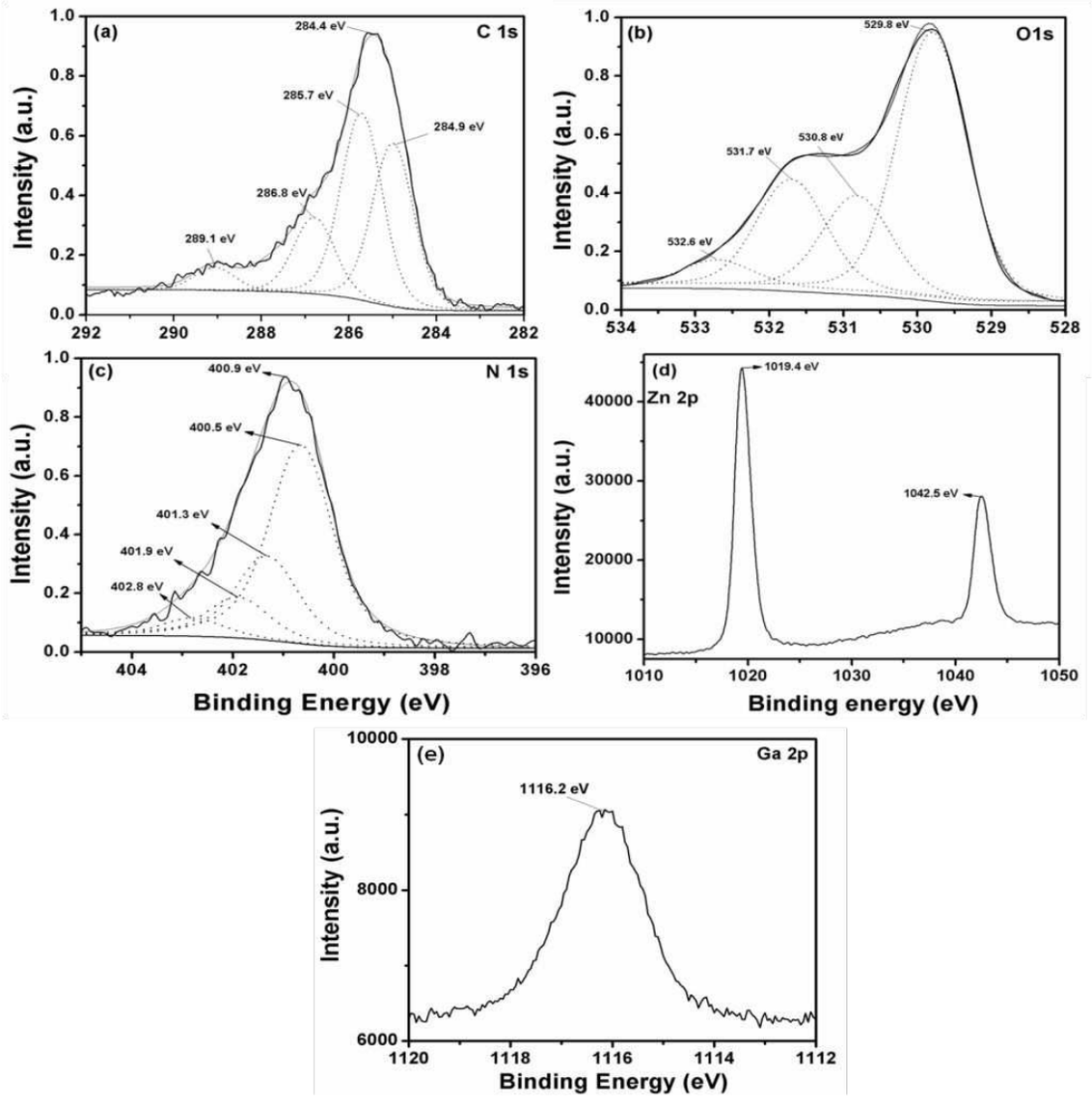

Figure 30. (a) C 1 s, (b) O 1 s, (c) N 1 s, (d) Zn 2p and (e) Ga 2p XPS spectra of PANI/Ga-ZnO thin film electrode. Reprinted with permission from [Ameen S., 2011], Microchim. Acta 172 (2011) 471©2012, Springerlink Ltd.

rectifying behavior of lower turn on voltage (~0.4 V) with least current (~0.09 mA) and breakdown voltage (~0.56 V) with high leakage current (~0.5 mA). The I-V properties of Pt/PANI/Ga-ZnO device are considerably better than the data reported elsewhere on PANI/ZnO and PANI based heterostructure devices [129]. Herein, the Ga ion doping to ZnO NPs might generate high density of minority charge carriers and the efficient charge movement at the junction of PANI and Ga-ZnO interfaces, resulting in the high leakage current with moderate turn on and breakdown voltage [130]. Additionally, the improved I-V properties might result from the molecular geometry of PANI chains and the increased electronic conduction by Ga ions in ZnO NPs which likely generate the hopping effect.

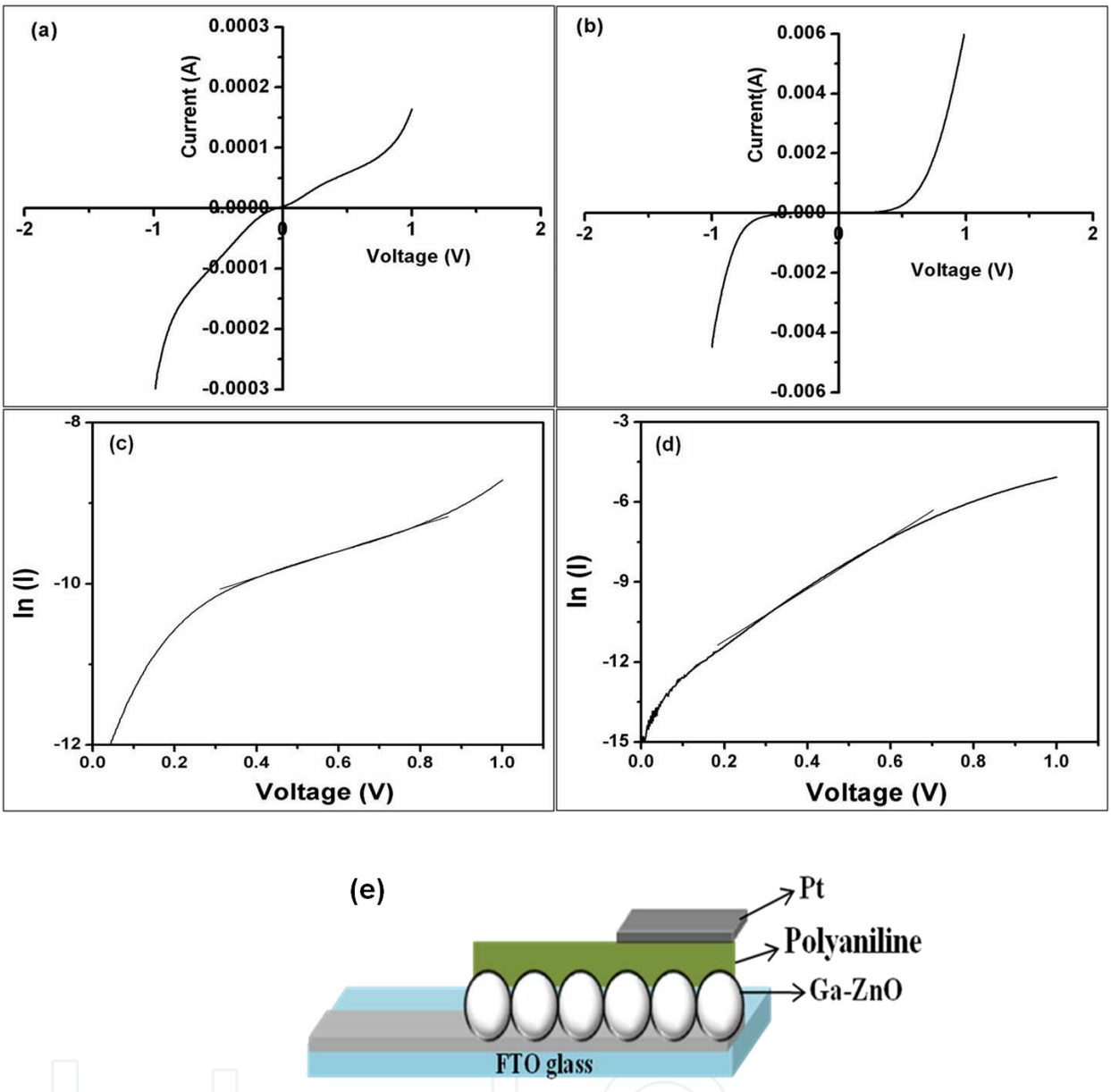

Figure 31. I-V characteristics of (a) Pt/PANI/ZnO (b) Pt/PANI/Ga- ZnO heterostructure device. ln(I) versus (V) plots of (c) Pt/PANI/ZnO and (d) Pt/PANI/Ga-ZnO heterostructure devices. (e) the schematic of Pt/PANI/Ga-ZnO heterostructure device. Reprinted with permission from [Ameen S., 2011], Microchim. Acta 172 (2011) 471©2012, Springerlink Ltd.

8. Metal oxides as nanofillers in polymer electrolytes

The inorganic semiconductor especially metal oxides nanomaterials as nanofillers are conceived to improve the mechanical, thermal, interfacial, and ionic conductivity properties of the polymer electrolytes, which could effectively utilize for high performance solid-state DSSCs. In general, the introduction of inorganic NPs in the polymer alters the conduction mechanisms,

which assigns to the ions conduction. In 1998, Croce et al. [131] studied the enhancement of the ionic conductivity of polymer electrolytes by the addition of TiO_2 and other NPs. Later, a ternary component polymer-gel electrolyte with TiO_2 NPs was prepared by Kang et al and explicated that these NPs led to a light-scattering effect [132]. The fabricated DSSC with the ternary component polymer electrolyte showed a high overall conversion efficiency of ~7.2% under 100 mW/cm^2. Falaras et al [133] developed the polymer composite electrolyte by the addition of commercial TiO_2 nanoparticles (NPs, P25, Degussa) consisted of polyethylene oxide (PEO), LiI, and I_2. The addition of TiO_2 NPs considerably prevented the re-crystallization and decreased the degree of crystallinity of PEO due to their large surface area. The differential scanning calorimetry (DSC) studies revealed that the introduction of TiO_2 NPs caused a significant increase in the glass transition temperature of PEO, which indicated the incorporation of the polymer to the inorganic oxide fillers. The fabricated DSSCs with TiO_2-PEO nanocomposite electrolyte achieved a reasonably high overall conversion efficiency of ~4.2% with a J_{SC} of ~7.2 mA/cm^2, V_{OC} ~0.664 V, and FF ~0.58 at ~65.6 mW/cm^2 [134]. Additionally, other research groups have also used TiO_2 NPs as nanofillers and explained the effects of nanofillers on different polymer electrolytes. Recently, Akhtar et al [135] reported a composite electrolyte of polyethylene glycol methyl ether (PEGME) and TiO_2 NPs and demonstrated the heat treatment effects on the properties of PEGME-TiO_2 composite electrolyte. It was found that the heat treatment was an essential step to improve morphology, amorphicity, and ionic conductivity of PEGME-TiO_2 composite electrolytes. From AFM images (Fig. 32), TiO_2 particles with ~20-30 nm size are well distributed on the PEGME matrix in the case of PEGME-TiO_2 composite film (Fig. 32(a). However, TiO_2 particles are aggregated and become a bigger size (40-60 nm) on the polymer matrix in PEGME-TiO_2/80^{o}C (Fig. 32 (b)). From the film roughness analysis (Fig. 32 (c, d)), it is observed that the surface roughness of the PEGME-TiO_2/80^{o}C and PEGME-TiO_2 composites are estimated to be about ~23.1 nm and ~18.5 nm for the root mean square roughness (R_{rms}), and ~12 nm and 8~.8 nm for the average surface roughness (R_a), respectively. Generally, it has been well known that the low surface roughness of the polymer composite film is ascribed to the high-crystallized surface of thr composite materials. Therefore, the crystallinity of PEGME-TiO_2/80^{o}C might lower than PEGME-TiO_2 because the former exhibits the higher R_{rms} and R_a value than later composite film. Consistently, the 3D AFM images (Fig. 32 (d)) of PEGME-TiO_2/80^{o}C exhibit a highly rough surface morphology with non-uniformly distributed TiO_2 particles into the PEGME matrix, while a highly uniform and less rough surface is observed in PEGME-TiO_2 composite film before heating (Fig. 32 (c)). This rough morphology of PEGME-TiO_2/80^{o}C might create free spaces and voids in which the I^-/I_3^- ions could easily migrate, which suggest the PEGME-TiO_2/80^{o}C as excellent electrolyte materials. With the improved morphology of PEGME-TiO_2 composite, the electrolyte shows the high ionic conductivity of ~1.9 mS/cm as compared to the PEGME acid (1.2 mS/cm) and PEGME-TiO_2 (0.92 mS/cm) which results from the enhanced morphological properties in terms of high roughness and amorphicity after heating of PEGME-TiO_2. The Raman spectra (Fig. 33) of the PEGME-acid, PEGME-TiO_2, and PEGME-TiO_2/80^{o}C composite electrolytes exhibit a significant peak at the range of 110-115 cm^{-1}, which is ascribed to the symmetric stretch of I_3^- species in redox electrolytes [136]. The heat treatment on PEGME-TiO_2 drastically increased the strong Raman peak, indicating a significant increase in the amount of I_3^- species in redox

electrolytes. It might attribute to the increased bond strength between PEGME and TiO_2 and high roughness of the composite materials, which might help to absorb a large amount of the iodide couple as compared to PEGME-acid and PEGME-TiO_2 composite electrolytes. The increased intensity of peak suggests that a large amount of I_3^- species is formed in the PEGME-TiO_2/80°C composite electrolyte upon heat treatment. In general, the diffusional I^-/I_3^- ions migration in the redox electrolyte is responsible for the ionic conductivity of electrolyte, which causes electron exchange between ions by electronic conduction process [137]. The electronic conduction in redox electrolyte depends on the formation of I_3^- ions. Raman results show the proportional relation between the ionic conductivity and concentration of I_3^- species of the composite electrolytes, which is directly related to relative intensity of Raman peak. The enhanced ionic conductivity of PEGME-TiO_2/80°C composite electrolyte might associate with the formation of high I_3^- species in redox electrolyte. However, low ionic conductivity in PEGME-acid and PEGME-TiO_2 composite electrolyte results from the low relative intensity of the Raman peak and less formation of I_3^- species in redox electrolyte. Therefore, a heat treatment step plays an essential role to prepare the improved composite electrolyte with enhanced ionic conductivity. DSSC fabricated with PEGME-TiO_2/80°C composite electrolyte shows the maximum overall conversion efficiency of ~3.1% with a J_{SC} of ~8.9 mA/cm^2, V_{OC} of ~0.625 volt, and FF of ~56.2%. The conversion efficiency and J_{SC} of DSSCs with PEGME-TiO_2/80°C composite electrolytes is higher than those of fabricated with PEGME-acid (~1.3%) and PEGME-TiO_2 (~2.4%) electrolytes. This could be expected from the enhanced ionic conductivity and enlargement of the amorphous phase of the polymer upon heat treatment. The heat treatment on PEGME-TiO_2 composites enhances the ionic conductivity and cross-linking properties of composite electrolyte, which are essential factors to achieve the high current density and high PV performance. Furthermore, Akhtar et al [138] investigated the effect of titania nanotubes (NTs) as nanofillers on the properties of PEG-based electrolytes and fabricated solid-state DSSCs. PEG-TiNT electrolytes with 10% of TiNTs exhibit the high penetration and complete filling into the pores of the TiO_2 film, as shown in Fig. 34. The XPS studies (Fig. 35) were carried out to elucidate the strong interaction between PEG and TiNTs. PEG-TiNT10 electrolyte shows the highest interaction between the titanium atoms of the NTs and the polymer network as compared to those of other PEG-TiNTs electrolytes. This results to the decrease in the crystallinity degree of the polymer after introduction of the NTs which achieves the highest ionic conductivity of ~2.4×10^{-3} S/cm. DSSC fabricated with PEG-TiNT composite electrolyte (Fig. 36) exhibits the maximum overall conversion efficiency of ~4.4% with J_{SC} of ~9.4 mA/cm^2, V_{OC} of ~0.73 V, and FF of ~0.65 under 100 mW/cm^2 irradiation. No significant decrease of the conversion efficiency for 30 days was observed in DSSCs fabricated with PEG-TiNT10 (inset of Fig. 36), indicating the high stability of the composite electrolytes. The lower current density in PEG-TiNT20 is due to its lower ion conductivity, lower penetration, and weak interaction between PEG to TiNTs. It is proved that the better penetration into the pores of the TiO_2 layer was obtained at a ratio of TiNT and PEG in the composite electrolyte (PEG-TiNT10). Thus, due to the better interfacial contact between the electrolyte and TiO_2 layer, high ion conductivity is obtained, which enhances the photocurrent density. Moreover, the PEG-TiNT composite electrolytes might facilitate the movement of electrons in the redox (I^-/I_3^-) couple due to the fast electron transfer characteristics of NTs with less grain-boundary,

http://dx.doi.org/10.5772/51432

in comparison to NPs. The other metal oxide nanomaterials, such as ZnO, SiO_2 and Al_2O_3, have been introduced as nanofillers to different polymer electrolytes [139]. Caruso et al. prepared the polymer composite electrolyte with the composition of PEO-poly (vinylidenefluoride) (PVDF) and SiO_2 NPs and applied as a solid electrolyte for solid-state DSSCs [140]. These kinds of solid state electrolytes presented high viscosity to the solid state electrolyte with TiO_2-based polymer composites. They used a vacuum technique for introducing the composite polymer electrolytes into the dye-sensitized TiO_2 electrode which showed that the vacuum method exhibited a better performance than those prepared via the conventional drop casting method. This approach improved the fulfilling of the photoelectrode with a solid electrolyte by vacuum technique, but the optimization of the electrolyte composition is still an important issue. In this regards, Xia et al utilized ZnO NPs as nanofillers for preparing the composite polymeric electrolyte of poly (ethylene glycol methyl ether) (PEGME) [141]. The PEGME was first grafted onto the surface of ZnO NPs through covalent bond formation by a chemical process. The solid composite electrolyte consisted of KI and I_2 dissolved in PEGME and ~24 wt% of the polymer-grafted ZnO NPs. The obtained prepared electrolyte showed that the ionic conductivity increased as the salt concentration increased and reached a maximum value of ~3.3×10^{-4} S/cm and then decreased, acting as a classical polymer electrolyte system. DSSC fabricated with polymer-grafted NPs electrolyte presented the lower conversion efficiency of ~3.1% compared to that of DSSC with a liquid electrolyte (~4.0%). After the addition of polymer-grafted ZnO NPs in liquid electrolyte, the V_{OC} of DSSC increased by ~0.13 V while the J_{SC} decreased, this was probably due to the high viscosity of the gel electrolyte. Another report addressed the new polymer electrolyte system of Al_2O_3 NPs with different sizes and a PVDF derivative and polyacrylonitrile in an ionic-liquid-based electrolyte [142]. The diffusion coefficient of I_3^- ions altered by the addition Al_2O_3 NPs. The variation in sizes of Al_2O_3 NPs greatly influenced the charge transfer rate at the electrolyte and semiconducting layer interfaces. In this report, the imidazolium cations might adsorb on the NP surface, which might help in the charge transfer at counter and anions I^-/I_3^- gather around them. Some researchers have recently used clay-like NPs as nanofillers in the polymer electrolytes and applied to the DSSCs [143]. Nogueira et al. [144] examined the incorporation of a montmorillonite (MMT) derivative to a polymer electrolyte based on a poly-(ethylene oxide) copolymer, the plasticizer GBL, and Li I/I_2. The improved ionic conductivity of the composite electrolyte attributed to the large number of charge carriers introduced into the complex after the addition of the clay. The addition of 5 wt % MMT promoted the increase in the mechanical stability of the nanocomposite polymer electrolyte film, resulted in the lower deformation as compared to the film without any clay. From their observations, it was found that the addition of MMT clay to the plasticized polymer electrolyte not only increased the ionic conductivity but also improved the solidification of the electrolyte. These improvements led to the mechanical stability of the polymer composite films and the stability of DSSCs as well. DSSCs fabricated with the nanocomposites polymer electrolyte showed reasonable conversion efficiencies of ~1.6% and ~3.2% at 100 mW/cm^2 and 10 mW/cm^2, respectively. The device presented very poor FF values of ~0.40 at 100 mW/cm^2, which was attributed to the low penetration of the composite electrolyte into the pores of the TiO_2 film. The MMT clay as nanofillers was also used by Lin et al. They prepared the nano-composites of poly (nisopropylacrylamide) with MMT clay to a liquid electrolyte system as a

gelator and applied as solid polymer electrolyte. The poly (nisopropylacrylamide)-MMT electrolyte-based DSSC achieved a relatively high conversion efficiency of ~5.4% with a J_{SC} of ~12.6 mA/cm^2, V_{OC} of ~0.73 V, and FF of ~0.59, whereas the DSSC prepared with the electrolyte gelled with the pure polymer presented lower photovoltaic parameters of J_{SC} (~7.28 mA/cm^2), V_{OC} (~0.72 V), FF (0.60), and conversion efficiency (~3.2%) at 100 mW/cm^2. From the electrochemical impedance spectroscopy, a considerable decrease in impedance values was observed by DSSC fabricated with nanocomposite-gelled electrolyte. The impedance at the electrolyte/dye-coated TiO_2 interface, and the Nernstian diffusion within the electrolytes were decreased, resulted in the high photocurrent density leading to the high performance of DSSCs. They also investigated the molar conductivity of the nanocomposite-gelled electrolytes to explain the high ionic conductivity and improved electrochemical behavior of electrolyte.

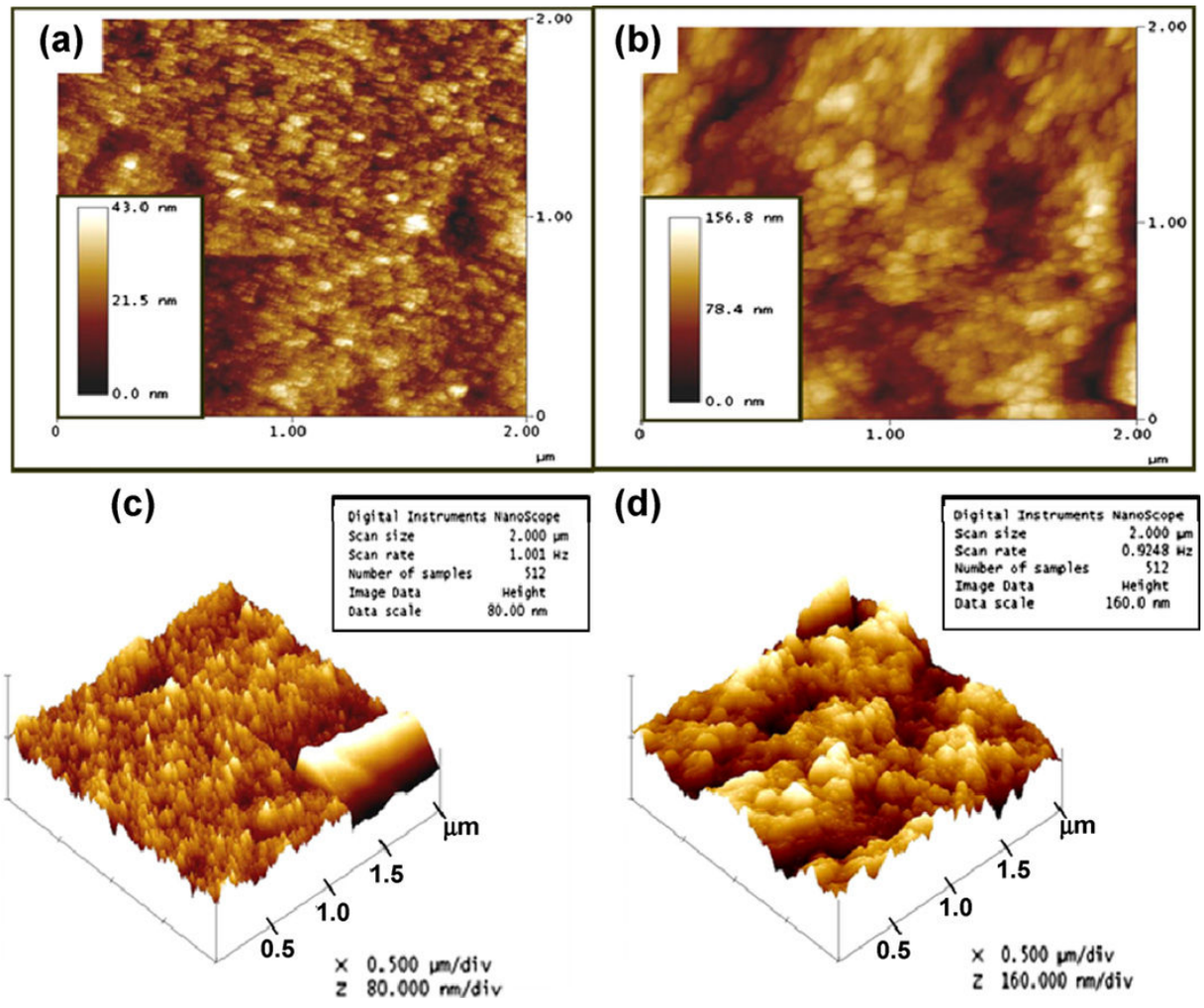

Figure 32. Topographic and three-dimensional AFM images of (a), (c) PEGME-TiO_2 and (b), (d) PEGMETiO_2/80C. Reprinted with permission from [Akhtar, 2011], Mater. Chem. Phys. 127 (2011) 479.© 2011, Elsevier Ltd.

http://dx.doi.org/10.5772/51432

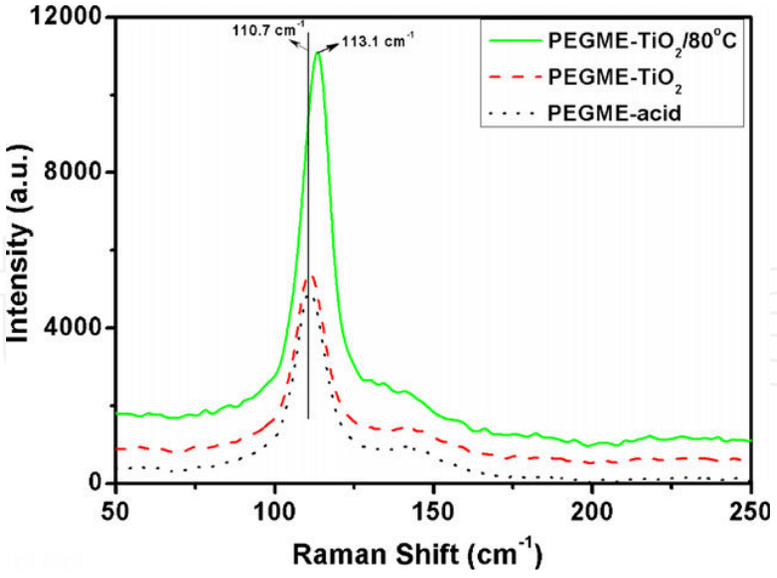

Figure 33. Raman spectra of PEGME-acid, PEGME–TiO_2 and PEGME–TiO_2/80 ∘C composite electrolytes. Reprinted with permission from [Akhtar., 2011], Mater. Chem. Phys. 127 (2011) 479. © 2011, Elsevier Ltd.

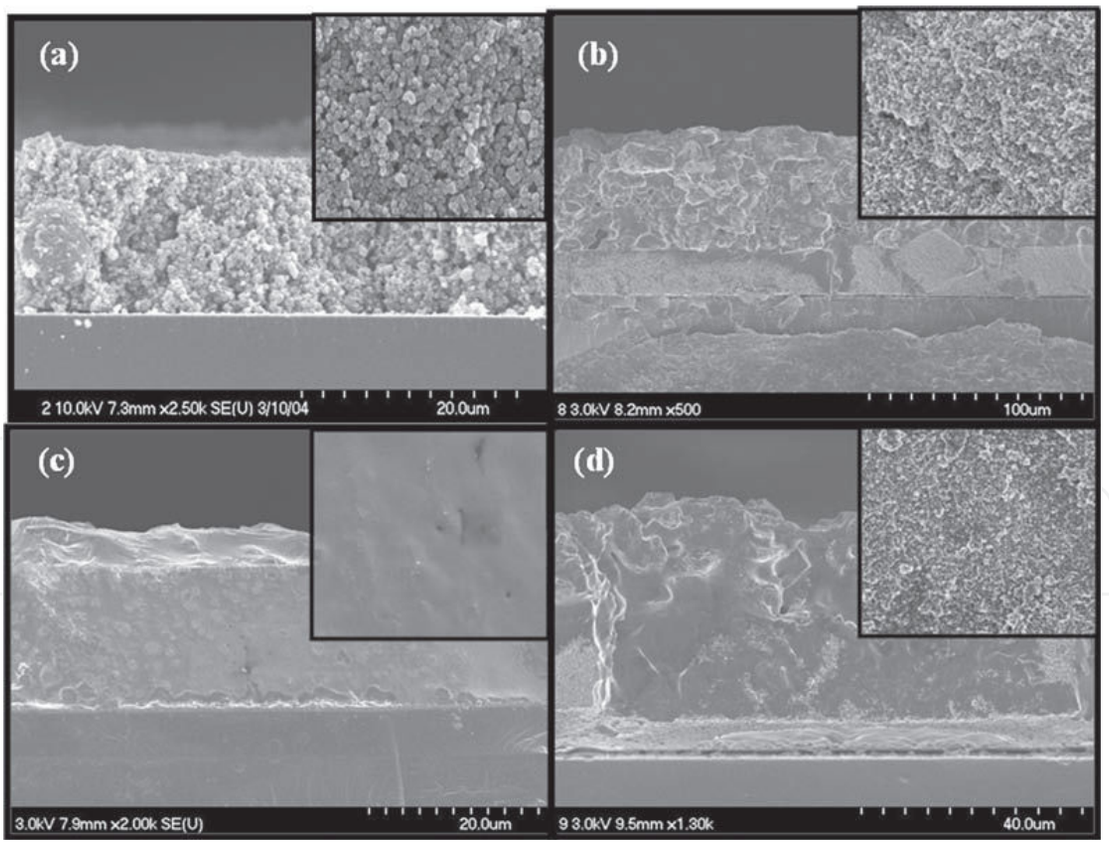

Figure 34. Cross-section and top view (inset) FE-SEM images of the TiO2 thin film (a) before electrolyte filling and after introducing composite electrolytes of (b) PEG-TiNT5, (c) PEG-TiNT10, and (d) PEG-TiNT20. Reprinted with permission from [Akhtar., 2007], Electrochem. Commun. 9 (2007) 2833.© 2007, Elsevier Ltd.

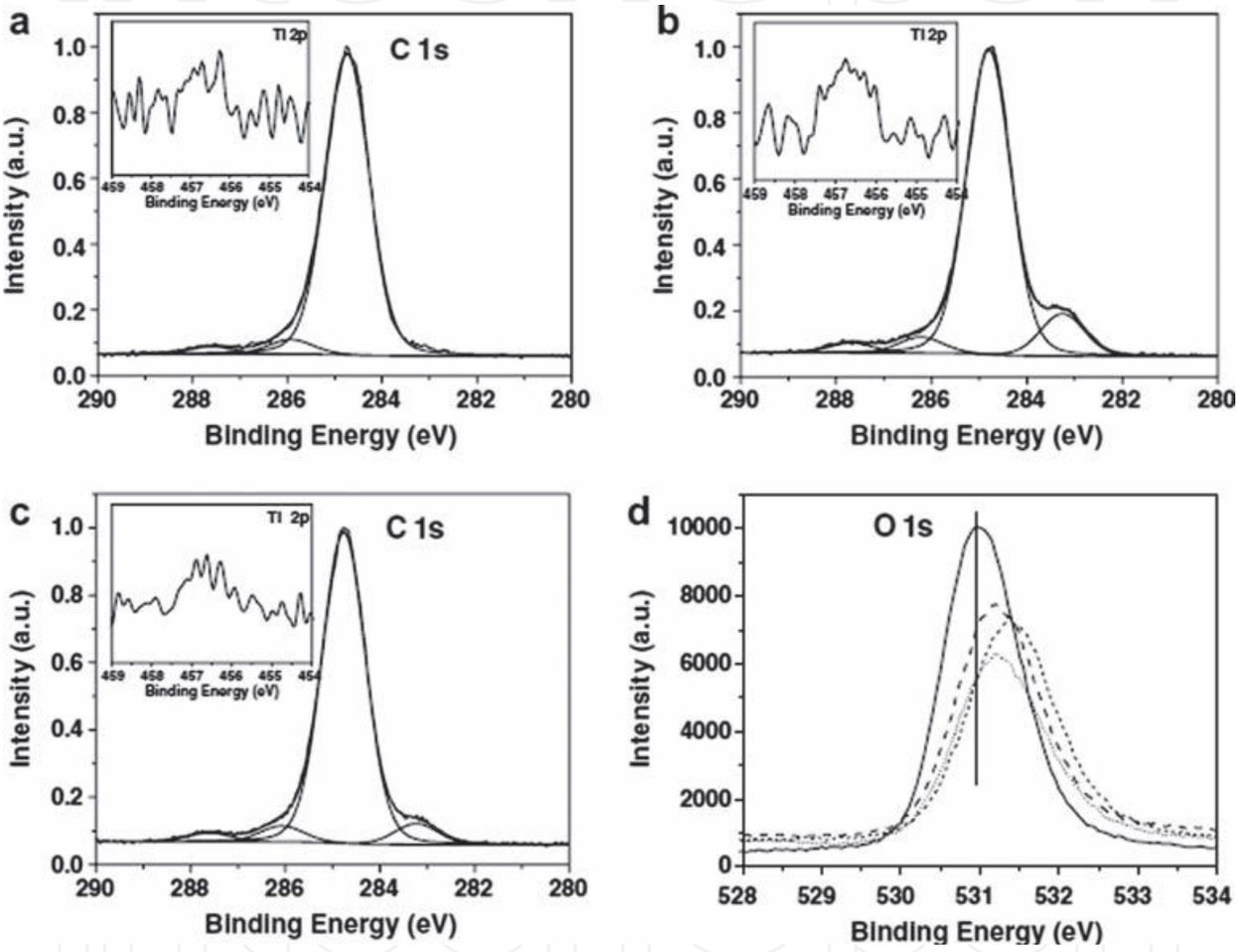

Figure 35. XPS spectra of the composite electrolytes. (a) PEG-TiNT5, (b) PEG-TiNT10, (c) PEG-TiNT20, and (d) O 1 s of PEG (—), PEG-TiNT5 (- - - -) PEG-TiNT10 (…..) and PEG-TiNT20 (-.-.-). Reprinted with permission from [Akhtar., 2007], Electrochem. Commun. 9 (2007) 2833.© 2007, Elsevier Ltd.

http://dx.doi.org/10.5772/51432

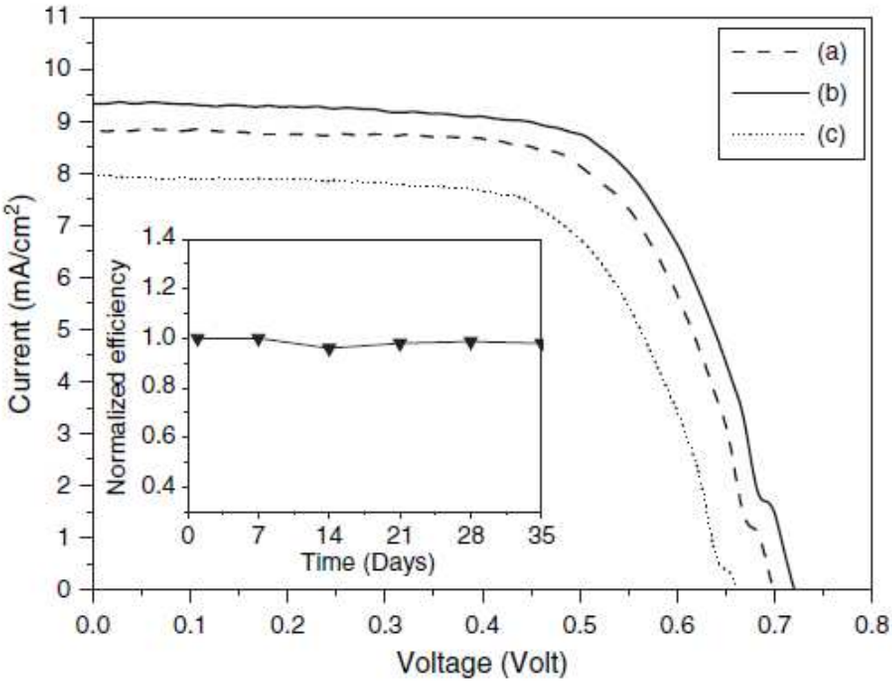

Figure 36. Current–voltage characteristics of DSSC fabricated with composite electrolytes of (a) PEG-TiNT5, (b) PEG-TiNT10, and (c) PEG-TiNT20. Inset shows the stability test of DSSC fabricated with composite electrolyte of PEG-TiNT10. Reprinted with permission from [Akhtar, 2007], Electrochem. Commun. 9 (2007) 2833.© 2007, Elsevier Ltd.

9. Conclusions

In summary, the morphological, structural, crystalline, optical, electrical and photovoltaic properties of conducting polymers, nanocomposites of conducting polymer/inorganic nanomaterials and semiconducting metal oxides have been discussed. The PANI nanocomposites with semiconducting materials have shown the improved penetration and optoelectronic properties, and applied for the electrical and electronic application such as diodes and solar cells. Here, the uniform distribution of CdS nanomaterials effectively improves the electronic state of PANI like polarons and bipolarons for the high charge carriers and enhances the charge transfer. The unique conducting polymers, particularly PANI nanomaterials have been used as hole transporting material and as counter electrodes for the applications of DSSCs. The metal oxide semiconducting nanomaterials, particularly TiO_2 and ZnO nanomaterials, in terms of morphology, surface properties, dye absorption and application in DSSCs are extensively summarized. Various morphologies of metal oxides nanostructures greatly affect the performances of dye absorption, electrical, electrochemical, and photovoltaic devices. The metal oxides semiconducting nanomaterials with different morphologies and sizes enhance the surface-to-volume ratio and produce the highly advanced photoanodes for the efficient DSSCs. The morphologies of metal oxides semiconducting considerably influence the dye absorption, light harvesting and results in increased electron transfer and reduce the recom-

bination rate during the operation of DSSCs. The photovoltaic properties such as J_{SC}, V_{OC}, FF, and conversion efficiency have significantly improved by altering the sizes and shapes of the metal oxides semiconductors. The chapter also summarizes the use of various metal oxide semiconducting nanomaterials as nanofillers in polymer electrolytes and describes their effect on the properties of polymer electrolytes and the performances of DSSCs. The introduction of metal oxide semiconducting nanomaterials into the polymer matrix has significantly improved the amorphicity, mechanical, thermal and ionic conductivity of polymer electrolytes. The chapter includes some of the polymer composite electrolytes and their photovoltaic properties for DSSCs.

Author details

Sadia Ameen[1], M. Shaheer Akhtar[2], Minwu Song[1] and Hyung Shik Shin[1]

1 Energy Materials & Surface Science Laboratory, Solar Energy Research Center, School of Chemical Engineering, Chonbuk National University, Jeonju, Republic of Korea

2 New and Renewable Energy Material Development Center (NewREC), Chonbuk National University, Jeonbuk, Republic of Korea

References

[1] Shirakawa H. The discovery of polyacetylene film: the dawning of an era of conducting polymers. Angewandte Chemie International Edition 2001;40:2575–2580.

[2] MacDiarmid AG. Synthetic metals: a novel role for organic polymers. Angewandte Chemie International Edition 2001; 40:2581–2590.

[3] Gerard M, Chaubey A, Malhotra BD. Biosens. Application of conducting polymers to biosensors. Biosensors and Bioelectronics 2002;17:345-359.

[4] Friend RH, Gymer RW, Holmes AB, Burroughes JH, Marks RN, Taliani C, Bradley DD C, Santos DA, Brédas JL, Lögdlund M, Salaneck WR. Electroluminescence in conjugated polymers. Nature 1999; 397:121-128.

[5] Sirringhaus H, Tessler N, Friend RH. Integrated Optoelectronic Devices based on. Conjugated Polymers. Science 1998; 280:1741-1744.

[6] Morrin A, Wilbeer F, Ngamna O, Moulton SE, Killard AJ, Wallace GG, Novel biosensor fabrication methodology based on processable conducting polyaniline nanoparticles. Electrochemistry Communication 2005; 7:317-322.

[7] Jang J, Bae J, Lee K. Synthesis and characterization of polyaniline nanorods as curing agent and nanofiller for epoxy matrix composite, Polymer 2005;46:3677-3684.

[8] Plesu N, Ilia G, Pascariu A, Vlase G. Preparation, degradation of polyaniline doped with organic phosphorus acids and corrosion essays of poly aniline-acrylic blends. Synthetic Metals 2006; 156:230-238.

[9] Han DH, Lee HJ, Park SM. Electrochemistry of conductive polymers XXXV: Electrical and morphological characteristics of polypyrrole films prepared in aqueous media studied by current sensing atomic force microscopy. Electrochimica Acta 2005;50:3085-3092.

[10] Johanson U, Marandi A, Tamm T, Tamm J. Comparative study of the behavior of anions in polypyrrole films. Electrochimica Acta 2005;50:1523-1528.

[11] Krivan E, Peintler G, Visy C. Matrix rank analysis of spectral studies on the electropolymerisation and discharge process of conducting polypyrrole/dodecyl sulfate films. Electrochimica Acta 2005;50:1529-1535.

[12] Chehimi MM, Abel ML, Perruchot C, Delamar M, Lascelles SF, Armes SP. The determination of the surface energy of conducting polymers by inverse gas chromatography at infinite dilution. Synthetic Metals 1999;104:51-59.

[13] Khomenko VG, Barsukov VZ, Katashinskii AS. The catalytic activity of conducting polymers toward oxygen reduction. Electrochimica Acta 2005;50:1675-1683.

[14] Hien NTL, Garcia B, Pailleret A, Deslouis C. Role of doping ions in the corrosion protection of iron by polypyrrole films. Electrochimica Acta 2005;50:1747-1755.

[15] Liu L, Zhao Y, Zhou Q, Xu H, Zhao C, Jiang Z. Nano-polypyrrole supercapacitor arrays prepared by layer-by-layer assembling method in anodic aluminum oxide templates. Journal of Solid State Electrochemistry 2007;11:32-37.

[16] Krivoshei IV, Skorobogatov VM. "Polyacetylene and Polyarylenes; Polymer Monographs." Vol. 10,Gordon and Breach Science Publishers, Philadelphia, PA, 1991

[17] Kovacic P, Jones MB. Dehydro coupling of aromatic nuclei by catalyst-oxidant systems: poly(p-phenylene). Chemical Reviews 1987;87:357-379.

[18] Shi G, Xue G, Li C, Jin S, Yu B. Uniaxial oriented poly(p-phenylene) fibrils and films. Macromolecules 1994;27:3678-3679.

[19] Roth S, Bleier H. Solitons in polyacetylene. Advances in Physics1987;36:385-462.

[20] Jacky JWY, Tang BZ. Functional polyacetylenes. Account of Chemical Research 2005;38:745-754.

[21] Asato AE, Liu RSH, Rao VP, Cai YM. Azulene-Containing Donor-Acceptor Compounds as Second-Order Nonlinear Chromophores. Tetrahedron Letters 1996;37:419-422.

[22] Taudi H, Bernede JC, Valle D, Bonnet MAA, Morsli M. Influence of the electrochemical conditions on the properties of polymerized carbazole. Journal of Materials Science 2001;36:631-634.

[23] Baba A, Onishi K, Knoll W, Advincula RC. Investigating Work Function Tunable Hole-Injection/Transport Layers of Electrodeposited Polycarbazole Network Thin Films. Journal of Physical Chemistry B 2004;108:18949-18955.

[24] Pud AA. Stability and degradation of conducting polymers in electrochemical systems. Synthetic Metals 1994;66(1):1–18.

[25] Min G. Conducting polymers and their applications in the film industry: polyaniline polyimide blended films. Synthetic Metals 1999;102(1–3):1163–1166.

[26] Davies JE, Less RJ, May I, Rawson JM. Isolation of the first diselenadiazolyl complex, $Pd_3[PhCNSeSeN]_2[PPh_3]_4$ 2PhMe New J. Chem. 1998;22:763-765

[27] Hahiwara T, Demura T, Iwata K. Synthesis and properties of electrically conducting polymers from aromatic amines. Synthetic Metals 1987;18:317-322.

[28] Snauwaert P, Lazzaroni R, Riga J, Verbist JJ. Electronic structure of polyaniline and substituted derivatives. Synthetic Metals 1987; 18:335-340.

[29] Cho MS, Cho YH, Choi HJ, Jhon MS. Synthesis and electrorheological characteristics of polyaniline-coated poly(methyl methacrylate) microsphere: Size effect. Langmuir 2003;19:5875-5881.

[30] Jindal Z, Verma NK. Electrochemical template–assisted fabrication of CdS micro/nanostructures. Physica E 2009;41:1752–1756.

[31] Soudi R, Kamal M, Shabaka AA, Abdelrazek EM, Eisa W. Synthesis, characterization and spectroscopic studies of CdS/polyaniline core/shell nanocomposites. Synthetic Metals 2010;160:479–484.

[32] Xi Y, Zhou J, Guo H, Cai C, Lin Z. Enhanced photoluminescence in core-sheath CdS–PANI coaxial nanocables: a charge transfer mechanism. Chemical Physics Letters 2005;412:60-63.

[33] Seoudi R, Shabaka AA., Kamal M, Abdelrazek EM, Eisa H. Dependence of structural, vibrational spectroscopy and optical properties on the particle sizes of CdS/polyaniline core/shell nanocomposites. Journal of Molecular Structure 2012;10(13):156-162.

[34] Raut BT, Chougule MA, Sen S, Pawar RC, Lee CS, Patil VB. Novel method of fabrication of polyaniline–CdS nanocomposites: Structural, morphological and optoelectronic properties. Ceramics International 2012;38:3999-4007.

[35] Ameen S, Akhtar MS, Kim YS, Shin HS. Synthesis and electrochemical impedance properties of CdS nanoparticles decorated polyaniline nanorods. Chemical Engineering Journal 2012;181–182:806–812.

[36] Boyer MI, Quillard S, Louarn G, Froyer G, Lefrant S. Vibrational study of the $FeCl_3$-doped dimer of polyaniline; a good model compound of emeraldine salt. Journal of Physical Chemistry B 2000;104:8952–896.

[37] Mazeikiene R, Statino A, Kuodis Z, Niaura G, Malinauskas A. In situ Raman spectroelectrochemical study of self-doped polyaniline degradation kinetics. Electrochemistry Communications 2006;8:1082–1086.

[38] Khiew PS. Huang NM, Radiman S, Ahmad MS. Synthesis and characterization of conducting polyaniline-coated cadmium sulphide nanocomposites in reverse microemulsion. Materials Letters 2004;58:516–521.

[39] Shimano JY, MacDiarmid AG. Polyaniline, a dynamic block copolymer: key to attaining its intrinsic conductivity. Synthetic Metals 2001;123:251–262.

[40] Monkman AP, Stevens GC, Bloor D. X-ray photoelectron spectroscopic investigations of the chain structure and doping mechanisms in polyaniline. Journal of Physics D: Applied Physics 1991;24:738–743.

[41] Wu MS, Wen TC, Gopalan A. Electrochemical copolymerization of diphenylamine and anthranilic acid with various feed ratios. Journal of the Electrochemical Society 2001;148:D65–D73.

[42] Ameen S, Akhtar MS., Kim YS, Yang OB, Shin HS. Electrical and structural characterization of plasma polymerized polyaniline/TiO_2 heterostructure diode: a comparative study of single and bilayer TiO_2 thin film electrode. Journal of Nanoscience and Nanotechnology 2011;11:3306–3313.

[43] Glidle A, Swann MJ, Hadyoon CS, Cui L, Davis J, Ryder KS, Cooper JM. XPS assaying of electrodeposited copolymer composition to optimise sensor materials. Journal of Electron Spectroscopy and Related Phenomena 121 (2001) 131–148.

[44] Suzer S, Birer O, Sevil UA, Guven O. XPS investigations on conducting polymers. Turkish Journal of Chemistry 1998;22:59–65.

[45] Duran JDG, Guindo MC, Delgado AV, Caballero FG. Surface chemical analysis and electrokinetic properties of synthetic spherical mixed zinc–cadmium sulfides, Journal of Colloids and Interface Science 1997;193:223–233.

[46] Fiordiponti P, Pistoia G. An impedance study of polyaniline films in aqueous and organic solutions. Electrochimica Acta 1989;34:215–221. (b) Vorotyntsev MA, Badiali JP, Inzelt G. Electrochemical impedance spectroscopy of thin films with two mobile charge carriers: effects of the interfacial charging. Journal of Electroanalytical Chemistry 1999;472:7–19.

[47] Hagfeldt A, Gratzel M. Light-Induced Redox Reactions in Nanocrystalline Systems. Chemical Reviews 1995;95:49-68.

[48] Cheng YJ, Yang SH, Hsu CS. Synthesis of conjugated polymers for organic solar cell applications, Chemical Reviews 2009;109:5868–5923.

[49] Jaglarz J, Wagner T, Cisowski J, Sanetra J. Ellipsometric studies of carbazole-containing polymer layers. Optical Materials, 2007;29:908-912.

[50] Kudo N, Shimazaki Y, Ohkita H, Ohoka M, Ito S. Organicinorganic hybrid solar cells based on conducting polymer and SnO_2 nanoparticles chemically modified with a fullerene derivative. Solar Energy Materials Solar Cells 2007;91:1243-1247.

[51] Woo S, Jeong JH, Lyu HK, Jeong S, Sim JH, Kim WH, Han YS, Kim Y. Hybrid solar cells with conducting polymers and vertically aligned silicon nanowire arrays: The effect of silicon conductivity. Physica B: Condensed Matter 2012;407:3059-3062.

[52] Tan F, Qu S, Wu J, Wang Z, Jin L, Bi Y, Cao J, Liu K, Zhang J. Wang Z., Electrodepostied polyaniline films decorated with nano-islands: Characterization and application as anode buffer layers in solar cells. Solar Energy Materials Solar Cells 2011;95:440-445.

[53] Chang MY, Wu CS, Chen YF, Hsieh BZ, Huang WY, Ho KS, Hsieh TH, Han YK. Polymer solar cells incorporating one-dimensional polyaniline nanotubes. Organic Electronics 2008; 9:1136-1139.

[54] Lim TH, Oh KW, Kim SH. Self-assembly supramolecules to enhance electrical conductivity of polyaniline for a flexible organic solar cells anode. Solar Energy Materials Solar Cells 2012;101:232-240.

[55] Bejbouji H, Vignau LL, Miane J, Dang MT, Oualim EM, Harmouchi M, Mouhsen A. Polyaniline as a hole injection layer on organic photovoltaic cells. Solar Energy Materials Solar Cells. 2010;94:176-181.

[56] Zhu S., Wei W., Chen X., Jiang M., Zhou Z. Hybrid structure of polyaniline/ZnO nanograss and its application in dye-sensitized solar cell with performance improvement. Journal of Solid State Chemistry 2012;190:174-179.

[57] Ameen S, Akhtar MS, Song M, Kim YS, Shin HS. Plasma Deposited Polyaniline on Ruthenium Dye Sensitized Zno Thin Film for Dye Sensitized Solar Cell. Advanced Science Letters 2012: doi:10.1166/asl.2012.3305.

[58] Malherbe R, Martinez J, Reguera E, Navarro E. Journal of Materials Science 1992;28:274.

[59] Ameen S, Akhtar MS, Kim G-S, Kim YS, Yang O-B, Shin HS. Plasma-enhanced polymerized aniline/TiO_2 dye-sensitized solar cells. Journal of Alloys and Compounds 2009;487:382–386.

[60] Bisquert J. Theory of the Impedance of Electron Diffusion and Recombination in a Thin Layer. Journal of Physical Chemistry B 2002;106:325-333.

[61] J.R. Macdonald, Impedance Spectroscopy, John Wiley & Sons, New York, 1987.

[62] Brad AJ, Faulkner LR. Electrochemical Methods: Fundamentals and Applications, John Wiley & Sons, New York, 1980, p. 350.

[63] Yeh MH, Lee CP, Chou CY, Lin LY, Wei HY, Chu CW, Vittal R, Ho KC. Conducting polymer-based counter electrode for a quantum-dot-sensitized solar cell (QDSSC) with a polysulfide electrolyte. Electrochimica Acta, 2011;57:277-284.

[64]] Lee KM, Chen PY, Hsu CY, Huang JH, Ho WH, Chen HC, Ho KC. A high-performance counter electrode based on poly(3,4-alkylenedioxythiophene) for dye-sensitized solar cells. Journal of Power Sources. 2009;188:313-318.

[65] Lee KM, Chiu WH, Wei HY, Hu CW, Suryanarayanan V, Hsieh WF, Ho KC. Effects of mesoscopic poly(3,4-ethylenedioxythiophene) films as counter electrodes for dye-sensitized solar cells. Thin Solid Films, 2010;518:1716-1721

[66] Maiaugree W, Pimanpang S, Towannang M, Saekow S, Jarernboon W, Amornkitbamrung V. Optimization of TiO_2 nanoparticle mixed PEDOT–PSS counter electrodes for high efficiency dye sensitized solar cell. Journal of Non-Crystalline Solids 2012; In Press: doi:10.1016/j.jnoncrysol.2011.12.104.

[67] Chen J, Li B, Zheng J, Zhao J, Jing H, Zhu Z. Polyaniline nanofiber/carbon film as flexible counter electrodes in platinum-free dye-sensitized solar cells. Electrochimica Acta 2011; 56:4624-4630.

[68] Li Q, Wu J, Tang Q, Lan Z, Li P, Lin J, Fan L. Application of microporous polyaniline counter electrode for dye-sensitized solar cells. Electrochemistry Communications 2008; 10:1299-1302.

[69] Zhang J, Hreid T, Li X, Guo W, Wang L, Shi X, Su H, Yuan Z. Nanostructured polyaniline counter electrode for dye-sensitised solar cells: Fabrication and investigation of its electrochemical formation mechanism. Electrochimica Acta, 2010;55:3664-3668.

[70] Wang G, Xing W, Zhuo S. The production of polyaniline/graphene hybrids for use as a counter electrode in dye-sensitized solar cells. Electrochimica Acta 2012;66:151-157.

[71] Tai Q, Chen B, Guo F, Xu S, Hu H, Sebo B, Zhao XZ. In situ prepared transparent polyaniline electrode and its application in bifacial dye-sensitized solar cells. ACS Nano 2011; 24;5(5):3795-9.

[72] Ameen S, Akhtar MS, Kim YS, Yang OB, Shin HS. Sulfamic Acid-Doped Polyaniline Nanofibers Thin Film-Based Counter Electrode: Application in Dye-Sensitized Solar Cells. Journal of Physical Chemistry C 2010;114:4760–4764.

[73] Nazeeruddin, MK, Kay A, Rodicio I, Humphry-Baker R, Muller E, Liska P, lachopoulosn N, Gratzel M. Conversion of light to electricity by cis-X2bis(2,2'-bipyridyl-4,4'-dicarboxylate)ruthenium(II) charge-transfer sensitizers (X = Cl^-, Br^-, I^-, CN^-, and SCN^-) on nanocrystalline titanium dioxide electrodes. Journal of the American Chemical Society 1993;115:6382–6390.

[74] Li Z, Ye B, Hu X, Ma X, Zhang X, Deng Y. Facile Electropolymerized-PANI as counter electrode for low cost dye-sensitized solar cells. Electrochemistry Communications 2009;11:1768-1771.

[75] Graetzel M. Photoelectrochemical cells. Nature 2011;414:338-344.

[76] Kawai T, Takahashi H, Matsushima Y, Ogata T, Unuma H. Evaluation of Photocatalytic Activity of TiO_2 Thin Films by Spin-Trap ESR Spectroscopy. Science of Advanced Materials, 2010; 2:74-78.

[77] Thomas J, Kumar KP, Mathew S. Enhancement of Sunlight Photocatalysis of Nano TiO_2 by Ag Nanoparticles Stabilized with D-Glucosamine. Science of Advanced Materials 2011;3:59-65.

[78] Lee SM, Cho SN, Cheon S. Anisotropic Shape Control of Colloidal Inorganic Nanocrystals. Advanced Materials 2003;15:441-444.

[79] Hyam RS, Bhosale RK, Lee W, Han SH, Hannoyer B, Ogale SB. Room Temperature Synthesis of Rutile TiO_2 Hierarchical Nanoneedle Flower Morphology for Dye Sensitized Solar Cell. Journal of Nanoscience and Nanotechnology 2010;10:5894-5898.

[80] Du G, Wan B, Guo Z, Shen J, Li Y, Liu H. Effect of Annealing on Electrochemical Performance of Anodized TiO2 Nanotubes for Lithium Ion Batteries. Advanced Science Letters, 2011;4:469-473.

[81] Mor GK, Shankar K, Paulose M, Varghese PK, Grimes CA. Use of Highly-Ordered TiO_2 Nanotube Arrays in Dye-Sensitized Solar Cells. Nano Letters, 2006;6:215-218.

[82] Ameen S, Akhtar MS, Kim YS, Shin HS. Controlled synthesis and photoelectrochemical properties of highly ordered TiO_2 nanorods. RSC Advances, 2012;2:4807–4813

[83] Shin K, Seok SI, Im SH, Park JH. CdS or CdSe decorated TiO_2 nanotube arrays from spray pyrolysis deposition: use in photoelectrochemical cells. Chemical Communication, 2010;46:2385-2387.

[84] Du PA, Chen HH, Lu YC. Dye sensitized solar cells using well-aligned zinc oxide nanotip arrays. Applied Physics Letters 2006;89:253513-253615.

[85] Gregg BA. Interfacial processes in the dye-sensitized solar cell. Coordination Chemistry Reviews 2004;248:1215-1224.

[86] Lee S, Cho IS, Lee JH, Kim HD, Kim DW, Kim JY, Shin H, Lee JK, Jung HS, Park NG, Kim K, Ko MJ, Hong KS. Two-Step Sol−Gel Method-Based TiO_2 Nanoparticles with Uniform Morphology and Size for Efficient Photo-Energy Conversion Devices. Chemistry of Materials, 2010;22:1958-1965.

[87] Chakravarty R, Periasamym C. Effect of aluminium doping on structural and optoelectronic properties of sol-gel derived nanocrystalline ZnO thin film. Science of Advanced Materials 2011;3:276–283.

[88] Chao CH, Chan CH, Huang JJ, Chang LS, Shih HC. Manipulated the band gap of 1D ZnO nano-rods array with controlled solution concentration and its application for DSSCs. Current Applied Physics 2011;11:S136–S139

[89] Mohanta SK, Kim DC, Kong BH, Cho HK, Liu W, Tripathy S. Optical Properties of ZnO Nanorods and Hybrid Structures Grown on p-type GaN/Sapphire and Silicon-on-

Insulator Substrates. Science of Advanced Materials 2010;2:64-68. (b) Zhang H, Du N, Chen B, Li D, Yang D. Carbon Nanotube-ZnO Nanosphere Heterostructures: Low-Temperature Chemical Reaction Synthesis, Photoluminescence, and Their Application for Room Temperature NH_3 Gas Sensor. Science of Advanced Materials 2009;1:13-17.

[90] Akhtar MS, Khan MA, Jeon MS, Yang OB. Controlled synthesis of various ZnO nanostructured materials by capping agents-assisted hydrothermal method for dye-sensitized solar cells. Electrochimica Acta 2008;53:7869–7874.

[91] Tseng YK, Hsu HC, Hsieh WF, Liu KS, Chen IC. Two-step oxygen injection process for growing ZnO nanorods. Journal of Materials Research 2003;18:2837–2844.

[92] Yu WD, Li XM, Gao XD, Self-catalytic synthesis and photoluminescence of ZnO nanostructures on ZnO nanocrystal substrates, Applied Physics Letters 2004;84:2651–2658.

[93] Uthirakumar P, Kang JH, Senthilarasu S, Hong CH. The different types of ZnO materials on the performance of dye-sensitized solar cells, Physica E 2011;43:1746–1751.

[94] Greene LE, Yuhas BD, Law M, Zitoun D, Yang PD. Solution-Grown Zinc Oxide Nanowires. Inorganic Chemistry 2006;45:7535-7543.

[95] Han H, Bach U, Cheng YB, Caruso RA. Increased nanopore filling: Effect on monolithic all-solid-state dye-sensitized solar cells. Applied Physics Letters 2007;90:213510-213512.

[96] Gao YF, Nagai M, Chang TC, Shyue JJ. Solution-Derived ZnO Nanowire Array Film as Photoelectrode in Dye-Sensitized Solar Cells. Crystal Growth and Design 2007;7:2467-2471.

[97] Jiang CY, Sun XW, Tan KW, Lo GQ, Kyaw AKK, Kwong DL. High-bendability flexible dye-sensitized solar cell with a nanoparticle-modified ZnO-nanowire electrode. Applied Physics Letters 2008;92:143101-143103.

[98] Akhtar MS, Khan MA, Jeon MS, Yang OB. Controlled synthesis of various ZnO nanostructured materials by capping agents-assisted hydrothermal method for dye-sensitized solar cells. Electrochimica Acta 2008;53:7869-7874.

[99] Umar A, Al-Hajry A, Hahn YB, Kim DH. Rapid synthesis and dye-sensitized solar cell applications of hexagonal-shaped ZnO nanorods. Electrochimica Acta 2009;54:5358-5362.

[100] Ameen S, Akhtar MS, Shin HS. Growth and characterization of nanospikes decorated ZnO sheets and their solar cell application. Chemical Engineering Journal 2012;195-196:307–313.

[101] Umar A, Kim SH, Kim JH, Al-Hajry A, Hahn YB. Temperature-dependant non-catalytic growth of ultraviolet-emitting ZnO nanostructures on silicon substrate by thermal evaporation process. Journal of Alloys and Compounds 2008;463:516–521.

[102] Laudise RA, Kolb ED, Caporason AJ. Hydrothermal growth of large sound crystals of zinc oxide. Journal of the American Ceramic Society 1964;47:9–12.

[103] Ameen S, Akhtar MS., Kim YS, Yang OB, Shin HS. Influence of seed layer treatment on low temperature grown ZnO nanotubes: performances in dye sensitized solar cells, Electrochimica Acta 2011;56:1111–1116.

[104] Wagner CD, Riggs WM, Davis LE, Moulder JF, Muilenberg GE. Handbook of X-ray Photoelectron Spectroscopy, Perkin Elmer, Eden Prairie, 1979.

[105] Leunga CY, Djurisic AB, Leung YH, Ding L, Yang CL, Ge WK. Influence of the carrier gas on the luminescence of ZnO tetrapod nanowires, Journal of Crystal Growth 2006;290:131–136.

[106] Fan JCC, Goodenough JB. X-ray photoemission spectroscopy studies of Sn doped indium-oxide films, Journal of Applied Physics 1977;48:3524–3531.

[107] Martinson ABF, Elam JW, Hupp JT, Pellin MJ. ZnO nanotube based dyesensitized solar cells Nano. Letters 2007;7:2183–2187.

[108] Umar A, Singh P, Al-Ghamdi AA, Al-Heniti S. Direct growth of ZnO nanosheets on FTO substrate for dye-sensitized solar cells applications, Journal of Nanoscience and Nanotechnology 2010;10:6666–6671.

[109] Al-Hajry A, Umar A, Hahn YB, Kim DH. Growth, properties and dyesensitized solar cells–applications of ZnO nanorods grown by lowtemperature solution process. Superlattice Microstructures 2009;45:529–534.

[110] Ilican S, Caglar Y, Caglar M, Yakuphanoglu F. Structural, optical and electrical properties of F-doped ZnO nanorod semiconductor thin films deposited by solgel process. Applied Surface Science 2008;255:2353–2359.

[111] Peiteado M, Iglesias Y, Fernandez JF, De Frutos J, Caballero AC. Microstructural development of tin-doped ZnO bulk ceramics. Materials Chemistry and Physics 2007;101:1–6.

[112] Tsay CY, Cheng HC, Tung YT, Tuan WH, Lin CK. Effect of Sn-doped on microstructural and optical properties of ZnO thin films deposited by sol-gel method. Thin Solid Films 2008;517:1032–1036.

[113] Yung KC, Liem H, Choy HS, 185002 enhanced redshift of the optical band gap in Sn-doped ZnO free standing films using the sol–gel method. Journal of Physics D: Applied Physics 2009;42:15002-15006.

[114] Ameen S, Akhtar MS, Seo HK, Kim YS, Shin HS. Influence of Sn doping on ZnO nanostructures from nanoparticles to spindle shape and their photoelectrochemical properties for dye sensitized solar cells. Chemical Engineering Journal 2012;187: 351–356

[115] Exarhos GJ, Sharma SK. Influence of processing variables on the structure and properties of ZnO films. Thin Solid Films 1995;270:27–32.

[116] Yang J, Lee J, Im K, Lim S, Influence of Sn-doping in hydrothermal methods on the optical property of the ZnO nanorods. Physica E 2009;42:51–56.

[117] Sheini FJ, More MA, Jadkar SR, Patil KR, Pillai VK, Joag DS. Observation of photoconductivity in Sn-doped ZnO nanowires and their photoenhanced field emission behavior. Journal of Physical Chemistry C 2010;114:3843–3849.

[118] Dolbec R, ElKhakani MA, Serventi AM, Jacques RGS. Influence of the nanostructural characteristics on the gas sensing properties of pulsed laser deposited tin oxide thin films. Sensors and Actuators B 2003;93:566–571.

[119] Ye N, Qi J, Qi Z, Zhang X, Yang Y, Liu J, Zhang Y. Improvement of the performance of dye-sensitized solar cells using Sn-doped ZnO nanoparticles. Journal of Power Sources 2010;195:5806–5809.

[120] Kim MH, Suh M, Gowrishankar V, McGehee MD, Kwon YU. Confinement Effects of P3HT in Nanochannels and Their Implications for Bulk Heterojunction Solar Cells. Journal of Nanoscience and Nanotechnology 2010;10:279–284.

[121] Mridha S, Basak D. ZnO/polyaniline based inorganic/organic hybrid structure: Electrical and photoconductivity properties. Applied Physics Letters 2008;92:142111–142113

[122] Ameen S, Akhtar MS, Kim YS, Yang OB, Shin HS. Polyaniline/Ga doped ZnO Heterostructure Device via Plasma Enhanced Polymerization. Microchim Acta 2011;172:471–478.

[123] Umar A, Al-Hajry A, Hahn YB, Kim DH. Rapid synthesis and dye-sensitized solar cell applications of hexagonal-shaped ZnO nanorods. Electrochimica Acta 2009;54:5358–5362.

[124] Monkman AP, Stevens GC, Bloor D. X-ray photoelectron spectroscopic investigations of the chain structure and doping mechanisms in polyaniline. Journal of Physics D: Applied Physics 1991;24:738-741.

[125] Barr TL. Recent advances in x-ray photoelectron spectroscopy studies of oxides. Journal of Vacuum Science & Technology A 1991;93:179-185.

[126] Sans JA, Segura A, Royo JFS, Barber V, Fenollosa MAH, Marí B. Correlation between optical and transport properties of Ga doped ZnO thin films prepared by pulsed laser deposition. Superlattice Microstructures 2006;39:282–290.

[127] Chen Y, Kang ET, Neon KG, Lim SL, Ma ZH, Tan KL. Intrinsic redox states of polyaniline studied by high-resolution X ray photoelectron spectroscopy. Colloid and Polymer Science 2001;279:73–76.

[128] Kang ET, Neoh KG, Tan KL. Polyaniline: A polymer with many interesting intrinsic redox states. Progress in Polymer Science 1998;23:277–324.

[129] Mridha S, Basak D. ZnO/polyaniline based inorganic/organic hybrid structure: Electrical and photoconductivity properties. Appl. Phys. Lett. 2008;92:142111–142113.

[130] Ameen S, Akhtar MS, Ansari SG, Yang OB, Shin HS. Electrophoretically deposited polyaniline/ZnO nanoparticles for p–n heterostructure diodes. Superlattice and Microstructures 2009;46:872–880.

[131] Croce F, Appetechi GB, Persi L, Scrosati B. Nanocomposite polymer electrolytes for lithium batteries. Nature (London) 1998;394: 456-458.

[132] Kang MS, Ahnand KS, Lee JW. Quasi-solid-state dye-sensitized solar cells employing ternary component polymer-gel electrolytes. Journal of Power Sources 2008;180:896-901.

[133] Katsaros G, Stergiopoulos T, Arabatzis IM, Papadokostaki KG, Falaras P. A solvent-free composite polymer/inorganic oxide electrolyte for high efficiency solid-state dye-sensitized solar cells. Journal of Photochemistry and Photobiology A 2002;149:191-198.

[134] Stergiopoulos T, Arabatzis IM, Katsaros G, Falaras P. Binary Polyethylene Oxide/ Titania Solid-State Redox Electrolyte for Highly Efficient Nanocrystalline TiO_2 Photoelectrochemical Cells. Nano Letters 2002;2:1259-1261.

[135] Akhtar MS, Park JG, Kim UY, Yang OB. Composite electrolytes of polyethylene glycol methyl ether and TiO_2 for dye-sensitized solar cells—Effect of heat treatment. Materials Chemistry and Physics 2011;127:479-483.

[136] Tadayyoni MA, Gao P, Weaver MJ. Application of surface-enhanced Raman spectroscopy to mechanistic electrochemistry: Oxidation of iodide at gold electrodes. Journal of Electroanalytical Chemistry 1986;198:125-136.

[137] Kubo W, Murakoshi K, Kitamura T, Yoshida S, Haruki M, Hanabusa K, Shirai H, Wada Y, Yanagida S. Quasi-Solid-State Dye-Sensitized TiO_2 Solar Cells: Effective Charge Transport in Mesoporous Space Filled with Gel Electrolytes Containing Iodide and Iodine. Journal of Physical Chemistry B 2001;105:12809- 12815.

[138] Akhtar MS, Chun J M, Yang OB. Advanced composite gel electrolytes prepared with titania nanotube fillers in polyethylene glycol for the solid-state dye-sensitized solar cell. Electrochemistry Communications 2007;9:2833-2837.

[139] Zhang J, Han H, Wu S, Xu S, Yang Y, Zhou C, Zhao X. Conductive carbon nanoparticles hybrid PEO/P(VDF-HFP)/SiO_2 nanocomposite polymer electrolyte type dye sensitized solar cells. Solid State Ionics 2007;178:1595-1601.

[140] Han H, Bach U, Cheng YB. Caruso R A. Increased nanopore filling: Effect on monolithic all-solid-state dye-sensitized solar cells. Applied Physics Letters 2007;90:213510-213412.

[141] Zhang X, Yang H, Xiong HM, Li FY, Xia YY. A quasi-solid-state dye-sensitized solar cell based on the stable polymer-grafted nanoparticle composite electrolyte. Journal of Power Sources 2006;160:1451-1455.

[142] Nazmutdinova G, Sensfuss S, Schrödner M, Hinsch A, Sastrawan R, Gerhard., Himmler S, Wasserscheid P. Quasi-solid state polymer electrolytes for dye-sensitized solar cells:

Effect of the electrolyte components variation on the triiodide ion diffusion properties and charge-transfer resistance at platinum electrode. Solid State Ionics 2006;177:3141-3146.

[143] Tu CW, Liu KY, Chien AT, Yen MH, Weng TH, Ho KC, Lin KF. Enhancement of photocurrent of polymer-gelled dye-sensitized solar cell by incorporation of exfoliated montmorillonite nanoplatelets. Journal of Polymer Science A: Polymer Chemistry 2008;46:47- 53.

[144] Ito BI, de Freitas JN, De Paoli MA, Nogueira AF. Application of a Composite Polymer Electrolyte Based on Montmorillonite in Dye Sensitized Solar Cells. Journal of Brazilian Chemical Society 2008:19:688-696.

IntechOpen